

QUANTUM MECHANICS FOR CLOSURE OF DYNAMICAL SYSTEMS*

DAVID C. FREEMAN[†], DIMITRIOS GIANNAKIS[‡], AND JOANNA SLAWINSKA[§]

Abstract. We propose a scheme for data-driven parameterization of unresolved dimensions of dynamical systems based on the mathematical framework of quantum mechanics and Koopman operator theory. Given a system in which some components of the state are unknown, this method involves defining a surrogate system in a time-dependent quantum state which determines the fluxes from the unresolved degrees of freedom at each timestep. The quantum state is a density operator on a finite-dimensional Hilbert space of classical observables and evolves over time under an action induced by the Koopman operator. The quantum state also updates with new values of the resolved variables according to a quantum Bayes' law, implemented via an operator-valued feature map. Kernel methods are utilized to learn data-driven basis functions and represent quantum states, observables, and evolution operators as matrices. The resulting computational schemes are automatically positivity-preserving, aiding in the physical consistency of the parameterized system. We analyze the results of two different modalities of this methodology applied to the Lorenz 63 and Lorenz 96 multiscale systems, and show how this approach preserves important statistical and qualitative properties of the underlying chaotic systems.

Key words. dynamical closure, parameterization, quantum mechanics, Koopman operators, transfer operators, kernel methods

AMS subject classifications. 37M10, 37A50, 62M20, 68U20, 82C10

1. Introduction. Among the foundational problems in the modeling of complex dynamical systems is the question of how to account for fine-grain degrees of freedom which are too computationally complex to model directly. The Earth's climate system is a classical example of a multiscale, multiphysics system where direct numerical simulation of all relevant degrees of freedom is not computationally feasible (now, and for the foreseeable future [28]), necessitating the use of subgrid-scale models to represent unresolved degrees of freedom. For example, cloud formation (a highly influential process on climate scales) is in part determined by microscopic chemical processes and turbulent convective motions in the atmosphere across the entire globe. Representations of convective cloud physics within global climate models (GCMs) has thus relied on surrogate models of small-scale processes to approximate their aggregate contribution over the larger spatiotemporal climate scales [39]. This is a methodology known as *closure*, or *parameterization*, and besides climate dynamics it finds applications in many disciplines dealing with complex time-dependent phenomena, e.g., [65, 25].

In this paper, we present a new framework for closure of dynamical systems that models the unresolved degrees of freedom as a quantum mechanical system. Our approach extends a recently developed operator-theoretic framework for data

*Submitted to the editors DATE.

Funding: D.G. acknowledges support from the US National Science Foundation under grants 1842538 and DMS-1854383, the US Office of Naval Research under MURI grant N00014-19-1-242, and the US Department of Defense, Basic Research Office under Vannevar Bush Faculty Fellowship grant N00014-21-1-2946. D.C.F. is supported as a PhD student under the last grant.

[†]Department of Mathematics, Dartmouth College, Hanover, NH 03755, USA (david.c.freeman.gr@dartmouth.edu).

[‡]Department of Mathematics, Dartmouth College, Hanover, NH 03755, USA; Department of Physics and Astronomy, Dartmouth College, Hanover, NH 03755, USA (dimitrios.giannakis@dartmouth.edu).

[§]Department of Mathematics, Dartmouth College, Hanover, NH 03755; USA (joanna.m.slawska@dartmouth.edu).

assimilation, called quantum mechanical data assimilation (QMDA) [32, 29], to the setting of two-way coupling between classical and quantum systems representing the resolved and unresolved dynamics, respectively.

1.1. Parameterization. Early approaches to parameterization, e.g., [1, 30], were based on low-order bulk formulas representing an average flux from unresolved degrees of freedom to the resolved variables. These formulas are typically constructed using physical reasoning, and feature a small number of parameters that can be tuned, e.g., using observational data, so as to best match the behavior of nature, or a high-resolution reference model, on the resolved scales. More recently, with the advent of the “big data” era, data-driven parameterization schemes have received considerable attention [12, 11, 75]. These approaches employ training data generated by high-resolution, targeted simulations to learn models of the unresolved flux terms as functions of the resolved variables. The premise of these machine learning approaches is that by fitting closure models in a high-dimensional hypothesis space one can discover functional relationships between the resolved and unresolved variables that would be difficult to do on the basis of physical reasoning and/or asymptotic analysis alone. Indeed, this approach has been shown to outperform conventional parameterizations in terms of capturing the statistical behavior of the resolved variables in a variety of settings [12, 11, 75].

A common feature of parameterization schemes, including the methods outlined above, is dimension reduction. That is, the contribution of the unresolved variables is made to be a function only of larger-scale variables which can be feasibly simulated or consistently measured. Effectively, this means that the equations governing the parameterized small-scale processes lose whatever independence they had from the resolved processes. In the paper [61], Palmer uses ideas from dynamical systems theory (in particular, the Poincaré-Bendixson theorem) to show that in some circumstances, dimension-reducing parameterizations will necessarily yield a system which is not chaotic. Palmer points out that since the chaotic nature of the climate is a vital aspect of its long-term behavior, a loss of chaotic dynamics could be a confounding factor in long-term statistical fidelity. In other words, the (partial) independence of small-scale processes could be a fundamental component of the qualitative behavior of large-scale processes. Simplifying the small-scale subsystems with functional dependencies exclusively in terms of other variables could thus result in the loss of dynamical complexity in the climate model, and substantially change the qualitative behavior of long-term climate predictions.

Palmer proposed a solution to this issue, in which unresolved scales were parameterized by a stochastic variable rather than a deterministic model. Altering the system to have a stochastic component effectively corresponds to state space augmentation; that is, the state space of the parameterized system now includes the resolved variables and the event space associated with the stochastic variables. As a result, the act of approximating some component of the state space no longer makes the parameterized variable totally determined by other components of the system through a functional relationship, which means there is no longer necessarily an erasure of the chaotic behavior. The probability density function of the stochastic variable in Palmer’s example was based on some known information about the system (making its stochastic behavior mimic, in some sense, the deterministic behavior of the fully defined component).

More broadly, stochastic parameterization schemes provide a means of restoring the independence between resolved and unresolved degrees of freedom, while main-

taining computational tractability, by representing the unresolved degrees of freedom as realizations of a stochastic process [57, 53, 73, 21, 18, 6]. In systems exhibiting timescale separation, a common route to stochastic parameterization is to derive stochastic differential equations (SDEs) for the unresolved variables by taking homogenization limits of the primitive governing equations [62, 58, 47]. Alternatively, and particularly in systems where the unresolved dynamics are not consistent with SDEs, stochastic closure schemes are constructed by parameter inference from training data [68]. Recent works have used ideas from data assimilation [56, 51] to sequentially learn the parameters of stochastic closure models from noisy partial observations [16, 38, 17, 52].

In placing these methods and results in context, it should be kept in mind that stochasticity of the parameterized dynamics is not a necessary ingredient for successful subgrid-scale modeling—rather, it is the act of representing unresolved degrees of freedom by surrogate dynamical models (of either deterministic or stochastic nature) that can lead to improved performance over parameterization schemes based on pure functional relationships with the resolved variables. Indeed, in multiscale dynamical systems exhibiting averaging principles [62, 3], the effective slow dynamics is deterministic. The heterogeneous multiscale method [25] is a general multiscale modeling framework that leverages averaging principles to build microscale models for unresolved variables—in a broad range of applications, these models are deterministic. In atmospheric dynamics, one of the most successful approaches to parameterization, called super-parameterization, involves coupling a coarse atmospheric model with embedded column models of moist convection in each gridbox [40], and these models are again oftentimes (but not always [41]) deterministic.

1.2. Quantum mechanical data assimilation. QMDA is a technique for sequential data assimilation (filtering) of partially observed dynamical systems [56, 51], combining elements of Koopman operator theory [26] with the Dirac–von Neumann quantum mechanical evolution and measurement axioms [71]. In QMDA, the density operator from quantum mechanics is employed as a generalization of the probability distribution for the system state in Bayesian data assimilation, the assimilated observables are represented by self-adjoint multiplication operators, and dynamical evolution of observables takes place under the unitary action of the Koopman operator. When observations are made, the density is updated via a projective von Neumann measurement, which is analogous to the Bayesian analysis step. Thus, under the assumption that the assimilated signal is governed by a classical dynamical system, QMDA comprises a one-way-coupled classical-quantum system, where the classical system influences the state of the quantum system through the observation map but the quantum system does not influence the state of the classical system.

QMDA addresses a number of challenges in classical data assimilation, as it avoids the need for ad hoc Gaussian approximations, does not require diffusion regularization, and automatically preserves sign-definite quantities. Being rooted in linear operator theory, the method also has an asymptotically consistent, data-driven formulation, whereby operators are represented by matrices in a data-driven basis learned from time-ordered data using kernel algorithms [7, 31, 8, 23].

1.3. Our contributions. Building on the QMDA framework, we propose a data-driven technique for closure of dynamical systems that employs a quantum mechanical system as a surrogate model of the unresolved degrees of freedom. The surrogate quantum system evolves in tandem with the classical system for the resolved variables via two-way coupling, generalizing the one-way coupling in QMDA.

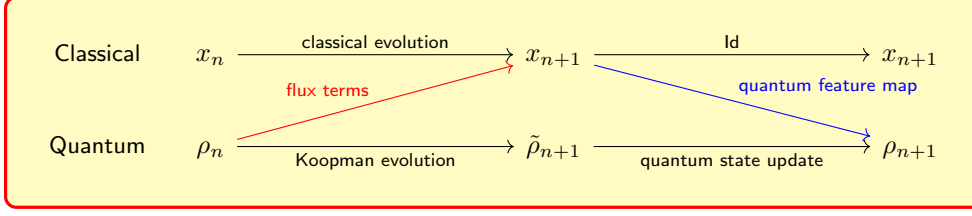


Fig. 1: Schematic representation of a QMCI cycle. The diagram illustrates the update procedure for the classical degrees of freedom (resolved variables) x_n and the quantum state (density operator) ρ_n over one timestep. We advance the resolved variables to their value x_{n+1} at time $t_{n+1} = t_n + \Delta t$ using the values x_n at time t_n and the flux terms obtained by evaluation of a quantum mechanical observable on the state ρ_n (red arrow). Moreover, we advance the quantum state ρ_n to a prior state $\tilde{\rho}_{n+1}$ at time t_{n+1} through a unitary evolution step induced by the Koopman operator. The state $\tilde{\rho}_{n+1}$ is then updated to the posterior ρ_{n+1} via a projective update (quantum Bayes’ rule) induced by a quantum feature map (blue arrow). The cycle is repeated to advance the coupled classical–quantum states (x_{n+1}, ρ_{n+1}) at later times.

A schematic overview of our approach, which we call Quantum Mechanical Closure (QMCI), is depicted in Fig. 1.

At any time t_n , the state of the quantum mechanical system is represented by a density operator ρ_n acting on a Hilbert space H_L of (finite) dimension L . The closure terms needed to advance the resolved variables x_n at time t_n to their state x_{n+1} at time $t_{n+1} = t_n + \Delta t$ are obtained by evaluation of a quantum mechanical observable A (i.e., a self-adjoint operator acting on H_L) on the state ρ_n . Intuitively, the density operator ρ_n can be thought of as a non-commutative analog of a classical probability density, and the evaluation of A on ρ_n is analogous to the evaluation of an expectation functional in classical probability theory. Thus, the update $x_n \mapsto x_{n+1}$ given ρ_n can be thought of as ensemble update based on the statistical information about the unresolved degrees of freedom encoded in ρ_n .

To advance ρ_n to the quantum state ρ_{n+1} at time t_{n+1} , we first employ a unitary evolution map, $\rho_{n+1} \mapsto \tilde{\rho}_{n+1}$, induced by the Koopman operator of the dynamical system [26]. Then, we update $\tilde{\rho}_{n+1} \mapsto \rho_{n+1}$ projectively given the resolved variables x_{n+1} using an operator-valued function that we call a quantum feature map. These steps will be described precisely below, but for now we note that the unitary Koopman evolution can be thought of as being analogous to the forecast step in data assimilation [56, 51]. In this analogy, the Koopman evolution leads to a “prior” state $\tilde{\rho}_{n+1}$, which is updated projectively to the “posterior” ρ_{n+1} given x_{n+1} analogously to the Bayesian analysis step in data assimilation. In quantum information theory, the values of the feature map used here to assimilate the resolved degrees of freedom are known as *quantum effects* [42]. Quantum effects generalize the notion of events in classical statistics.

The principal distinguishing aspects of QMCI are as follows.

1. We cast the problem of closure of dynamical systems into the framework of operator theory and quantum information theory. Non-abelian quantum systems are known to exhibit new types of behavior (such as entanglement and superposition), and offer greater capacity to encode information than classical

systems [37]. In particular, the dimension of the space of density operators on an L -dimensional Hilbert space is $O(L^2)$, whereas the dimension of the space of L -dimensional probability density vectors is $O(L)$. Our main premise is that the mathematical framework of quantum mechanics provides a flexible arena for building closure schemes for classical dynamical systems enjoying favorable structure preservation and asymptotic consistency properties.

2. Positivity preservation: Our procedure for constructing the coupled classical-quantum system depicted in Fig. 1 employs, as an intermediate step, an information-preserving embedding of the full dynamical system (i.e., both the resolved and unresolved degrees of freedom) into an infinite-dimensional quantum system. This system is projected to the finite-dimensional system on the Hilbert space H_L . The process of embedding the classical system into the infinite-dimensional quantum system *before* projecting into finite dimensions allows us to take advantage of properties of non-abelian operator spaces to ensure that the parameterization scheme is positivity preserving. That is, positive-definite flux terms from the unresolved variables to the resolved variables in the original system are represented by positive-definite operators in the QMCI-parameterized system (and similarly for negative-definite terms). This addresses an important problem in data-driven subgrid-scale modeling, where failure to preserve the sign of sign-definite quantities (e.g., moisture in an atmospheric circulation model) is recognized as a significant source of bias and numerical instability [75].
3. Data-driven formulation: QMCI employs a closely-related data-driven formulation to QMDA, which uses eigenfunctions of kernel integral operators as data-driven basis functions for representation of linear operators [7]. The training data requirements of QMCI are comparable to other data-driven closure schemes, and typically comprise of time series of the resolved variables and the unresolved fluxes. In what follows, we explore scenarios where training data for building the basis are either directly available from integrations of the full model (as would be the case, e.g., when coarsening a high-resolution climate model [11, 12, 75]), or they are constructed from the resolved variables (as would be the case, e.g., when learning residuals of imperfect models from observations of nature). In the latter scenario, we use delay-coordinate embedding techniques [66] to improve the richness of our approximation models. Using techniques for pointwise and spectral approximation of linear operators [15, 72], the data-driven QMCI models converge in the large-data limit to data-independent finite-dimensional models on the Hilbert space H_L . Increasing the dimension parameter L allows the finite-dimensional models to capture increasingly high-dimensional subgrid-scale dynamics.

In this paper, we describe the mathematical framework and associated computational algorithms of QMCI. Moreover, we demonstrate the behavior of the scheme in two test systems: the Lorenz 63 (L63) [54] and Lorenz 96 (L96) multiscale system [55, 27]. The L63 system was employed in [61] as a motivating example for stochastic parameterization. The L96 multiscale system has been employed as a prototype test system in several studies on parameterization and surrogate modeling, e.g., [21, 45, 14, 68].

1.4. Plan of the paper. In section 2, we state the parameterization problem under study. Section 3 gives an overview of the axioms of quantum mechanics. In section 4, we describe the construction of the quantum mechanical system that we will

use to model the unresolved degrees of freedom. This construction largely parallels the QMDA approach from [29]. In [section 5](#), we describe the QMCI parameterization scheme based on the quantum system from [section 4](#). This is followed by a description of the data-driven implementation of our approach in [section 6](#). In [sections 7 and 8](#), we present applications of QMCI to the L63 and L96 multiscale systems, respectively. [Section 9](#) contains a discussion and perspectives on future work. Details on numerical implementation and pseudocode are collected in [Appendix A](#).

2. Problem Statement. Consider a discrete-time dynamical system with state space Ω and evolution map $\Phi : \Omega \rightarrow \Omega$ preserving a probability measure μ . Suppose that the state space is decomposable as the product $\Omega = \mathcal{X} \times \mathcal{Y}$, where \mathcal{X} and \mathcal{Y} are state spaces for the resolved and unresolved degrees of freedom, respectively. Throughout the paper, we will assume that Ω is a “nice” (separable, completely metrizable) topological space, and μ is a Borel measure with compact support. Additional assumptions will be introduced as needed.

We view the Φ dynamics on Ω as being inaccessible to direct simulation, e.g., due to the dimension of \mathcal{Y} being prohibitively large, lack of complete knowledge of the evolution map Φ , or a combination thereof. The general problem of parameterization is to build a surrogate dynamical system $\tilde{\Phi} : \tilde{\Omega} \rightarrow \tilde{\Omega}$ on a state space $\tilde{\Omega} = \mathcal{X} \times \tilde{\mathcal{Y}}$ which is (i) feasible to integrate; and (ii) compatible with the evolution of the resolved degrees of freedom in \mathcal{X} . Here, $\tilde{\mathcal{Y}}$ is the state space of a surrogate model of the unresolved degrees of freedom in \mathcal{Y} .

Let $P_{\mathcal{X}} : \Omega \rightarrow \mathcal{X}$ and $\tilde{P}_{\mathcal{X}} : \tilde{\Omega} \rightarrow \mathcal{X}$ denote the canonical projection maps onto \mathcal{X} from Ω and $\tilde{\Omega}$, respectively. Let also $\alpha : \Omega \rightarrow \tilde{\Omega}$ be a map that assigns a dynamical state in $\tilde{\Omega}$ to each dynamical state in Ω . A parameterized system on $\tilde{\Omega}$ which is consistent with the original system on Ω would satisfy the following commutative diagram:

$$(2.1) \quad \begin{array}{ccccc} \Omega & & \xrightarrow{\Phi} & & \Omega \\ & \searrow P_{\mathcal{X}} & & \swarrow P_{\mathcal{X}} & \\ & & X & & X \\ & \nearrow \tilde{P}_{\mathcal{X}} & & \nwarrow \tilde{P}_{\mathcal{X}} & \\ \tilde{\Omega} & & \xrightarrow{\tilde{\Phi}} & & \tilde{\Omega} \end{array} \quad \begin{array}{c} \downarrow \alpha \\ \downarrow \alpha \end{array}$$

This diagram represents the fact that for initial conditions $\tilde{\omega} = \alpha(\omega) \in \tilde{\Omega}$ that are consistent with $\alpha \in \Omega$ in terms of the resolved variables, i.e., $\tilde{P}_{\mathcal{X}}(\tilde{\omega}) = P_{\mathcal{X}}(\omega)$, the $\tilde{\Phi}$ dynamics should produce consistent outcomes with Φ , (again, in terms of the resolved variables), i.e., $\tilde{P}_{\mathcal{X}} \circ \tilde{\Phi}(\tilde{\omega}) = P_{\mathcal{X}} \circ \Phi(\omega)$. In practice, such a strong form of consistency is seldom achievable, and one seeks to identify an appropriate state space $\tilde{\mathcal{Y}}$ and dynamics $\tilde{\Phi}$ such that (2.1) holds as closely as possible in some sense, e.g., in terms of low-order statistics such as probability distributions and time-autocorrelation functions of the resolved variables with respect to the invariant measure.

In general, it is advantageous to include any partial knowledge about the Φ dynamics in the construction of $\tilde{\Phi}$. To incorporate that possibility in our formalism, we introduce (without loss of generality) a space \mathcal{Z} and maps $\phi : \mathcal{X} \times \mathcal{Z} \rightarrow \mathcal{X}$ and $Z : \mathcal{Y} \rightarrow \mathcal{Z}$ such that

$$P_{\mathcal{X}} \circ \Phi(\omega) = \phi(x, Z(y)), \quad \omega = (x, y).$$

Here, ϕ captures the functional form of the evolution map for the resolved variables

conditioned on a function Z (a “flux term”) of the unresolved variables. Assuming that ϕ is known, we can construct $\tilde{\Phi}$ as a map of the form

$$(2.2) \quad \tilde{\Phi}(x, \tilde{y}) = (\phi(x, \tilde{Z}(\tilde{y}), \tilde{\psi}(x, \tilde{y})),$$

where $\tilde{\psi} : \mathcal{X} \times \tilde{\mathcal{Y}} \rightarrow \tilde{\mathcal{Y}}$ represents the evolution of the surrogate unresolved variables \tilde{y} given the resolved variables x , and $\tilde{Z} : \tilde{\mathcal{Y}} \rightarrow \mathcal{Z}$ is a function acting as a surrogate for Z . If ϕ is not known, we replace (2.2) by

$$(2.3) \quad \tilde{\Phi}(x, \tilde{y}) = (\tilde{\phi}(x, \tilde{Z}(\tilde{y}), \tilde{\psi}(x, \tilde{y})),$$

where $\tilde{\phi} : \mathcal{X} \times \mathcal{Z} \rightarrow \mathcal{X}$ is an approximation of ϕ .

2.1. Examples. We outline how some of the commonly used parameterization schemes fit within the framework described above.

2.1.1. Deterministic functional closure. In closure schemes modeling the unresolved variables through functional relationships with the resolved variables, we formally set $\tilde{\mathcal{Y}} = \mathcal{X}$, so that the flux term $\tilde{Z} : \mathcal{X} \rightarrow \mathcal{Z}$ becomes a function of the resolved variables. The map $\tilde{\psi}(x, \tilde{y})$ is also formally set to a copy of $\phi(x, \tilde{Z}(\tilde{y}))$ so it need not be explicitly retained in calculations. A number of the classical parameterization schemes (e.g., [1, 30] in geophysical fluid dynamics) derive \tilde{Z} heuristically using prior physical knowledge of the problem at hand. For certain classes of systems exhibiting timescale separation between the x and y variables, \tilde{Z} can be systematically obtained from the governing equations of the original system using asymptotic analysis techniques such as averaging [62]. In data-driven approaches, the function \tilde{Z} is constructed via a supervised learning algorithm using $(x, Z(y))$ pairs as training data; e.g., [12, 11, 75].

2.1.2. Stochastic closure. To treat stochastic parameterization schemes, we set $\tilde{\mathcal{Y}}$ to a probability sample space, $\tilde{Z} : \tilde{\mathcal{Y}} \rightarrow \mathcal{Z}$ to a random variable, and choose $\tilde{\psi}$ such that $\{\tilde{\Phi}^n : n \in \mathbb{N}\}$ defines a stochastic process over $\tilde{\Omega}$. As a concrete example, we may understand Palmer’s Gaussian-distributed stochastic closure of the L63 system [61] in this framework, as follows.

In a coordinate system obtained via empirical orthogonal function (EOF) analysis, the L63 governing equations with the standard parameter values become

$$(2.4) \quad \begin{aligned} \dot{a}_1 &= v_1(a_1, a_2, a_3) := 2.3 a_1 - 6.2 a_3 - 0.49 a_1 a_2 - 0.57 a_2 a_3, \\ \dot{a}_2 &= v_2(a_1, a_2, a_3) := -62 - 2.7 a_2 + 0.49 a_1^2 - 0.49 a_3^2 + 0.14 a_1 a_3, \\ \dot{a}_3 &= v_3(a_1, a_2, a_3) := -0.63 a_1 - 13 a_3 + 0.43 a_1 a_2 + 0.49 a_2 a_3, \end{aligned}$$

where the coordinates a_1 , a_2 , and a_3 have decreasing variance. Let $\Omega = \mathbb{R}^3$ and $\Phi^t : \Omega \rightarrow \Omega$ with $t \in \mathbb{R}$ be the flow generated by (2.4). In this example, we consider the discrete-time system $\Phi : \Omega \rightarrow \Omega$ with $\Phi = \Phi^{\Delta t}$ induced by the continuous-time flow at a fixed timestep Δt as the “true” dynamics. Moreover, we let $\Omega = \mathcal{X} \times \mathcal{Y}$ with $x = (a_1, a_2) \in \mathcal{X} \equiv \mathbb{R}^2$ and $y = a_3 \in \mathcal{Y} \equiv \mathbb{R}$ represent the resolved and unresolved variables, respectively. The corresponding flux term is $Z : \mathcal{Y} \rightarrow \mathcal{Z}$ with $\mathcal{Z} = \mathbb{R}$ and $Z(y) = y$. As approximate resolved dynamics, we employ the map $\tilde{\phi} : \mathcal{X} \times \mathcal{Z} \rightarrow \mathcal{X}$ obtained by a forward Euler discretization of (2.4) at the timestep Δt ; that is, we have

$$\tilde{\phi}(x, z) = x + (v_1(x, z), v_2(x, z)) \Delta t.$$

In Palmer’s approach, the evolution of the a_3 variable is approximated by an i.i.d. Gaussian process. To represent this process within the framework described

above, we let $\tilde{\mathcal{Y}} = \mathbb{R}^{\mathbb{N}}$ be a space of \mathbb{R} -valued sequences equipped with a σ -algebra $\Sigma_{\tilde{\mathcal{Y}}}$ of cylinder sets and a shift-invariant Gaussian measure $\nu : \Sigma_{\tilde{\mathcal{Y}}} \rightarrow [0, 1]$. That is, ν has the properties that (i) $\nu \circ T^{-1} = \nu$, where $T : \tilde{\mathcal{Y}} \rightarrow \tilde{\mathcal{Y}}$ is the shift map, $T(\tilde{y}_0, \tilde{y}_1, \dots) = (\tilde{y}_1, \tilde{y}_2, \dots)$; and (ii) $\tilde{Z}_0, \tilde{Z}_1, \dots$ with $\tilde{Z}_n = u \circ T^n$ are i.i.d. Gaussian random variables with equal variance. Here, $u : \tilde{\mathcal{Y}} \rightarrow \mathcal{Z}$ projects onto the first component, $u(\tilde{y}_0, \tilde{y}_1, \dots) = \tilde{y}_0$, and the measure ν is chosen such that Z_n has variance equal to the variance of a_3 . With these definitions, the parameterized dynamics from (2.3) becomes $\tilde{\Phi}(x, \tilde{y}) = (\tilde{\phi}(x, \tilde{Z}(\tilde{y}), \tilde{\psi}(x, \tilde{y})))$, with $\tilde{\psi}(x, \tilde{y}) = u(T(\tilde{y}))$.

Palmer observed that with this approach the parameterized x dynamics recovers the qualitative features of the (a_1, a_2) variables of the full L63 system, including the characteristic lobes of the Lorenz attractor projected onto the (a_1, a_2) plane; see [61, Figure 2] and Figure 7a below. In particular, since the state space $\tilde{\Omega}$ of the stochastically parameterized system is formally infinite-dimensional, the method is able to overcome theoretical limitations of a deterministic functional closure on $\mathcal{X} = \mathbb{R}^2$, which by the Poincaré-Bendixson theorem cannot exhibit chaos in continuous time under smooth dynamics.

In section 7, we will use Palmer's L63 closure scheme as a reference example to assess the performance of QMCl. Certain classes of SDE schemes derived via homogenization principles [62] can similarly be understood as a state-space augmentation of the resolved variables space \mathcal{X} to include the sample space of a Brownian motion driving the parameterized system.

3. Overview of quantum mechanics. As a statistical theory, quantum mechanics can be looked at as a generalization of Bayesian probability theory [44, 42]. Quantum mechanics deals directly with objects (e.g., quantum particles) for which a measurement of any observable at a given time is inherently probabilistic in nature. The theory of quantum mechanics deals with understanding how the generalized probability distributions associated with these objects (which, in some views, constitute the objects themselves) evolve over time and under experimental observations of the objects' properties. The probability theory associated with quantum systems, however, is generalized beyond classical probability theory. Quantum probabilistic dynamics are understood through non-abelian algebras of operators on Hilbert spaces and spectral theory applied to these operators. The QMDA methodology arises from a parallel between the probabilistic dynamics formulated in this way and the mathematical structure of dynamical systems and Koopman operator theory [32, 29].

A standard framework of quantum probabilistic dynamics arises from the Dirac-von Neumann quantum mechanical axioms. In this section, we provide an overview of the mathematical objects and evolution rules associated with this theory in order to get a general view of how the mathematical systematization of quantum mechanics can be applied to dynamical systems more broadly. More detailed explication of the foundations of this theory can be found, e.g., in [71].

3.1. Hilbert spaces and quantum observables. In the Dirac-von Neumann framework, associated to every quantum system is a Hilbert space $(\mathcal{H}, \langle \cdot, \cdot \rangle)$ over the complex numbers. The precise choice of \mathcal{H} will depend on the specific system being studied. Quantum observables are defined as elements of the set of self-adjoint (possibly unbounded) linear operators $A : D(A) \rightarrow \mathcal{H}$, where the domain $D(A)$ of A is a dense subspace of \mathcal{H} .

Every quantum observable is associated with a measurable real-valued quantity of the quantum system (such as momentum, spin, etc.). Importantly, if the quantity associated with a quantum observable A is measured in an experimental setting, the

possible values of the measurement are contained in the spectrum of A . The self-adjointness condition ensures that such measurements are real-valued.

Let $B(\mathcal{H})$ be the space of bounded operators on \mathcal{H} . From the spectral theorem for self-adjoint operators, associated with every quantum observable $A : D(A) \rightarrow \mathcal{H}$ is an operator-valued measure $E_A : \mathcal{B}(\mathbb{R}) \rightarrow B(\mathcal{H})$ on the Borel σ -algebra $\mathcal{B}(\mathbb{R})$ over \mathbb{R} such that (i) for every Borel set $S \in \mathcal{B}(\mathbb{R})$, $E_A(S)$ is an orthogonal projection; (ii) $E(\emptyset) = 0$; (iii) $E_A(\mathbb{R}) = \text{Id}$; and (iv) for every countable collection $\{S_i\}$ of pairwise-disjoint sets $S_i \in \mathcal{B}(\mathbb{R})$, we have $E_A(\bigcup_i S_i) = \sum_i E_A(S_i)$, where the sum over i converges in the strong topology of $B(\mathcal{H})$. Using E_A , one can reconstruct the operator A through the spectral integral $A = \int_{\mathbb{R}} a dE_A(a)$.

The measure E_A plays an important role in calculations, and it can be resolved as a finite discrete sum of projections for QMCI applications (see [subsection 4.3](#)). In the general theory, however, the spectrum of A has a continuous component and A cannot be finitely resolved in this way. Unlike classical observables lying in commutative algebras of functions, quantum observables do not, in general, commute. One of the signature characteristics of quantum mechanics arises from this fact—non-commutative observables cannot be measured simultaneously at arbitrarily high precision, giving rise to the famed uncertainty principle.

3.2. Quantum states. Let $B_1(\mathcal{H}) \subseteq B(\mathcal{H})$ be the space of trace class operators on \mathcal{H} . The quantum states of the system are defined as elements of the set $Q(\mathcal{H}) \subseteq B_1(\mathcal{H})$ consisting of all positive, trace class operators of unit trace, i.e.,

$$Q(\mathcal{H}) = \{\rho \in B_1(\mathcal{H}) \mid \text{tr } \rho = 1, \rho \geq 0\}.$$

Such operators $\rho \in Q(\mathcal{H})$ are known as density operators. Quantum states can be thought of as roughly analogous to classical probability densities in an L^1 space, representing the degree of knowledge about the system's current state. With this in mind, a density operator's positivity and unity of trace can be thought of as analogous to the positivity and normalization of a classical probability density. We say that $\rho \in Q(\mathcal{H})$ is a pure state if there exists a unit vector $\xi \in \mathcal{H}$ such that $\rho = \langle \xi, \cdot \rangle \xi$, i.e., ρ is a rank-1 projection along ξ . Otherwise, ρ is said to be mixed.

Every quantum state $\rho \in Q(\mathcal{H})$ induces a continuous, positive linear functional $\mathbb{E}_\rho : B(\mathcal{H}) \rightarrow \mathbb{C}$ on bounded operators defined as

$$(3.1) \quad \mathbb{E}_\rho A = \text{tr}(\rho A);$$

intuitively, we think of this formula as being analogous to an expectation with respect to a classical probability density. If A is a self-adjoint quantum observable (not necessarily bounded), the associated projection-valued measure E_A induces a probability distribution for experimental measurements of A . Specifically, the probability that a measurement $a \in \mathbb{R}$ of the quantum observable A lies in a Borel set $S \in \mathcal{B}(\mathbb{R})$ is given by

$$(3.2) \quad \mathbb{P}_{\rho, A}(a \in S) = \mathbb{E}_\rho E_A(S).$$

This general formula holds for all quantum observables, and thus the quantum state ρ alone determines the probability distribution of all quantum observables of a system.

3.3. Quantum evolution and measurement. In the Dirac-von Neumann axioms, there are two evolution rules for the quantum state. The first is the time-evolution equation. Letting \mathcal{T} denote either \mathbb{Z} or \mathbb{R} , respectively for discrete- or

continuous-time systems, suppose that $\rho_0 \in Q(\mathcal{H})$ is the initial quantum state of a system, and ρ_t the quantum state of the system at a time $t \in \mathcal{T}$ such that no intervening measurement took place. The quantum mechanical time evolution axiom posits that there exists a group of unitary operators $\{U^t \in B(\mathcal{H})\}_{t \in \mathcal{T}}$ such that

$$(3.3) \quad \rho_t = \mathcal{P}^t \rho_0 := U^{t*} \rho_0 U^t.$$

The collection $\{\mathcal{P}^t\}_{t \in \mathcal{T}}$ extends to an evolution group on $B_1(\mathcal{H})$, which can be thought of as an analog of the group of transfer operators of a measure-preserving dynamical system [4] acting on densities in L^1 . If the quantum system under study is open, i.e., it is allowed to interact with its environment, (3.3) is replaced by evolution under a semigroup $\{\mathcal{P}^t : B_1(\mathcal{H}) \rightarrow B_1(\mathcal{H})\}_{t \in \mathcal{T}_+}$ which is required to be trace non-increasing, i.e., we have $\text{tr}(\mathcal{P}^t \rho) \leq 1$ rather than the stronger property $\text{tr}(\mathcal{P}^t \rho) = 1$ under (3.3). In either case, the evolution of quantum states under \mathcal{P}^t is dual to the evolution of quantum observables given by the operators $\mathcal{U}^t : B(\mathcal{H}) \rightarrow B(\mathcal{H})$ with

$$(3.4) \quad \mathcal{U}^t A = U^t A U^{t*};$$

i.e., we have $\mathbb{E}_{\mathcal{P}^t \rho_0} A = \mathbb{E}_{\rho_0}(\mathcal{U}^t A)$. In quantum mechanics, the evolution of states and observables in (3.3) and (3.4) is known as the Schrödinger and Heisenberg picture, respectively.

The second evolution rule addresses how measurements of quantum observables affect the quantum state. Suppose a quantum system is in the state $\rho \in Q(\mathcal{H})$ at a time t , and a quantum observable A is measured at the time t . Then, if the measurement takes a value $a \in \mathbb{R}$ such that $E_A(\{a\}) \neq 0$ (which necessarily means that a is an eigenvalue of A), the quantum state of the system is now given by $\rho|_a \in Q(\mathcal{H})$, where

$$(3.5) \quad \rho|_a = \frac{E_A(\{a\}) \rho E_A(\{a\})}{\text{tr}(E_A(\{a\}) \rho E_A(\{a\}))}.$$

The update $\rho \mapsto \rho|_a$ is oftentimes referred to as a von Neumann measurement, and can be thought of as an analog of the Bayesian conditioning rule of classical probability theory.

In (3.5), the projections $E_A(\{a\})$ are examples of quantum effects, defined as the operators in the set

$$(3.6) \quad \mathcal{E}(\mathcal{H}) = \{e \in B(\mathcal{H}) \mid 0 \leq e \leq \text{Id}\}.$$

Intuitively, one can think of effects as analogous to events in classical probability theory. The projections $e \in \mathcal{E}(\mathcal{H})$ represent events which are “sharp”, in the sense that $e^2 = e$, whereas other effects such that $e^2 < e$ can be thought of as being “fuzzy”.

A generalization of (3.5) that represents conditioning of ρ by an arbitrary effect $e \in \mathcal{E}(\mathcal{H})$ is

$$(3.7) \quad \rho|_e = \frac{\sqrt{e} \rho \sqrt{e}}{\text{tr}(\sqrt{e} \rho \sqrt{e})}.$$

This update rule reduces to (3.5) when $e = e^2 = E_A(\{a\})$ is a projection. In applications involving physical quantum systems, (3.7) is used to model the state change of a quantum system being measured due to interactions with the measuring apparatus, a process sometimes called “state collapse”. Equation (3.7), however, also applies more broadly as an inference rule within abstract quantum probability theory [67], which is how we will use it in our quantum mechanical closure schemes.

4. Quantum mechanical representation of classical dynamics. In this section, we construct the quantum mechanical system that we will use to model the unresolved degrees of freedom in QMCI. Our goal is to build a quantum system on a finite-dimensional Hilbert space, H_L , and use the quantum state space of this system as the state space of the surrogate dynamical model for the unresolved degrees of freedom, i.e., $\tilde{\mathcal{Y}} = Q(H_L)$ in the notation of [section 2](#). Following the QMDA approach [\[29\]](#), the first step in this construction is a formal embedding of the classical dynamics on Ω into a quantum system associated with an infinite-dimensional Hilbert space, H . Under this embedding, classical observables (functions of the state) are represented by quantum mechanical observables, and classical probability densities are represented by quantum density operators. We describe this embedding in [subsection 4.2](#), following a brief overview of relevant definitions from Koopman and transfer operator theory. In [subsection 4.3](#), we construct finite-dimensional quantum systems by discretization (i.e., finite-dimensional projection) of the infinite-dimensional system, choosing $H_L \subset H$ as an L -dimensional space in a nested family of finite-dimensional subspaces associated with an orthonormal basis of H . In [subsection 4.4](#), we make explicit our choice of basis leading to the construction of H_L .

4.1. Koopman and transfer operators. The measure-preserving dynamical system $\Phi : \Omega \rightarrow \Omega$ induces groups of linear operators $U^n : L^p(\mu) \rightarrow L^p(\mu)$ on the L^p spaces associated with the invariant measure, acting by composition with the dynamical flow, $U^n f = f \circ \Phi^n$ with $n \in \mathbb{Z}$. These operators are known as Koopman operators [\[49, 26\]](#), and preserve the $L^p(\mu)$ norm for any $p \in [0, \infty]$ since μ is an invariant measure under Φ . In the Hilbert space case, $H := L^2(\mu)$, the Koopman operators are unitary, i.e., $(U^n)^* = U^{-n}$ for any $n \in \mathbb{Z}$. We define the inner product of H as $\langle f, g \rangle := \int_{\Omega} f^* g d\mu$, and use the notations $\|f\|_{L^p(\mu)} := (\int_{\Omega} |f|^p d\mu)^{1/p}$ for $p \in [1, \infty)$ and $\|f\|_{L^\infty(\mu)} = \lim_{p \rightarrow \infty} \|f\|_{L^p(\mu)}$ for the standard $L^p(\mu)$ norms.

Identifying $L^p(\mu)$, $p \in (1, \infty]$, with the dual of $L^q(\mu)$, $q \in [1, \infty)$, with $\frac{1}{p} + \frac{1}{q} = 1$, we have that $U^n : L^p(\mu) \rightarrow L^p(\mu)$ is the adjoint (dual) of the operator $P^n : L^q(\mu) \rightarrow L^q(\mu)$ with $P^n f = f \circ \Phi^{-n}$, known as the transfer operator [\[4\]](#). If we further identify $L^q(\mu)$ as the space of finite Borel measures on Ω with densities in $L^q(\mu)$, denoted here as $M_q(\mu)$, the transfer operator can be identified with the pushforward map $\Phi_*^n : M_q(\mu) \rightarrow M_q(\mu)$, where $\Phi_*^n \nu = \nu \circ \Phi^{-n}$. That is, if $\nu \in M_q(\mu)$ has density $\varrho = \frac{d\nu}{d\mu} \in L^q(\mu)$, then the measure $\Phi_*^n \nu$ has density $\frac{d\Phi_*^n \nu}{d\mu} = P^n \varrho$.

Koopman and transfer operators are central analytical tools in ergodic theory [\[4, 26\]](#). In recent years, they have found widespread use in data-driven analysis and forecasting methodologies for dynamical systems; e.g., [\[24, 59, 64, 74, 13, 48, 8\]](#). We will be addressing aspects of data-driven approximation in [section 6](#), but for the remainder of this section our focus will be on quantum mechanical systems induced by the unitary Koopman operators on H and its subspaces.

4.2. Embedding into an infinite-dimensional quantum system. The unitary Koopman evolution group $\{U^n \in B(H)\}_{n \in \mathbb{Z}}$ induces a quantum system on H with states $Q(H) \subset B_1(H)$ as described in [section 3](#). Moreover, we can identify the unitary evolution of states in [\(3.3\)](#) with an induced action of the Koopman operator; that is,

$$\rho_n = \mathcal{P}^n \rho_0 := U^{n*} \rho_0 U^n,$$

where $\rho_0 \in Q(H)$ is the initial state and we set $t \equiv n \in \mathbb{Z}$ since we work in discrete time. This quantum system can be brought into correspondence with the underlying classical dynamical system, as follows.

4.2.1. Von Neumann algebras. Consider the space of classical observables $L^\infty(\mu)$. In addition to being a Banach space as the other $L^p(\mu)$ spaces, $L^\infty(\mu)$ has the distinguished property of being a von Neumann algebra [70] with respect to pointwise function multiplication and complex conjugation. This means:

1. For any $f, g \in L^\infty(\mu)$, the pointwise product fg lies in $L^\infty(\mu)$, and we have

$$\|fg\|_{L^\infty(\mu)} \leq \|f\|_{L^\infty(\mu)}\|g\|_{L^\infty(\mu)}, \quad \|f^*f\|_{L^\infty(\mu)} = \|f\|_{L^\infty(\mu)}^2,$$

making $L^\infty(\mu)$ a C^* -algebra.

2. $L^\infty(\mu)$ is the continuous dual of the Banach space $L^1(\mu)$, making it a von Neumann algebra.

By commutativity of function multiplication, $L^\infty(\mu)$ is an abelian algebra. Given a probability density $p \in L^1(\mu)$, i.e., a positive function satisfying the normalization condition $\int_\Omega p d\mu = 1$, we have a continuous, positive linear functional $\mathbb{E}_p : L^\infty(\mu) \rightarrow \mathbb{C}$, defined as the expectation

$$\mathbb{E}_p f = \int_\Omega p f d\mu.$$

Letting $P(\mu) \subset L^1(\mu)$ be the space of probability densities in $L^1(\mu)$, i.e.,

$$P(\mu) = \{p \in L^1(\mu) \mid p \geq 0, \int_\Omega p d\mu = 1\},$$

we can think of elements of $P(\mu)$ as states of the algebra $L^\infty(\mu)$.

The similarities between this construction and the construction of quantum states from [subsection 3.2](#) is not accidental. Given a Hilbert space \mathcal{H} , the space $B(\mathcal{H})$ is a Banach space equipped with the operator norm, $\|A\|_{B(\mathcal{H})} = \sup_{u \in \mathcal{H}} \frac{\|Au\|_{\mathcal{H}}}{\|u\|_{\mathcal{H}}}$, and it is a von Neumann algebra with respect to operator composition and adjunction. This means:

1. For any $A, B \in B(\mathcal{H})$, the operator product AB lies in $B(\mathcal{H})$, and we have

$$\|AB\|_{B(\mathcal{H})} \leq \|A\|_{B(\mathcal{H})}\|B\|_{B(\mathcal{H})}, \quad \|A^*A\|_{B(\mathcal{H})} = \|A\|_{B(\mathcal{H})}^2,$$

making $B(\mathcal{H})$ a C^* -algebra.

2. $B(\mathcal{H})$ is the continuous dual of the Banach space $B_1(\mathcal{H})$, equipped with the trace norm $\|A\|_{B_1(\mathcal{H})} = \text{tr} \sqrt{A^*A}$, making it a von Neumann algebra.

Aside from trivial cases, the algebra $B(\mathcal{H})$ is non-abelian, which is a fundamental reason for differences in behavior between classical and quantum systems.

4.2.2. Embedding observables. Setting $\mathcal{H} = H \equiv L^2(\mu)$, the abelian algebra $L^\infty(\mu)$ embeds naturally and isometrically into $B(H)$ through its regular representation, i.e., the map $\pi : L^\infty(\mu) \rightarrow B(H)$ that maps elements of $L^\infty(\mu)$ to multiplication operators in $B(H)$, i.e.,

$$(\pi f)g = fg, \quad \forall g \in H.$$

This map is a $*$ -homomorphism of $L^\infty(\mu)$, i.e.,

$$\pi 1_\Omega = \text{Id}, \quad \pi(fg) = (\pi f)(\pi g), \quad \pi(f^*) = (\pi f)^*,$$

where f, g are arbitrary elements of $L^\infty(\mu)$ and $1_\Omega \in L^\infty(\mu)$ is the element equal to 1 μ -a.e. Note that πf is self-adjoint if and only if f is real-valued (i.e., f is a self-adjoint element of the $L^\infty(\mu)$ algebra), and πf is a positive operator if and only if $f \geq 0$ μ -a.e. Moreover, the spectrum of the multiplication operator πf is equal to the essential range of f , which corresponds to the values of f that have nonzero probability of occurring with respect to μ .

One can also verify that π is dynamically compatible with the evolution of classical observables under the Koopman operators $U^n : L^\infty(\mu) \rightarrow L^\infty(\mu)$ and the induced evolution $\mathcal{U}^n : B(H) \rightarrow B(H)$ from (3.4); that is, we have $\mathcal{U}^n \circ \pi = \pi \circ U^n$. This compatibility relationship is exhibited by the following commutative diagram:

$$\begin{array}{ccc} L^\infty(\mu) & \xrightarrow{U^n} & L^\infty(\mu) \\ \pi \downarrow & & \downarrow \pi \\ B(H) & \xrightarrow{\mathcal{U}^n} & B(H) \end{array}$$

4.2.3. Embedding states. The states of $L^\infty(\mu)$ can similarly be consistently embedded into states of $B(H)$ by means of the map $\Gamma : P(\mu) \rightarrow Q(H)$ that maps a probability density p to the pure state that projects along the square root of p , i.e.,

$$(4.1) \quad \Gamma(p) = \langle \sqrt{p}, \cdot \rangle \sqrt{p}.$$

Note that \sqrt{p} is a unit vector in $H = L^2(\mu)$ since p is a probability density in $L^1(\mu)$. Analogously to π , the map Γ is compatible with the evolution of probability densities under the transfer operator $P^n : P(\mu) \rightarrow P(\mu)$ and the induced operator $\mathcal{P}^n : Q(H) \rightarrow Q(H)$ from (3.3); that is, we have $\mathcal{P}^n \circ \Gamma = \Gamma \circ P^n$, and the following diagram commutes:

$$\begin{array}{ccc} P(\mu) & \xrightarrow{P^n} & P(\mu) \\ \Gamma \downarrow & & \downarrow \Gamma \\ Q(H) & \xrightarrow{\mathcal{P}^n} & Q(H) \end{array}$$

Overall, we have the following compatibility relationship between classical and quantum time evolution:

$$(4.2) \quad \mathbb{E}_{\mathcal{P}^n(\Gamma p)}(\pi f) = \mathbb{E}_{P^n p} f, \quad \forall f \in L^\infty(\mu), \quad \forall p \in P(\mu).$$

Note that, in general, Γ is not an onto map even if one restricts attention to pure states in $Q(H)$; this follows from the fact that there exist unit vectors in H which are not square roots of positive functions in $L^1(\mu)$. In other words, there are pure states in $Q(H)$ which have no underlying classical probability distribution in $P(\mu)$.

4.2.4. Embedding effects. Together, the maps π and Γ provide a consistent representation of Bayesian conditioning of probability densities by events in terms of conditioning of quantum states by effects.

Let $S \subseteq \Omega$ be a measurable subset of Ω (an event) and let $p \in P(\mu)$ be a probability density such that $\int_\Omega p \chi_S d\mu > 0$, where χ_S is the characteristic function of S . According to Bayes' theorem, the posterior density to p given S is

$$(4.3) \quad p|_S = \frac{\chi_S p}{\int_\Omega p \chi_S d\mu}.$$

Interpreting χ_S as an effect of the abelian algebra $L^\infty(\mu)$ (in the sense that $0 \leq \chi_S \leq 1_\Omega$; cf. (3.6)), and rewriting $\chi_S p = \chi_S p \chi_S$, it is apparent that (4.3) and (3.5) are manifestations of the same state conditioning procedure, the former being abelian and the latter being non-abelian. In particular, $\pi \chi_S$ is an effect in $\mathcal{E}(H)$, and we have the compatibility relation

$$(4.4) \quad \Gamma(p|_S) = (\Gamma p)|_{\pi \chi_S}.$$

By (4.2) and (4.4), we conclude that the infinite-dimensional quantum system on H consistently reproduces the statistical behavior of the underlying classical dynamical system on $L^1(\mu)$.

4.3. Discretization. Let $\{\phi_0, \phi_1, \dots\}$ be an orthonormal basis of H , and let $H_L \subset H$ be the L -dimensional subspace defined as

$$(4.5) \quad H_L = \text{span}\{\phi_0, \dots, \phi_{L-1}\}.$$

Deferring the task of choosing $\{\phi_l\}$ to [subsection 4.4](#), we construct finite-dimensional quantum systems on H_L by discretization (i.e., projection) of the infinite-dimensional system on H , as follows.

4.3.1. Discretization of observables. Let $\Pi_L : H \rightarrow H$ be the orthogonal projection with $\text{ran } \Pi_L = H_L$. When convenient, we will view Π_L as a map into H_L without change of notation. The projection Π_L induces a projection $\mathbf{\Pi}_L : B(H) \rightarrow B(H)$ defined as $\mathbf{\Pi}_L A = \Pi_L A \Pi_L$. The range of $\mathbf{\Pi}_L$ can be canonically identified with $B(H_L)$, i.e., the space of linear maps on H_L , so we can consider $\mathbf{\Pi}_L : B(H) \rightarrow B(H_L)$ as a map from (bounded) quantum observables on H to quantum observables on H_L (which are necessarily bounded since H_L is finite-dimensional). An important property of $\mathbf{\Pi}_L$ is that it is a positive map, i.e., it maps positive operators in $B(H)$ to positive operators in $B(H_L)$. This is in contrast to Π_L , which in general does not map positive functions to positive functions.

As a von Neumann algebra, $B(H_L)$ is isomorphic to the L^2 -dimensional algebra of $L \times L$ complex matrices, which we denote as \mathbb{M}_L . Such an isomorphism $\beta_L : B(H_L) \rightarrow \mathbb{M}_L$ is non-canonical since it depends on a choice of basis for H_L , but for our purposes a natural choice is to define β_L as the map that yields the matrix representation of operators in $B(H_L)$ with respect to the $\{\phi_l\}$ basis; that is, we set $\beta_L A = \mathbf{A}$, where $\mathbf{A} = [A_{ij}]_{i,j=0}^{L-1}$ is the $L \times L$ matrix with elements $A_{ij} = \langle \phi_i, A \phi_j \rangle$.

Using the quantum representation of classical observables $\pi : L^\infty(\mu) \rightarrow B(H)$ from [subsection 4.2.2](#), we define a projected representation $\pi_L : L^\infty(\mu) \rightarrow B(H_L)$ and its matrix-valued counterpart $\pi_L : L^\infty(\mu) \rightarrow \mathbb{M}_L$ as $\pi_L = \mathbf{\Pi}_L \circ \pi$ and $\pi_L = \beta_L \circ \pi_L$, respectively. By positivity of π , $\mathbf{\Pi}_L$, and β_L , the maps π_L and π_L are both positive, i.e., they map positive functions to positive operators and positive matrices, respectively. For a real-valued element $f \in L^\infty(\mu)$, $\pi_L f$ is a finite-rank symmetric operator with a spectrum $\{a_0, \dots, a_J\} \subset \mathbb{R}$ of real eigenvalues that can be loosely thought of a “discretization” of the essential range of f . The corresponding spectral measure $E_{\pi_L f} : \mathcal{B}(\mathbb{R}) \rightarrow B(H_L)$ is given by

$$(4.6) \quad E_{\pi_L f}(S) = \sum_{j: a_j \in S} E_{\pi_L f}^{(j)},$$

where $E_{\pi_L f}^{(j)} \in B(H_L)$ is the orthogonal projection onto the eigenspace of $\pi_L f$ corresponding to a_j .

Equation (4.6) may be used to compute the measurement probability from (3.2) given a quantum state $\rho \in Q(H_L)$, viz.

$$(4.7) \quad \mathbb{P}_{\rho, \pi_L f}(S) = \sum_{j: a_j \in S} \text{tr} \left(\rho E_{\pi_L f}^{(j)} \right).$$

As $L \rightarrow \infty$, the operators $\pi_L f$ exhibit spectral convergence to the multiplication operator πf in a suitable sense; see [29] for further details.

It is important to note that for a general element $f \in L^\infty(\mu)$, the matrix representation $\pi_L f$ is not diagonal; that is, the range of π_L is not included in an abelian subalgebra of \mathbb{M}_L (every such subalgebra would only contain diagonal matrices). This is in contrast to π which, being an algebra homomorphism, maps $L^\infty(\mu)$ to an abelian subalgebra of $B(H)$ (consisting of multiplication operators). Thus, as a result of discretization, our representation of classical observables by the finite-dimensional quantum system exhibits non-abelian behavior, which is an intrinsically quantum mechanical property.

4.3.2. Discretization of states. For a given quantum state $\rho \in Q(H)$, let $\sigma_0, \sigma_1, \dots$ be the projected operators $\sigma_L = \Pi_L \rho \in B(H)$. While, in general, the σ_L are not density operators, as $L \rightarrow \infty$ they converge to ρ in the trace norm of $Q(H)$. As a result, there exists $L_* \in \mathbb{N}$ such that for every $L > L_*$, we have $C_L = \text{tr } \sigma_L > 0$, and thus

$$(4.8) \quad \rho_L := \frac{\sigma_L}{C_L}$$

is a quantum state in $Q(H)$. Every such state can be identified with a state of $Q(H_L)$. As one can directly verify, for every quantum observable A , we have

$$(4.9) \quad \lim_{L \rightarrow \infty} \mathbb{E}_{\rho_L} A_L = \mathbb{E}_\rho A,$$

where $A = \Pi_L A$, so, in the limit of infinite dimension L , the quantum systems on H_L consistently recover the expectation of any bounded quantum observable on H .

Let $\beta_L : H_L \rightarrow \mathbb{C}^L$ be the linear map that maps elements of H_L to their column vector representation with respect to the $\{\phi_l\}$ basis, i.e., $\beta_L f = \mathbf{f} = (f_0, \dots, f_{L-1})^\top$ with $f_l = \langle \phi_l, f \rangle$. In applications, we represent a quantum state $\rho \in Q(H_L)$ by an $L \times L$ density matrix $\boldsymbol{\rho} = \beta_L \rho$. If $\rho = \langle \xi, \cdot \rangle \xi$ is a pure state induced by a unit vector $\xi \in H_L$, then $\boldsymbol{\rho} = \boldsymbol{\xi} \boldsymbol{\xi}^\dagger$ is a rank-1 projection matrix along the unit vector $\boldsymbol{\xi} = \beta_L \xi \in \mathbb{C}^L$, where † denotes the complex conjugate transpose.

Next, if $\rho = \Gamma(p) \in Q(H)$ is a pure state from (4.1) induced by a probability density $p \in L^1(\mu)$, i.e., $\rho = \langle \xi, \cdot \rangle \xi$ with $\xi = \sqrt{p}$, then for large-enough L we have $\rho_L = \langle \xi_L, \cdot \rangle \xi_L$ with $\xi_L = \Pi_L \xi / \|\Pi_L \xi\|_H$. It should be noted that, in general, ξ_L is not the square root of a probability density in $P(\mu)$; in fact, ξ_L need not be a positive function. Thus, analogously to our discretization of observables from subsection 4.3.1, our finite-dimensional representations of classical probability densities are through intrinsically quantum mechanical objects.

4.3.3. Discretization of evolution operators. Let $U \equiv U^1$ and $P \equiv P^1$ be the single-step Koopman and transfer operators on H . For any $L \in \mathbb{N}$, we define projected operators $U_L = \Pi_L U$ and $P_L = \Pi_L P$ on H_L , and the corresponding induced operators $\mathcal{U}_L : B(H_L) \rightarrow B(H_L)$ and $\mathcal{P}_L : B_1(H_L) \rightarrow B_1(H_L)$ as $\mathcal{U}_L A = U_L A U_L^*$ and $\mathcal{P}_L A = U_L^* A U_L \equiv P_L A P_L^*$. In general, U_L and P_L are not unitary operators. Nevertheless, \mathcal{P}_L can be shown to be trace non-increasing, $\text{tr}(\mathcal{P}_L \rho) \leq 1$ for any $\rho \in Q(H_L)$. As a result, the operator semigroups $\{\mathcal{U}_L^n\}_{n \in \mathbb{N}}$ and $\{\mathcal{P}_L^n\}_{n \in \mathbb{N}}$ generated by \mathcal{U}_L and \mathcal{P}_L , respectively, define an open quantum system on H_L . Note that if H_L is a U -invariant subspace of H , then $U_L : H_L \rightarrow H_L$ and $P_L : H_L \rightarrow H_L$ are unitary, and we can define associated unitary evolution groups $\{\mathcal{U}_L^n\}_{n \in \mathbb{N}}$ and $\{\mathcal{P}_L^n\}_{n \in \mathbb{N}}$. However, every such U -invariant subspace H_L must necessarily admit a basis of Koopman eigenfunctions, and we cannot in general assume existence of such a basis. Irrespective of whether U and P are unitary, for any number of timesteps

$n \in \mathbb{N}$, observable $A \in B(H)$, and quantum state $\rho \in Q(H)$, we have

$$\lim_{L \rightarrow \infty} \mathbb{E}_{\mathcal{P}_L^n \rho_L} A_L = \mathbb{E}_{\mathcal{P}^n \rho} A,$$

where $A_L = \Pi_L A$ and ρ_L is given by (4.8).

4.3.4. Discretization of effects. We use the projection maps Π_L to discretize effects similarly to our discretization of quantum observables from subsection 4.3.1. First, observe that since $\Pi_L A \leq A$ whenever $A \in B(H)$ is positive, the projections Π_L map effects into effects; that is, we can view Π_L as a map from $\mathcal{E}(H)$ to $\mathcal{E}(H_L)$. Using (4.9), it follows that for every observable $A \in B(H)$, state $\rho \in Q(H)$, and effect $e \in \mathcal{E}(H)$,

$$\lim_{L \rightarrow \infty} \mathbb{E}_{\rho_L | e_L} A_L = \mathbb{E}_{\rho | e} A,$$

where $A_L = \Pi_L A$, ρ_L is given by (4.8), and $e_L = \Pi_L e$. Thus, conditioning by the projected effects e_L consistently recovers conditioning by e in the infinite-dimension limit. Note that if $e \in \mathcal{E}(H)$ is “classical”, i.e., it is a multiplication operator by characteristic function of a classical event, $e = \pi \chi_S$ for some measurable set $S \subseteq \Omega$, the projected effect $e_L = \pi_L \chi_S$ is in general not a multiplication operator. Thus, in the context of the finite-dimensional quantum systems on H_L , state conditioning takes place by generally non-classical events.

4.4. Choice of basis. Recall that the family of Hilbert spaces $H_0 \subset H_1 \subset \dots$ from subsection 4.3 is determined from an orthonormal basis $\{\phi_0, \phi_1, \dots\}$ of H . In choosing this basis, one must keep in mind that in applications the invariant measure μ that defines the inner product of H is typically supported on an unknown, non-smooth subset of state space (e.g., a fractal attractor). In such cases, defining the basis vectors ϕ_l through explicit closed-form expressions is generally not possible, so we rely instead on an implicit basis construction through eigendecomposition of kernel integral operators. This approach was introduced in the diffusion forecast technique [7], and was later used in related methods for Koopman operator approximation [36, 31, 23], as well as in QMDA [32, 29]. For our purposes, an advantage of using eigenfunctions of integral operators is their approximability from training data sampled from the invariant measure μ ; we will take up this task in section 6.

Let $W : \Omega \rightarrow \mathcal{W}$ be a measurable function into a data space \mathcal{W} that we will use to build our basis. In the applications presented in sections 7 and 8 below, \mathcal{W} will be a Euclidean space, $\mathcal{W} = \mathbb{R}^{d_{\mathcal{W}}}$ for some dimension $d_{\mathcal{W}}$, and possibilities for W will include:

- The identity map Id for $\mathcal{W} = \Omega$, which corresponds to using information from the full system state to build the basis.
- The projection map $\mathcal{P}_{\mathcal{X}} : \Omega \rightarrow \mathcal{X}$ for $\mathcal{W} = \mathcal{X}$, which corresponds to building the basis using information from only the resolved variables.
- A delay-coordinate map [66] for $\mathcal{W} = \mathcal{X}^Q$, where $Q = \mathbb{N}$ is the number of delays, which corresponds to using the dynamics to implicitly recover some of the information about the full system state lost through projection onto \mathcal{X} .

For any of these choices, let $\kappa_{\mathcal{W}} : \mathcal{W} \times \mathcal{W} \rightarrow \mathbb{R}$ be a symmetric kernel function and $\kappa : \Omega \times \Omega \rightarrow \mathbb{R}$ its pullback to Ω , i.e., $\kappa(\omega, \omega') = \kappa_{\mathcal{W}}(W(\omega), W(\omega'))$. We assume that W and $\kappa_{\mathcal{W}}$ have sufficient regularity so that κ lies in $L^2(\mu \times \mu)$. In that case, the integral operator $K : H \rightarrow H$ defined as

$$(4.10) \quad Kf = \int_{\Omega} \kappa(\cdot, \omega) f(\omega) d\mu(\omega)$$

is a self-adjoint, real, Hilbert-Schmidt integral operator. As a result, there exists a real orthonormal basis $\{\phi_0, \phi_1, \dots\}$ of H consisting of eigenvectors of K ; that is,

$$(4.11) \quad K\phi_l = \lambda_l \phi_l,$$

where the eigenvalues λ_l are real and satisfy $|\lambda_0| \leq |\lambda_1| \leq \dots \searrow 0$. In the experiments of [sections 7 and 8](#) our nominal choice for $\kappa_{\mathcal{W}}$ is the radial Gaussian kernel on $\mathcal{W} = \mathbb{R}^{d_{\mathcal{W}}}$,

$$(4.12) \quad \kappa_{\mathcal{W}}(w, w') = e^{-\|w - w'\|_2^2 / \epsilon_{\mathcal{W}}^2},$$

where $\epsilon_{\mathcal{W}} > 0$ is a bandwidth parameter that we tune automatically (see [Appendix A.3.1](#)). In some of our experiments, we will use a variable-bandwidth generalization of (4.12) proposed in [9], which was also used in refs. [32, 29] in QMDA applications. We define the Hilbert spaces H_L using (4.5) with the eigenvectors ϕ_l from (4.11).

Next, note that whenever the eigenvalue λ_l is nonzero, any corresponding eigenvector ϕ_l (which is an equivalence class of functions on Ω , defined μ -a.e.) is represented by the everywhere-defined function $\varphi_l : \Omega \rightarrow \mathbb{R}$ such that

$$(4.13) \quad \varphi_l(\omega) = \frac{1}{\lambda_l} \int_{\Omega} \kappa(\omega, \omega') \phi_l(\omega') d\mu(\omega').$$

It follows from (4.13) that every such function φ_l inherits the regularity properties (e.g., boundedness, continuity, differentiability) of the kernel κ . This motivates using kernels with plentiful nonzero corresponding eigenvalues in order to control the regularity of the basis functions. More specifically, noticing that φ_l from (4.13) is the pullback of a function on \mathcal{W} , i.e., $\varphi_l = \varphi_l^{(\mathcal{W})} \circ W$ for some $\varphi_l^{(\mathcal{W})} : \mathcal{W} \rightarrow \mathbb{R}$, we obtain a “maximal” number of nonzero eigenvalues λ_l if the $\varphi_l^{(\mathcal{W})}$ form an orthonormal basis of the Hilbert space $L^2(\mu_{\mathcal{W}})$ on \mathcal{W} associated with the pushforward measure $\mu_{\mathcal{W}} := W_*\mu$. This will hold, for instance, if $\kappa_{\mathcal{W}}$ is an integrally strictly-positive-definite kernel on \mathcal{W} [69], e.g., the radial Gaussian kernel on $\mathcal{W} = \mathbb{R}^{d_{\mathcal{W}}}$ from (4.12).

5. Quantum mechanical closure (QMCI). Recall from [section 2](#) that the state space of the parameterized system has the decomposition $\tilde{\Omega} = \mathcal{X} \times \tilde{\mathcal{Y}}$, where $\tilde{\mathcal{Y}}$ is the state space of the surrogate model for the unresolved degrees of freedom, and \mathcal{X} is the space of variables we are seek to accurately predict. In QMCI, we set $\tilde{\mathcal{Y}}$ to the state space $\tilde{\mathcal{Y}} = Q(H_L)$ of the finite-dimensional quantum system constructed in [subsection 4.3](#) for some $L \in \mathbb{N}$. Thus, in order to evolve the parameterized system via (2.2), we need to specify (i) the surrogate flux term $\tilde{Z} : Q(H_L) \rightarrow \mathcal{Z}$; and (ii) the evolution map $\tilde{\psi} : \mathcal{X} \times Q(H_L) \rightarrow Q(H_L)$ of the surrogate model. These maps will be specified in [subsections 5.1 to 5.3](#). In [subsection 5.4](#), we define a map $\alpha : \Omega \rightarrow \tilde{\Omega}$ that assigns initial conditions of the parameterized system on $\tilde{\Omega}$ from initial conditions of the true system (see the commutative diagram (2.1)).

5.1. Flux term. We also assume throughout that \mathcal{Z} is a Euclidean space, $\mathcal{Z} = \mathbb{R}^d$. With that assumption, we represent the true and surrogate flux terms componentwise, i.e., $Z = (Z^{(1)}, \dots, Z^{(d)})$ and $\tilde{Z} = (\tilde{Z}^{(1)}, \dots, \tilde{Z}^{(d)})$, where $Z^{(i)} : \mathcal{Y} \rightarrow \mathbb{R}$ and $\tilde{Z}^{(i)} : Q(H_L) \rightarrow \mathbb{R}$ are real-valued functions. We also assume that for each $i \in \{1, \dots, d\}$, the pullback function $\zeta^{(i)} : \Omega \rightarrow \mathbb{R}$ with $\zeta^{(i)} = Z^{(i)} \circ P_{\mathcal{Y}}$ is essentially bounded with respect to μ , so that $\zeta^{(i)}$ is an element of the $L^\infty(\mu)$ algebra. Under that condition, $\zeta^{(i)}$ has a representation in $B(H)$ by the multiplication operator $\pi\zeta^{(i)}$,

and we have a corresponding projected operator $\pi_L \zeta^{(i)} \in B(H_L)$. We set $\tilde{Z}^{(i)}$ to the quantum mechanical expectation associated with this multiplication operator, i.e.,

$$(5.1) \quad \tilde{Z}^{(i)}(\rho) = \mathbb{E}_\rho(\pi_L \zeta^{(i)}).$$

Given that the resolved variables and the quantum state at time t_n are $x_n \in \mathcal{X}$ and $\rho_n \in B(H_L)$, respectively, we use (5.1) and the resolved dynamics $\phi : \mathcal{X} \times \mathcal{Z} \rightarrow \mathcal{X}$ to update x_n to the state x_{n+1} at time t_{n+1} via the formula

$$(5.2) \quad x_{n+1} = \phi(x_n, z_n), \quad z_n = \tilde{Z}(\rho_n).$$

This step is depicted in the top line in the schematic of Figure 1.

5.2. Quantum state update. Our approach for updating the quantum state $\rho_n \in Q(H_L)$ given the resolved variables in $x_n \in \mathcal{X}$ is inspired by the prediction-correction scheme employed in sequential data assimilation (filtering) [56, 51], which was formulated quantum mechanically in refs. [32, 29]. First, we use the projected transfer operator \mathcal{P}_L to evolve ρ_n to the quantum state

$$(5.3) \quad \tilde{\rho}_{n+1} := \frac{\mathcal{P}_L \rho_n}{\text{tr}(\mathcal{P}_L \rho_n)};$$

see the arrow labeled “transfer operator” in the bottom row of the schematic in Figure 1. The state $\tilde{\rho}_{n+1}$ plays an analogous role to the prior density in classical data assimilation. Then, we update the quantum state ρ_{n+1} at time t_{n+1} by conditioning $\tilde{\rho}_{n+1}$ by a quantum effect induced by the classical state x_{n+1} , i.e.,

$$(5.4) \quad \rho_{n+1} = \tilde{\rho}_{n+1}|_{e_{n+1}} = \frac{\sqrt{e_{n+1}} \tilde{\rho}_{n+1} \sqrt{e_{n+1}}}{\text{tr}(\sqrt{e_{n+1}} \tilde{\rho}_{n+1} \sqrt{e_{n+1}})}, \quad e_{n+1} = \mathcal{F}_L(x_{n+1}),$$

where $\mathcal{F}_L : \mathcal{X} \rightarrow \mathcal{E}(H_L)$ is an effect-valued map that will be described in subsection 5.3. This update is represented by the arrow labeled “state conditioning” in the second row of the schematic in Figure 1. The state ρ_{n+1} obtained in this manner is loosely analogous to the posterior density in classical data assimilation.

The map $\tilde{\psi} : \mathcal{X} \times Q(H_L) \rightarrow Q(H_L)$ that evolves the state of the quantum system is defined as $\tilde{\psi}(x_n, \rho_n) = \rho_{n+1}$, where ρ_{n+1} is obtained from (x_n, ρ_n) by combining (5.2), (5.3), and (5.4).

In applications, the frequency of updating the state via conditioning on a quantum effect can be varied. Instead of using the map $\tilde{\psi}$ as defined above, one may use $\tilde{\psi}_r : \mathcal{X} \times Q(H_L) \rightarrow Q(H_L)$ where (5.2) and (5.3) are iterated r times between every application of (5.4); see Algorithm A.1. This corresponds to lengthening the time under which the quantum component of the system undergoes Koopman evolution before it is updated via conditioning on the observation of an effect.

5.3. Effect-valued feature map. What remains to completely define the posterior state in (5.4) is to specify the effect-valued map $\mathcal{F}_L : \mathcal{X} \rightarrow \mathcal{E}(H_L)$. Following [29], we build this map as an operator-valued feature map induced by a measurable kernel function $k : \mathcal{X} \times \mathcal{X} \rightarrow [0, 1]$ on the resolved variables space. Every such function induces a feature map $F : \mathcal{X} \rightarrow L^\infty(\mu)$ with $\text{ran } F \subseteq L^\infty(\mu)$, given by $F(x) = k(x, \cdot)$. Composing this map with the representation $\pi : L^\infty(\mu) \rightarrow B(H)$ leads to a feature map $\mathcal{F} : \mathcal{X} \rightarrow \mathcal{E}(H)$, $\mathcal{F} = \pi \circ F$, which takes values in the effect space of the infinite-dimensional operator algebra $B(H)$. We obtain \mathcal{F}_L by projection of \mathcal{F} onto $B(H_L)$, i.e., $\mathcal{F}_L = \Pi_L \circ \mathcal{F}$.

In the applications presented in [sections 7 and 8](#), $\mathcal{X} = \mathbb{R}^{d_{\mathcal{X}}}$ is a Euclidean space, and we use a radial Gaussian kernel

$$(5.5) \quad k(x, x') = e^{-\|x - x'\|_2^2 / \epsilon^2}, \quad \epsilon > 0.$$

The radial Gaussian kernel is strictly positive-definite [\[43\]](#), which implies that the corresponding feature map F is injective.

5.4. Initialization. Assuming that the parameterized dynamics $\tilde{\Phi} : \tilde{\Omega} \rightarrow \tilde{\Omega}$ have been appropriately defined, we would ideally like to have an initialization map $\alpha : \Omega \rightarrow \tilde{\Omega}$ such that the commutative diagram [\(2.1\)](#) is satisfied. Practically, we cannot assume to have access to the unresolved variables in \mathcal{Y} , so we must contend with maps that depend on $(x, y) \in \Omega$ only through $x \in \mathcal{X}$. With that in mind, it is natural to choose α using the effect-valued feature map from [subsection 5.3](#), defining

$$(5.6) \quad \alpha(x) = (x, \rho_x), \quad \rho_x = \frac{\mathcal{F}_L(x)}{\text{tr}(\mathcal{F}_L(x))},$$

whenever $\text{tr}(\mathcal{F}_L(x)) > 0$. Note that ρ_x defined in this way is a state since $\mathcal{F}_L(x)$ is a positive operator for all $x \in \mathcal{X}$. Empirically, we find that following the decay of initial transients, the behavior of QMCI-parameterized systems does not depend significantly on the choice of ρ_x . For instance, replacing [\(5.6\)](#) by

$$(5.7) \quad \alpha(x) = (x, \bar{\rho}), \quad \bar{\rho} = \langle 1_{\Omega}, \cdot \rangle 1_{\Omega},$$

which ignores any information from x for the assignment of the initial quantum state $\bar{\rho}$, was found to impart negligible changes in the long-term statistical behavior of the parameterized system. The numerical experiments in [sections 7 and 8](#) (which focus on one- and two-point statistics under the invariant measure) utilize α from [\(5.7\)](#).

Computationally, an advantage of [\(5.7\)](#) over [\(5.6\)](#) is that the former is a pure state (whereas the latter is generally mixed), resulting in a significant reduction of computational cost (see [subsection 6.6](#)). However, it is possible that initializing with [\(5.6\)](#) (or a low-rank approximation thereof) as opposed to [\(5.7\)](#) would be beneficial in initial-value prediction experiments, which we do not address in this paper.

5.5. Stochastic parameterization. The QMCI scheme described in [subsections 5.1 to 5.3](#) is deterministic, in the sense that a given initial condition $(x_0, \rho_0) \in (\mathcal{X}, Q(H_L))$ completely determines the sequence $(x_0, \rho_0), (x_1, \rho_1), \dots$ of resolved variables x_n and quantum states ρ_n . In another approach, which we call the “stochastic” approach, we set $\tilde{\mathcal{Y}}$ to the sequence space $\tilde{\mathcal{Y}} = \mathcal{Z}^{\mathbb{N}}$. As in [subsection 2.1.2](#), we equip $\tilde{\mathcal{Y}}$ with a σ -algebra $\Sigma_{\tilde{\mathcal{Y}}}$ and a probability measure ν that is invariant under the shift map $T : \tilde{\mathcal{Y}} \rightarrow \tilde{\mathcal{Y}}$. We also let $u : \tilde{\mathcal{Y}} \rightarrow \mathbb{Z}$ be the projection map onto the first coordinate, and define the random variables $\tilde{Z}_n : \tilde{\mathcal{Y}} \rightarrow \mathcal{Z}$ such that $\tilde{Z}_n = u \circ T^n$. We formally choose the probability space $(\tilde{\mathcal{Y}}, \Sigma_{\tilde{\mathcal{Y}}}, \nu)$ such that the components $Z_n^{(1)}, \dots, Z_n^{(d)} : \tilde{\mathcal{Y}} \rightarrow \mathbb{R}$ are independent, real-valued random variables distributed according to the measure $\mathbb{P}_{\rho_n, \pi \zeta^{(j)}}$ from [\(3.2\)](#). Operationally, this means that the values $z_n = (z_n^{(1)}, \dots, z_n^{(d)}) \in \mathcal{Z}$ of the flux terms at time n are obtained by independent random draws from the measurement distributions $\mathbb{P}_{\rho_n, \pi \zeta^{(1)}}, \dots, \mathbb{P}_{\rho_n, \pi \zeta^{(d)}}$, respectively, determined via [\(4.7\)](#). The update formulas [\(5.3\)](#) and [\(5.4\)](#) for the quantum state ρ_n remain unchanged. See [Algorithm A.3](#) for pseudocode.

6. Data-driven formulation. To move towards a data-driven algorithm, we must first establish a method to generate a discrete analog of $H = L^2(\mu)$ (and then of H_L) which can be manipulated in practice. To that end, we make the following standing assumptions.

- A1. We have access to samples $w_0, \dots, w_{N-1} \in \mathcal{W}$ and $z_0, \dots, z_{N-1} \in \mathcal{Z}$ from the map W and the unresolved fluxes Z , respectively, with $w_m = W(\omega_m)$ and $z_m = Z(\omega_m)$. The samples are taken along a dynamical trajectory $\omega_0, \dots, \omega_{N-1} \in \Omega$ with $\omega_m = \Phi^m(\omega_0)$.
- A2. The invariant measure μ is ergodic.
- A3. There is a compact, forward-invariant set $\mathcal{M} \subseteq \Omega$ (i.e., $\Phi(\mathcal{M}) \subseteq \mathcal{M}$) that contains the support of μ and the starting point ω_0 (and thus the entire orbit $\omega_0, \omega_1, \dots$).
- A4. The maps Φ , X , Z , and W are continuous on \mathcal{M} . Moreover, the kernels κ and k from [subsections 4.4](#) and [5.3](#), respectively, are both continuous on $\mathcal{M} \times \mathcal{M}$.

With these assumptions, we use the samples $\{(w_m, z_m)\}_{m=0}^{N-1}$ as training data to build data-driven QMCI models that are structurally very similar to the data-independent models described in [section 5](#). Our construction follows closely the data-driven formulation of QMDA [\[32, 29\]](#). Note that we do not assume knowledge of the states ω_m underlying the training data (w_m, z_m) . Also, we do not require that the ω_m lie on the support of μ (which may be a null set with respect to an ambient measure on Ω , such as an attractor of a dissipative system), but allow instead initial conditions ω_0 drawn from the larger set \mathcal{M} of potentially positive ambient measure [\[10\]](#).

For the rest of the paper, we reserve m indices to denote samples in the training data and n indices to denote samples obtained from free-running QMCI models. For example, in our notation, x_m and x_n are independent points in \mathcal{X} , the former representing the resolved variables in the training phase, and the latter output from a QMCI model.

6.1. Finite-dimensional Hilbert space. Let μ_N be the discrete sampling measure on Ω supported on the training trajectory, defined as $\mu_N = \sum_{m=0}^{N-1} \delta_{\omega_m} / N$ where δ_{ω_m} is the Dirac δ -measure supported on $\omega_m \in \Omega$. As a finite-dimensional analog of $H = L^2(\mu)$, we employ the finite-dimensional Hilbert space $\hat{H}_N := L^2(\mu_N)$, equipped with the inner product

$$\langle f, g \rangle_N := \int_{\Omega} f^* g d\mu_N = \frac{1}{N} \sum_{m=0}^{N-1} f^*(\omega_m) g(\omega_m).$$

Note that the elements of \hat{H}_N are equivalence classes of functions on Ω with common values at the sampled states ω_m . Assuming, for simplicity of exposition, that the points $\omega_0, \dots, \omega_{N-1}$ are all distinct (which holds true aside from special cases such as ω_0 being an eventually periodic point under Φ), \hat{H}_N has dimension N . Thus, every element $f \in \hat{H}_N$ can be represented by a column vector $\mathbf{f} = (f_0, \dots, f_{N-1})^\top \in \mathbb{C}^N$ with components $f_m = f(\omega_m)$, and every column vector $\mathbf{f} \in \mathbb{C}^N$ represents a unique element $f \in \hat{H}_N$. Correspondingly, every linear map $A : \hat{H}_N \rightarrow \hat{H}_N$ can be represented by a matrix $\mathbf{A} \in \mathbb{C}^{N \times N}$ such that $\mathbf{A}\mathbf{f}$ is the column vector representation of Af .

Let $C(\mathcal{M})$ denote the Banach space of continuous, complex-valued functions on \mathcal{M} , equipped with the uniform norm, $\|f\|_{C(\mathcal{M})} = \max_{\omega \in \mathcal{M}} |f(\omega)|$. Under [Assumptions A2](#) and [A3](#), for μ -a.e. initial condition $\omega_0 \in \mathcal{M}$ and in the limit of large data,

$N \rightarrow \infty$, the measures μ_N converge to the invariant measure in the weak-* topology of finite Borel measures on \mathcal{M} ; i.e.,

$$(6.1) \quad \lim_{N \rightarrow \infty} \int_{\mathcal{M}} f d\mu_N \equiv \lim_{N \rightarrow \infty} \frac{1}{N} \sum_{m=0}^{N-1} f(\omega_m) = \int_{\mathcal{M}} f d\mu, \quad \forall f \in C(\mathcal{M}).$$

In (6.1), we may replace f in the integrals with respect to μ_N by a uniformly convergent sequence of functions f_N ; that is, we have

$$(6.2) \quad \lim_{N \rightarrow \infty} \int_{\mathcal{M}} f_N d\mu_N = \int_{\mathcal{M}} f d\mu,$$

for μ -a.e. $\omega_0 \in \mathcal{M}$, where $\lim_{N \rightarrow \infty} f_N = f$ in $C(\mathcal{M})$ norm. In what follows, (6.2) will play a key role in ensuring the consistency of the data-driven formulation of QMCI.

6.2. Data-driven basis. In subsection 4.4, we used the eigenfunctions ϕ_l of the kernel integral operator $K : H \rightarrow H$ to define L -dimensional subspaces $H_L \subseteq H$ (see (4.5)) on which we built finite-dimensional quantum systems. To do this in the data-driven setting, we replace K with the operator $K_N : \hat{H}_N \rightarrow \hat{H}_N$ defined analogously to (4.10) as

$$K_N f = \int_{\Omega} \kappa(\cdot, \omega) f(\omega) d\mu_N(\omega) = \frac{1}{N} \sum_{m=0}^{N-1} \kappa(\cdot, \omega_m) f(\omega_m).$$

Computationally, K_N is represented by the $N \times N$ kernel matrix

$$\mathbf{K}_N = [\kappa(\omega_i, \omega_j)]_{i,j=0}^{N-1} = [\kappa_{\mathcal{W}}(w_i, w_j)]_{i,j=0}^{N-1}.$$

Once again, we solve the eigenvalue problem for K_N ,

$$(6.3) \quad K_N \phi_{l,N} = \lambda_{l,N} \phi_{l,N},$$

and define L -dimensional subspaces $H_{L,N} \subseteq \hat{H}_N$ as (cf. (4.5))

$$(6.4) \quad H_{L,N} = \text{span}\{\phi_{0,N}, \dots, \phi_{L-1,N}\}.$$

In (6.4), the eigenvectors $\phi_{l,N}$ are orthonormal on \hat{H}_N , and the corresponding eigenvalues $\lambda_{l,N}$ are real and are ordered in order of decreasing modulus. Analogously to $\Pi_L : H \rightarrow H$ and $\mathbf{\Pi}_L : B(H) \rightarrow B(H)$ from subsection 4.3, we define projection maps $\Pi_{L,N} : \hat{H}_N \rightarrow \hat{H}_N$ and $\mathbf{\Pi}_{L,N} : B(\hat{H}_N) \rightarrow B(\hat{H}_N)$ such that $\text{ran } \Pi_L = H_L$ and $\mathbf{\Pi}_{L,N} A = \Pi_{L,N} A \Pi_{L,N}$. We also let $\beta_{L,N} : H_{L,N} \rightarrow \mathbb{C}^L$ and $\beta_{L,N} : B(H_{L,N}) \rightarrow \mathbb{M}_L$ be the maps from vectors in $H_{L,N}$ and operators in $B(H_{L,N})$ to their corresponding vector and matrix representations with respect to the $\{\phi_{l,N}\}_{l=0}^{L-1}$ basis, defined analogously to $\beta_L : H_L \rightarrow \mathbb{C}^L$ and $\beta_L : B(H_L) \rightarrow \mathbb{M}_L$ from subsection 4.3, respectively.

Similarly to the representatives φ_l of ϕ_l from (4.13), every eigenvector $\phi_{l,N}$ with nonzero corresponding eigenvalue $\lambda_{l,N}$ has an everywhere-defined representative $\varphi_l : \Omega \rightarrow \mathbb{R}$, given by

$$(6.5) \quad \varphi_{l,N}(\omega) = \frac{1}{\lambda_{l,N}} \int_{\mathcal{M}} \kappa(\omega, \omega') \phi_{l,N}(\omega') d\mu_N = \frac{1}{\lambda_{l,N}} \frac{1}{N} \sum_{m=0}^{N-1} \kappa(\omega, \omega_m) \phi_{l,N}(\omega_m).$$

Under Assumption A4, every such φ_l and $\varphi_{l,N}$ is continuous on \mathcal{M} . By results on spectral approximation of kernel integral operators [72], the following can be shown to hold as $N \rightarrow \infty$, for μ -a.e. initial condition $\omega_0 \in \mathcal{M}$:

1. For every nonzero eigenvalue λ_l of K , the sequence of eigenvalues $\lambda_{l,N}$ of K_N converges to λ_l , including multiplicities.
2. For every continuous representative $\varphi_l \in C(\mathcal{M})$ of an eigenfunction $\phi_l \in H$ of K corresponding to $\lambda_l \neq 0$, there exists a sequence of eigenfunctions $\phi_{l,N} \in \hat{H}_N$ of K_N whose continuous representatives $\varphi_{l,N} \in C(\mathcal{M})$ converge to φ_l in the $C(\mathcal{M})$ norm.

We refer the reader to the paper [29] for further details on these results in the context of QMDA.

6.3. Operator approximation. We use the data-driven basis $\{\phi_{l,N}\}_{l=0}^{N-1}$ of $H_{L,N}$ to consistently approximate matrix representations of operators on H_L by matrix representations of operators on $H_{L,N}$ for a class of operators that behave consistently with operators on continuous functions. In what follows, $\iota : C(\mathcal{M}) \rightarrow L^p(\mu)$ and $\iota_N : C(\mathcal{M}) \rightarrow L^p(\mu_N)$ will denote the standard maps from continuous functions on \mathcal{M} to their corresponding L^p equivalence classes with respect to μ and μ_N , respectively.

Consider an operator $A \in B(H)$ that satisfies

$$(6.6) \quad A \circ \iota = \iota \circ \tilde{A}$$

for some bounded operator $\tilde{A} : C(\mathcal{M}) \rightarrow C(\mathcal{M})$. Consider also a uniformly bounded sequence of operators $\hat{A}_1, \hat{A}_2, \dots$ in $B(\hat{H}_1), B(\hat{H}_2), \dots$, respectively, such that

$$(6.7) \quad \lim_{N \rightarrow \infty} \|(\hat{A}_N \circ \iota_N - \iota_N \circ \tilde{A})f\|_{\hat{H}_N} = 0, \quad \forall f \in C(\mathcal{M}).$$

Given any such operator family $\{A, \tilde{A}, \hat{A}_0, \hat{A}_1, \dots\}$, our approach is to approximate matrix elements of A with respect to the kernel eigenbasis $\{\phi_l\}$ of H from [subsection 4.4](#) by matrix elements of \hat{A}_N with respect to the data-driven eigenbasis $\{\phi_{l,N}\}$ of \hat{H}_N . Specifically, let ϕ_i and ϕ_j be two basis vectors of H from (4.11) corresponding to nonzero eigenvalues. Let $\phi_{i,N}$ and $\phi_{j,N}$ be basis vectors of \hat{H}_N from (6.3) chosen such that, as $N \rightarrow \infty$, their continuous representatives $\varphi_{i,N}$ and $\varphi_{j,N}$ converge to those of ϕ_i and ϕ_j (i.e., φ_i and φ_j), respectively, as described in [subsection 6.2](#). Then, it can be shown [29] that for μ -a.e. $\omega_0 \in \mathcal{M}$,

$$(6.8) \quad \lim_{N \rightarrow \infty} \langle \phi_{i,N}, \hat{A}_N \phi_{j,N} \rangle_N = \langle \phi_i, A \phi_j \rangle.$$

This means that we can consistently approximate matrix elements of A by matrix elements of \hat{A}_N . In particular, if $L \in \mathbb{N}$ is such that λ_{L-1} is nonzero, it follows from (6.8) that as $N \rightarrow \infty$ the matrix representations $\mathbf{A}_{L,N} = \beta_{L,N} \hat{A}_{L,N}$ of the projected operators $A_{L,N} = \Pi_{L,N} \hat{A}_N \in B(H_{L,N})$ converge to the matrix representation $\mathbf{A}_L = \beta_L A_L$ of $A_L = \Pi_L A$ in any matrix norm. As we explain in [subsection 6.4](#) and [Appendix A.1](#), under [Assumption A4](#), all operators employed in QMCI satisfy the compatibility conditions (6.6) and (6.7) and thus can be approximated in this manner.

6.4. Data-driven QMCI framework. In the data-driven setting, the state space of the quantum mechanical model of the unresolved variables is $\tilde{\mathcal{Y}} = Q(H_{L,N})$. Analogously to the data-independent formulation in [section 5](#), we evolve the parameterized system on $\mathcal{X} \times \tilde{\mathcal{Y}}$ using a surrogate flux $\tilde{Z} : Q(H_{L,N}) \rightarrow \mathcal{Z}$ and an evolution map $\tilde{\psi} : \mathcal{X} \rightarrow Q(H_{L,N}) \rightarrow Q(H_{L,N})$. In this subsection, we give an outline of the construction of these maps, focusing on the differences between the data-driven approach and the formulation of [section 5](#). Specific formulas and pseudocode relevant to the data-driven setting are included in [Appendix A.1](#).

Flux terms. As in [subsection 5.1](#), we prescribe the surrogate flux $\tilde{Z} : Q(H_{L,N}) \rightarrow \mathcal{Z}$ using quantum mechanical expectations of discrete multiplication operators. For that, we first note that the space $L^\infty(\mu_N)$ is a finite-dimensional, abelian von Neumann algebra, which we use as a data-driven analog of $L^\infty(\mu)$ (see [subsection 4.2.1](#)). This algebra has a regular representation $\hat{\pi}_N : L^\infty(\mu_N) \rightarrow B(\hat{H}_N)$ that maps each vector $f \in \hat{H}_N$ to the discrete multiplication operator that multiplies by f . Note that $\hat{\pi}_N f$ is a diagonal operator in the standard basis of \hat{H}_N . We use $\hat{\pi}_N$ and the projected representation $\pi_{L,N} := \mathbf{\Pi}_{L,N} \circ \hat{\pi}_N$ as data-driven analogs of $\pi : L^\infty(\mu) \rightarrow B(H)$ and $\pi_L : L^\infty(\mu) \rightarrow B(H_L)$, respectively. The training samples $z_m \in \mathcal{Z} \equiv \mathbb{R}^d$ define, componentwise, a collection of elements $\zeta_N^{(1)}, \dots, \zeta_N^{(d)} \in L^\infty(\mu_N)$ such that $\zeta_N^{(i)}(\omega_m) = z_m^{(i)}$ where $z_m^{(i)}$ is the i -th component of $z_m = (z_m^{(1)}, \dots, z_m^{(d)})$. Analogously to (5.1), we define $\tilde{Z} = (\tilde{Z}^{(1)}, \dots, \tilde{Z}^{(d)})$ with $\tilde{Z}^{(i)}(\rho) = \mathbb{E}_\rho(\pi_{L,N} \zeta_N^{(i)})$. The evolution of the resolved variables in \mathcal{X} given $\rho \in Q(H_{L,N})$ is carried out via (5.2). Computationally, the quantum observables $\tilde{Z}^{(i)}$ and states ρ are represented by their $L \times L$ matrix representations in the $\{\phi_{l,N}\}$ basis of $H_{L,N}$, i.e., $\mathbf{Z}_{L,N}^{(i)} = \beta_{L,N} \tilde{Z}^{(i)}$ and $\boldsymbol{\rho} = \beta_{L,N} \rho$.

Quantum state update. We employ a predictor–corrector scheme similar to that in [subsection 5.2](#). Given the quantum state $\rho_n \in Q(H_{L,N})$ and resolved variables $x_n \in \mathcal{X}$ at time t_n , we use a data-driven approximation $\mathcal{P}_{L,N} : B_1(H_{L,N}) \rightarrow B_1(H_{L,N})$ of the transfer operator to obtain the prior state $\tilde{\rho}_{n+1}$ at time t_{n+1} analogously to (5.3) and an effect-valued feature map $\tilde{\mathcal{F}}_{L,N} : \mathcal{X} \rightarrow \mathcal{E}(H_{L,N})$ that updates $\tilde{\rho}_{n+1}$ by conditioning by $e_{n+1} = \tilde{\mathcal{F}}_{L,N}(x_{n+1})$ as in (5.4). The transfer operator $\mathcal{P}_{L,N}$ is based on an approximation of the Koopman operator $U : H \rightarrow H$ by a shift operator $\hat{U}_N : \hat{H}_N \rightarrow \hat{H}_N$ [7]. That is, we have $\mathcal{P}_{L,N} A = U_{L,N}^* A U_{L,N}$ where $U_{L,N} = \mathbf{\Pi}_{L,N} \hat{U}_N$, and $U_{L,N}$ is represented by the $L \times L$ matrix $\mathbf{U}_{L,N} = \beta_{L,N} U_{L,N}$; see [Appendix A.1.4](#) for further details. The effect-valued feature map $\mathcal{F}_{L,N}$ is constructed analogously to \mathcal{F}_L from [subsection 5.3](#) using the radial Gaussian kernel in (5.5). In the $\{\phi_{l,N}\}$ basis of $H_{L,N}$, the map $\tilde{\mathcal{F}}_{L,N}$ is represented by a matrix-valued map $\tilde{\mathbf{F}}_{L,N} : \mathcal{X} \rightarrow \mathbb{M}_L$ with $\tilde{\mathbf{F}}_{L,N} = \beta_{L,N} \circ \mathcal{F}_{L,N}$ that we use in numerical applications; see [Appendix A.1.5](#).

Initialization. In the experiments presented in [sections 7](#) and [8](#), we initialize the parameterized system with an uninformative quantum state analogously to (5.7). Specifically, given any $x \in \mathcal{X}$, we set the initial state $\alpha(x) = (x, \bar{\rho}_{N,L}) \in \mathcal{X} \times Q(H_{L,N})$, where

$$(6.9) \quad \bar{\rho}_{N,L} = \frac{\mathbf{\Pi}_{L,N} \bar{\rho}_N}{\text{tr}(\mathbf{\Pi}_{L,N} \bar{\rho}_N)}, \quad \bar{\rho}_N = \langle 1_\Omega, \cdot \rangle_N 1_\Omega.$$

An alternative approach would be to set $\alpha(x) = (x, \rho_x)$, where the quantum state ρ_x is obtained via the effect-valued feature map $\mathcal{F}_{L,N}$ analogously to (5.6). As mentioned in [subsection 5.4](#), numerically we found that the uninformative initialization approach has negligible impact on the ability of the parameterized system to reproduce the equilibrium statistical behavior of the original system, but initializing with (5.6) is expected to be important in initial-value prediction experiments.

Stochastic parameterization. The data-driven QMCI framework has a stochastic variant which is entirely analogous to the scheme described in [subsection 5.5](#).

6.5. Convergence of data-driven approximation. With the addition of another approximation parameter (N in addition to L), we seek to examine the convergence properties of the system under the iterated limits of $L \rightarrow \infty$ after $N \rightarrow \infty$. Previous work [29] has shown that for quantum observables $\hat{A}_N \in B(\hat{H}_N)$ and $A \in B(H)$ satisfying (6.6) and (6.7) for some $\hat{A} : C(\mathcal{M}) \rightarrow C(\mathcal{M})$ and for states $\hat{\rho}_N \in Q(\hat{H}_N)$ and

$\rho \in Q(H)$ satisfying a related compatibility condition with operators on continuous functions, the following asymptotic consistency relationship holds,

$$(6.10) \quad \lim_{L \rightarrow \infty} \lim_{N \rightarrow \infty} \mathbb{E}_{\mathcal{P}_{L,N} \rho_{L,N}} A_{L,N} = \lim_{L \rightarrow \infty} \mathbb{E}_{\mathcal{P}_L \rho_L} A_L = \mathbb{E}_\rho A.$$

Here, $A_{L,N} = \Pi_{L,N} \hat{A}_N$ and $A_L = \Pi_L A$ are the projected quantum observables associated with \hat{A}_N and A , respectively, and $\rho_{L,N} \in Q(H_{L,N})$ and $\rho_L \in Q(H_L)$ are the projected states associated with $\hat{\rho}_N$ and $\hat{\rho}$, respectively (see (4.8)). Under [Assumption A4](#), the fluxes $\zeta^{(i)}$ are continuous, which implies that (6.6) and (6.7) are satisfied with $A = \pi(\iota \zeta^{(i)})$, $\hat{A}_N = \hat{\pi}_N(\iota_N \zeta^{(i)})$, and \hat{A} set to the multiplication operator by $\zeta^{(i)}$ on continuous functions. Furthermore, the class of states ρ for which (6.10) holds includes images $\rho = \Gamma(p)$ from (4.1) of probability densities in $L^1(p)$ with continuous representatives in $C(\mathcal{M})$, as well as higher-rank generalizations, so the data-driven QMCI formulation is asymptotically consistent as $N \rightarrow \infty$ in a broad range of scenarios encountered in applications. In addition, an analogous convergence result holds for conditioning by effects $e \in \mathcal{E}(H)$ and $\hat{e}_N \in \mathcal{E}(\hat{H}_N)$ which satisfy (6.6) and (6.7) for some operator $\tilde{e} : C(\mathcal{M}) \rightarrow C(\mathcal{M})$ on continuous functions. We refer the reader to [29] for further details.

6.6. Computational cost. The training data requirements and computational cost of QMCI are generally comparable with those of kernel methods for supervised machine learning. Given that the data space \mathcal{W} has dimension $d_{\mathcal{W}}$, the brute-force computation cost of forming the $N \times N$ kernel matrix \mathbf{K}_N representing the integral operator K_N is $O(d_{\mathcal{W}} N^2)$ for radial kernels. This cost can be reduced to $O(N \log N)$ in data spaces of sufficiently low dimension using randomized methods for approximate nearest neighbors, e.g., [46]. In our numerical experiments, we compute \mathbf{K}_N with brute force and then sparsify it, retaining $k_{\text{nn}} \ll N$ nearest neighbors per data point. The storage cost and matrix–vector multiplication cost for \mathbf{K}_N then become $O(k_{\text{nn}} N)$. We compute the basis vectors $\phi_{l,N}$ using iterative solvers. The cost of this computation depends on the spectral properties of \mathbf{K}_N and the number L of requested eigenvectors, but generally scales linearly k_{nn} and N . Once the basis $\{\phi_{l,N}\}_{l=0}^{L-1}$ has been computed, we form the $L \times L$ matrix $\mathbf{U}_{L,N} = \pi_{L,N} \hat{U}_N$ representing the projected shift operator and the $L \times L$ observable matrices $\mathbf{Z}_{L,N}^{(1)}, \dots, \mathbf{Z}_{L,N}^{(d)}$ (see [Appendix A.3.1](#)), each with an $O(NL^2)$ computational cost. This completes the training phase of QMCI.

The computational cost associated with advancing the parameterized model over one timestep, given that the classical and quantum states are $x_n \in \mathcal{X}$ and $\rho_n \in Q(H_{L,N})$, respectively, is as follows:

- We compute the flux terms $\tilde{Z}^{(i)}(\rho_n) = \text{tr}(\rho_n \mathbf{Z}_{L,N}^{(i)})$ for $i \in \{1, \dots, d\}$, where $\rho_n \in \mathbb{M}_L$ is the matrix representation of ρ_n in the $\{\phi_{l,N}\}$ basis of $H_{L,N}$. For a quantum state of rank r , the cost of each of these computations is $O(rL^2)$. This can be as high as $O(L^3)$ for quantum states of full rank, but in our experiments we work with pure states, $r = 1$, which results in $O(L^2)$ operations.
- We advance the resolved variables x_n via (5.2) using the previously computed fluxes. The cost of this procedure is independent of QMCI so we do not consider it further here.
- Using the transfer operator, we advance ρ_n to the density matrix $\tilde{\rho}_{n+1}$ representing the prior state $\tilde{\rho}_n$. This is again an $O(rL^2)$ operation which can be as high as $O(L^3)$ but reduces to $O(L^2)$ for pure states.

- We compute the $L \times L$ matrix $\mathbf{F}_{L,N}(x_{n+1})$ representing the quantum effect $\mathcal{F}_{L,N}(x_{n+1})$. This has an $O(d_{\mathcal{X}}NL^2)$ cost. Using $\mathbf{F}_{L,N}(x_{n+1})$ we condition $\tilde{\rho}_{n+1}$ to obtain the density matrix ρ_{n+1} representing the posterior state from (5.4). The cost of this operation is $O(rL^2)$, where r is again the rank of $\tilde{\rho}_{n+1}$.

Note that the density matrix update, $\tilde{\rho}_{n+1} \mapsto \rho_{n+1}$, is the only step in the online prediction phase whose cost depends on the size N of the training data. In [subsection 9.3](#), we discuss possible ways of alleviating this dependence using random feature methods for kernel matrix approximation [63].

7. Quantum mechanical closure of the L63 system. As our first set of numerical examples, we apply QMCI to the L63 system [54]. The L63 system is classically defined as the dynamical system on \mathbb{R}^3 where $(x(t), y(t), z(t)) \in \mathbb{R}^3$ evolves as

$$\dot{x}(t) = \sigma(y(t) - x(t)), \quad \dot{y}(t) = x(t)(\rho - z(t)) - y(t), \quad \dot{z}(t) = x(t)y(t) - \beta z(t)$$

for the parameter values $\beta = 8/3$, $\rho = 28$, and $\sigma = 10$. However, as noted in [61], the L63 system can be expressed in terms of the system (2.4), where the variables $(a_1(t), a_2(t), a_3(t)) \in \Omega \equiv \mathbb{R}^3$ are obtained by projection of $(x(t), y(t), z(t))$ onto the EOF basis vectors, and have decreasing variance.

7.1. Experimental setup. We follow closely the setup of Palmer [61], which we outlined in [subsection 2.1.2](#). We assume knowledge of the equations governing the a_1 and a_2 components, but not of that governing the a_3 component. That is, we have $(a_1, a_2) \in \mathcal{X} \equiv \mathbb{R}^2$, $a_3 \in \mathcal{Y} \equiv \mathbb{R}$, and the flux term is $Z : \mathcal{Y} \rightarrow \mathcal{Z} \equiv \mathbb{R}$ with $Z(a_3) = a_3$. The true discrete-time system on Ω evolves under the time- Δt flow generated by (2.4) for a timestep of $\Delta t = 0.01$; that is, we have $\Phi : \Omega \rightarrow \Omega$ with $\Phi = \Phi^{0.01}$. Of course, Φ is not available in closed form, so practically we consider as the “true” L63 dynamics a numerical approximation of Φ by a high-fidelity ordinary differential equation solver. Here, we use MATLAB’s `ode45` solver which is based on an adaptive Runge-Kutta scheme of order (4, 5). As our approximate resolved dynamics $\hat{\phi} : \mathcal{X} \times \mathcal{Z} \rightarrow \mathcal{Z}$ we use a standard 4th-order Runge-Kutta (RK4) discretization of the a_1 and a_2 equations in (2.4), treating a_3 as fixed; see (A.13) for an explicit formula. We evolve the quantum states in $\tilde{\mathcal{Y}} = Q(H_{L,N})$ using the map $\psi_r : \mathcal{X} \times Q(H_{L,N}) \rightarrow Q(H_{L,N})$ from [subsection 5.2](#) for various choices of the number of timesteps r between state updates by the quantum Bayes’ rule (5.4).

7.2. Experiments with large, full training data. We first consider QMCI models trained with a long time series of the full system state. In these experiments, the training observation map $W : \Omega \rightarrow \mathcal{W}$ is the identity map on $\mathcal{W} = \Omega = \mathbb{R}^3$, and we use a training time series $\omega_0, \dots, \omega_{N-1} \in \mathcal{W}$ consisting of $N = 150,000$ samples with $\omega_m = (x_m, y_m) = \Phi^m(\omega_0)$. The initial training state ω_0 is obtained by integrating (2.4) with the initial condition (2, 2, 2) for 500 model time units (i.e., $500/\Delta t = 50,000$ timesteps), and setting ω_0 to the final point of that trajectory. We also use the values $z_0, \dots, z_{N-1} \in \mathbb{R}$ of the flux term, $z_m = Z(y_m) = y_m$, from the training trajectory.

Setting the dimension parameter $L = 1500$, we compute the kernel eigenfunction basis $\{\phi_{l,N}\}_{l=0}^{L-1}$ of $H_{L,N}$ from (6.3) using the training data ω_m . The kernel function $\kappa_{\mathcal{W}}$ is the radial Gaussian kernel (4.12) with the bandwidth parameter $\epsilon_{\mathcal{W}} = \sqrt{19}$ chosen via automatic tuning (see [Appendix A.3.1](#)). We then compute the corresponding $L \times L$ matrix representations $\mathbf{U}_{L,N}$ and $\mathbf{Z}_{L,N}$ of the projected Koopman operator

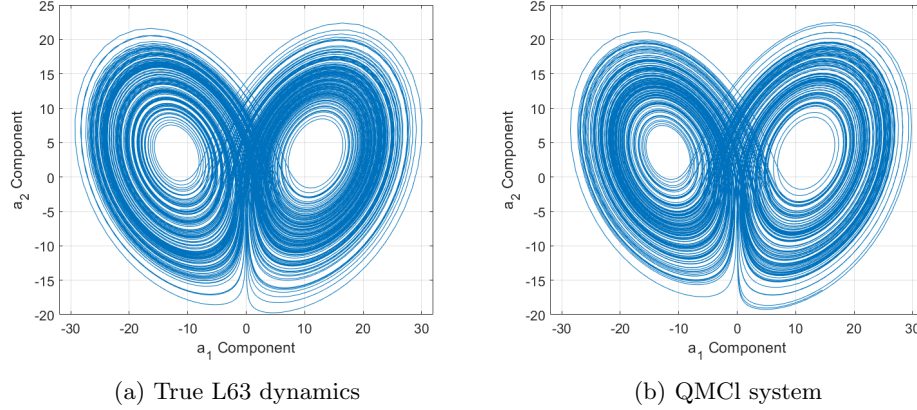


Fig. 2: Trajectory plots of the resolved variables $x = (a_1, a_2)$ under (a) the true L63 dynamics and (b) the QMCI parameterized system. The length of the plotted trajectories is 200 model time units.

and the projected multiplication operator representing the flux term Z as described in [subsection 6.4](#). We also use the basis functions to build the effect-valued feature map $\tilde{\mathbf{F}}_{L,N}$ described in [Appendix A.1.5](#). This map is based on the radial Gaussian kernel k in (5.5) with the bandwidth parameter $\epsilon = 2$. This completes the training phase of QMCI.

To run the parameterized system, we generate a state $\hat{\omega}_0 \in \Omega$ near the Lorenz attractor analogously to ω_0 ; that is, we integrate (2.4) over 500 model time units with the initial condition $(1.99, 2, 2)$, and set $\hat{\omega}_0 = (\hat{x}_0, \hat{y}_0)$ to the last point of that trajectory. We then use the initialization map (5.7) to generate an initial condition $\iota(\hat{x}_0) = (\hat{x}_0, \hat{\rho}_0) \in \mathcal{X} \times Q(H_{L,N})$ of the parameterized system. We condition the quantum state via the $\tilde{\mathcal{F}}_{L,N}$ effect map every $r = 10$ timesteps (i.e., every $r \Delta t = 0.1$ model time units).

Starting from $(\hat{x}_0, \hat{\rho}_0)$, the QMCI system generates via [Algorithm A.3.3](#) a time-ordered sequence of pairs $(\hat{x}_0, \hat{\rho}_0), (\hat{x}_1, \hat{\rho}_1), \dots$ of resolved variables $\hat{x}_n \in \mathcal{X}_n$ and quantum states $\hat{\rho}_n \in Q(H_{L,N})$, as well as a corresponding sequence of flux terms $\hat{z}_0, \hat{z}_1, \dots \in \mathcal{Z}$ given by $\hat{z}_n = \tilde{Z}(\rho_n)$ in accordance with (5.1). Under a “perfect” closure in the sense of the commutative diagram (2.1), the sequence of resolved variables $\hat{x}_0, \hat{x}_1, \dots$ should match the time series $\tilde{x}_0, \tilde{x}_1, \dots$ of the (a_1, a_2) state vector components under the L63 flow starting from the same initial condition, i.e., $\tilde{x}_n = (a_1(t_n), a_2(t_n))$ with $(a_1(t_n), a_2(t_n), a_3(t_n)) = \Phi^{n \Delta t}(\hat{\omega}_0)$. If, in addition, the flux term $Z = a_3$ is consistently approximated by \tilde{Z} , then the time series $(\hat{x}_0, \hat{z}_0), (\hat{x}_1, \hat{z}_1), \dots$ generated by the QMCI system should match the full three-dimensional L63 trajectory $\tilde{\omega}_0, \tilde{\omega}_1, \dots$ with $\tilde{\omega}_n = (a_1(t_n), a_2(t_n), a_3(t_n))$. Here, we assess the performance of the scheme by examining its ability to reproduce salient qualitative features of the Lorenz attractor and to recover the marginal distributions and time-autocorrelation functions of a_1 , a_2 , and a_3 .

[Figure 2](#) compares representative trajectories of the resolved variables x under the true L63 dynamics ([Figure 2a](#)) and their approximations \hat{x}_n under the QMCI system ([Figure 2b](#)). It is readily apparent that the QMCI system generates a structure with

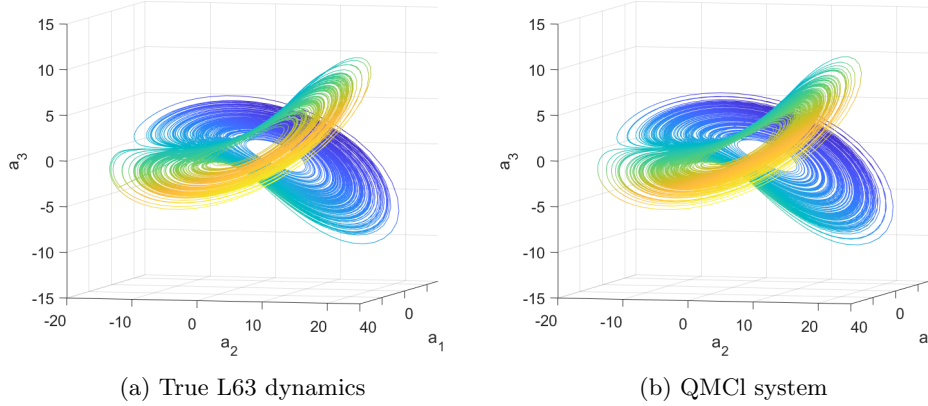


Fig. 3: As in Figure 2, but for trajectories of (a_1, a_2, a_3) in \mathbb{R}^3 showing both the resolved components, $x = (a_1, a_2)$, and the unresolved component, $y = a_3$, of the L63 state vector. The plotted trajectories spans 200 model time units. Colors correspond to the value of the a_1 component, for visual clarity.

a similar geometry to the Lorenz attractor. It is also worth noting that this similarity holds not just in the a_1, a_2 projection (which would be sufficient for a parameterization scheme). In fact, as shown by the three-dimensional trajectory plots in Figure 3, the QMCI algorithm meaningfully reconstructs all three dimensions of the system. Particularly, the trajectories show that the QMCI system evolves in the a_3 component in a qualitatively similar manner to the true system. In Figure 4, we show time series plots for the a_1 component under the true L63 and QMCI dynamics. The general rate and aperiodicity of the transitions, as well as the tendency for the point to sometimes oscillate in one lobe with increasing amplitude prior to switching lobes, are preserved in the QMCI system.

Next, in Figure 5, we examine the ability of QMCI to reproduce some of the one- and two-point statistics under the invariant measure of the L63 system, namely the marginal probability density functions (PDFs) and time-autocorrelation functions of the a_1 , a_2 , and a_3 coordinates. We estimate these statistics numerically using trajectories generated by the two systems spanning 1000 model time units (i.e., $1000/\Delta t = 100,000$ samples); see Appendix A.4 for further details. It is evident from the results that the QMCI system performs well in terms of reproducing the marginal PDF and time-autocorrelation structure of a_1 , a_2 , and a_3 with respect to the invariant measure.

Of particular importance in the L63 system is the behavior of the a_1 component. Much of the system's chaotic behavior can be understood as chaos in when the system transitions from one lobe of the attractor to another, manifesting as sign changes of the a_1 coordinate (see, e.g., Figure 2a). The autocorrelation plots in Figure 5b show that the QMCI system accurately captures the initial correlation decay of a_1 due to these transitions, which takes place over a timescale comparable to the Lyapunov timescale of the system (approximately 1 model time unit). The corresponding PDF is also reproduced reasonably well (see Figure 5a), though some differences from the true PDF are visible near $a_1 = 0$. These differences are not too surprising given that

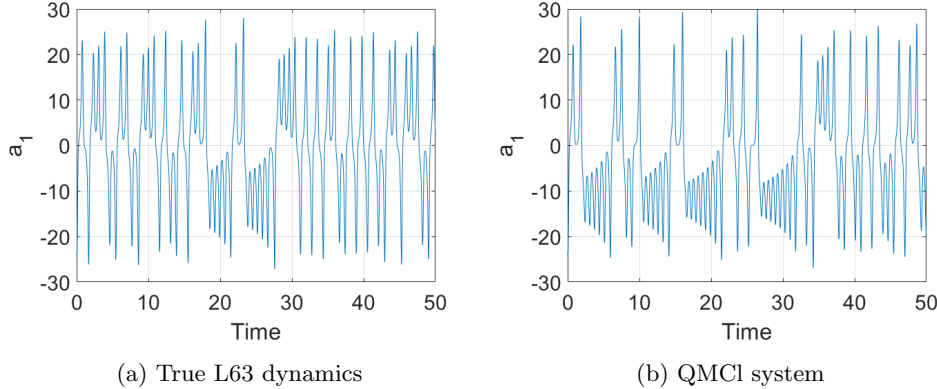


Fig. 4: Time series plots of the a_1 component under (a) the true L63 system and (b) the QMCI parameterized system.

values of a_1 close to 0 correspond to the mixing region between the two lobes of the attractor where the dynamics is particularly sensitive to perturbations.

Other notable aspects of the results in Figure 5 are the oscillatory nature of the autocorrelation function for a_2 (Figure 5d) and the bimodal corresponding PDF (Figure 5c) due to oscillations about the unstable fixed points in the center of the two “holes” of the attractor. The QMCI system is seen to consistently reproduce these features. Meanwhile, the time-autocorrelation of a_3 (Figure 5f) exhibits a damped oscillatory behavior that is again reasonably well reproduced by QMCI.

In calculations not reported here, we observed that replacing the RK4 scheme in the definition of $\tilde{\phi}$ by a first-order forward Euler scheme results in a noticeable reduction of statistical accuracy of the QMCI model in terms of the PDFs and autocorrelation functions of a_1 , a_2 , and a_3 . This effect is independent of QMCI since integrating the L63 system (2.4) with a forward Euler scheme of fixed timestep $\Delta t = 0.01$ (as opposed to `ode45`) was found to impart similar changes to the a_1, a_2, a_3 statistics.

In summary, the results presented in this subsection demonstrate that the QMCI-parameterized system provides an accurate surrogate model of the full L63 dynamics.

7.3. Small, partial training data. The experiment in subsection 7.2 assumed access to a large training dataset containing full information about the system state. Here, we show that with the same parameters but much less training data, $N = 10,000$, the QMCI method still performs a reasonable reconstruction of the L63 dynamics. On this experiment, we also impose the constraint that in generating the kernel eigenvectors defining $H_{L,N}$ we do not have access to full state vectors (a_1, a_2, a_3) . Instead, only the a_1 component is available.

Let $\tilde{W} : \Omega \rightarrow \mathbb{R}$ be the map that projects onto the first coordinate, i.e., $\tilde{W}(\omega) = a_1$ with $\omega = (a_1, a_2, a_3)$. Let also $\tilde{w}_m = \tilde{W}(\omega_m)$, where $\omega_0, \omega_1, \dots, \omega_{N-1} \in \Omega$ is the training trajectory in state space (defined as in subsection 7.2, but assumed here unobserved). To enrich the data \tilde{w}_m with information lost due to projection by \tilde{W} , delay-coordinate embedding is used on this one-dimensional time series. Setting $\mathcal{W} = \mathbb{R}^Q$, where $Q \in \mathbb{N}$ is an even parameter corresponding to the number of delays,

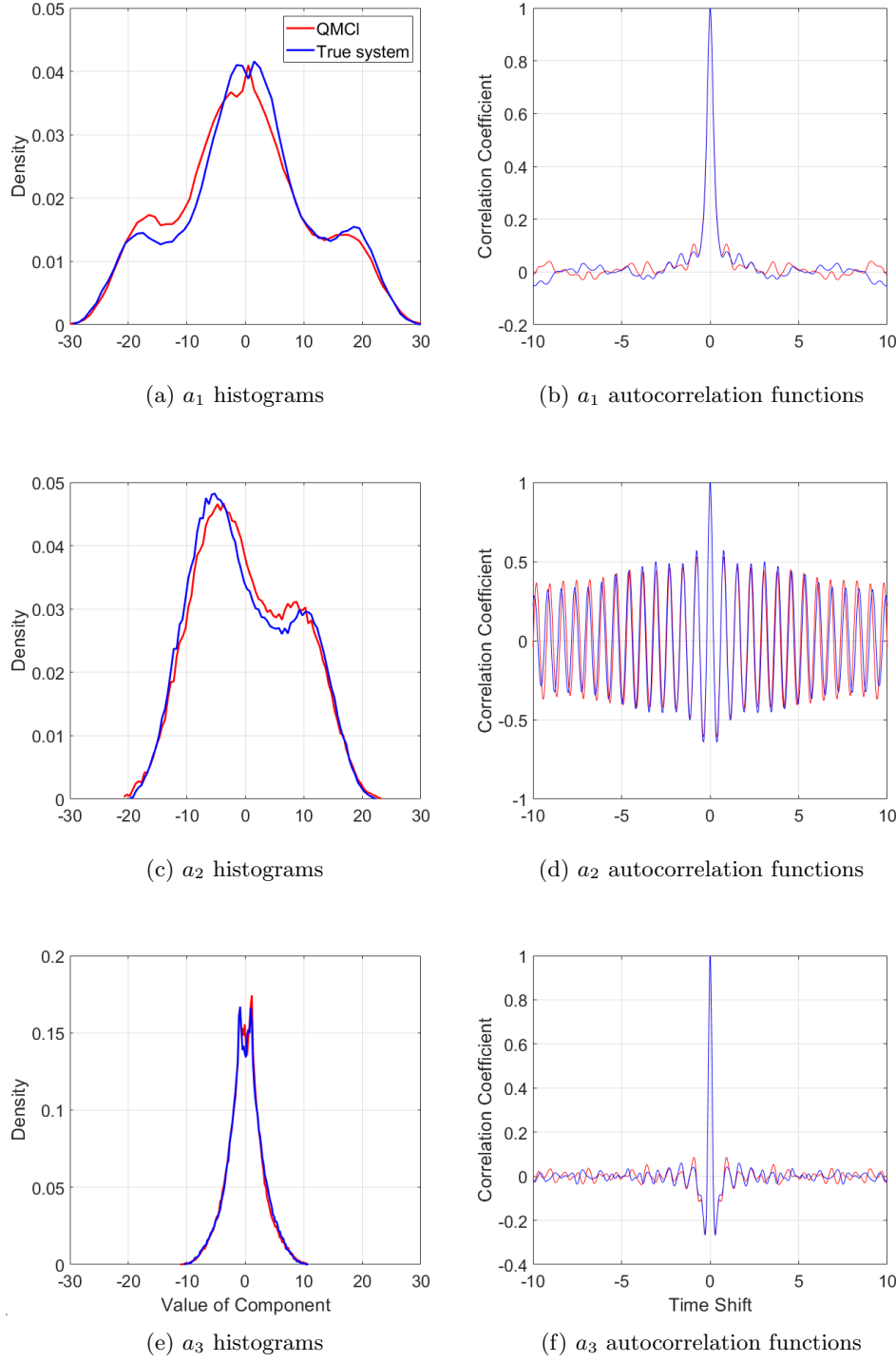


Fig. 5: Empirical PDFs (a, c, e) and normalized time-autocorrelation functions (b, d, f) of the a_1 (a, b), a_2 (c, d), and a_3 (e, f) components of the L63 system under the true and QMCI dynamics. The PDFs and autocorrelation functions were estimated using time series spanning 1000 model time units.

we define the delay-coordinate map $W : \Omega \rightarrow \mathcal{W}$ such that

$$(7.1) \quad W(\omega) = (\tilde{W}(\Phi^{-Q/2}(\omega)), \tilde{W}(\Phi^{-Q/2+1}(\omega)), \dots, \tilde{W}(\Phi^{Q/2}(\omega))).$$

From the theory of delay-coordinate maps [66] it is known that for sufficiently large Q , and with “high probability” in a suitable sense, W is an injective map on compact subsets of Ω , and thus the support of the invariant measure μ (which is compact since it is contained in an absorbing ball under the L63 dynamics [50]). Thus, for sufficiently large Q , training data obtained through the map W should be theoretically sufficient to build a basis for the entire Hilbert space H . Importantly for practical applications, we have

$$W(\omega_m) = (\tilde{w}_{m-Q/2}, \tilde{w}_{m-Q/2+1}, \dots, \tilde{w}_{m+Q/2}),$$

which means that we can evaluate W on the dynamical states ω_m underlying the training data without knowledge of these states. In particular, we can compute kernel matrices and build an associated data-driven basis of $H_{L,N}$ as described in [subsection 6.2](#) using data sampled from W . It is worthwhile noting that as the number of delays Q increases, the kernel eigenfunctions obtained from delay-coordinate-mapped data tend to span approximately Koopman-invariant subspaces [22, 33], which improves the quality of Koopman/transfer operator approximation in these subspaces. This fact motivates using delay-coordinate maps even when full system states are available for training.

[Figure 6](#) displays representative trajectory, marginal PDF, and autocorrelation results obtained using $N = 10,000$ training samples from (7.1) and $Q = 10$ delays. For the kernel $\kappa_{\mathcal{W}}$ used to build the basis we used the variable-bandwidth kernel proposed in [9], normalized to a symmetric Markov kernel using the approach of [19]. A description of the construction of this kernel can be found in [29]. For the feature-map kernel k , a bandwidth value $\epsilon = 10$ was chosen. One can notice that this system still closely approximates both the marginal PDFs ([Figure 6c](#)) and autocorrelation functions ([Figure 6d](#)) of the true system under the invariant measure. However, in both cases, it is evident that the larger, more informative training data used in the experiment of [subsection 7.2](#) allows for a more accurate approximation of the true system; see, e.g., the autocorrelation plots in [Figure 6d](#).

7.4. Stochastic closure experiments. For purposes of establishing a baseline of performance based on a concise and fast stochastic method, we first examine plots generated by the i.i.d. Gaussian closure of [61] (see [subsection 2.1.2](#)). [Figure 7](#) shows representative trajectories for the (a_1, a_2) and (a_1, a_2, a_3) components generated by this system. Though both attractor lobes are visible, there is noticeably less accuracy in the behavior when it comes to transitions between lobes—this is reflected in the autocorrelation plots shown in [Figure 8d](#). The stochastic closure also fails to reproduce the characteristic “holes” around the fixed points in the lobes of the attractor. This is reflected in the a_1 PDF from the Gaussian closure in [Figure 8c](#) which exhibits high probability density for values of a_1 that have lower probability density under the true system due to the holes.

Viewing [Figure 7b](#) allows us a glimpse into what is going on “under the hood” of the stochastic Gaussian closure. Since the choice of the a_3 component is Gaussian i.i.d. for each timestep, the a_3 component appears simply as random noise, while the useful approximation of the attractor manifests only in the (a_1, a_2) projection (see [Figure 7a](#)). On the other hand, in [Figure 3b](#) we can see that the deterministic QMCI approach reconstructs the entire attractor, even including the parameterized dimension. In

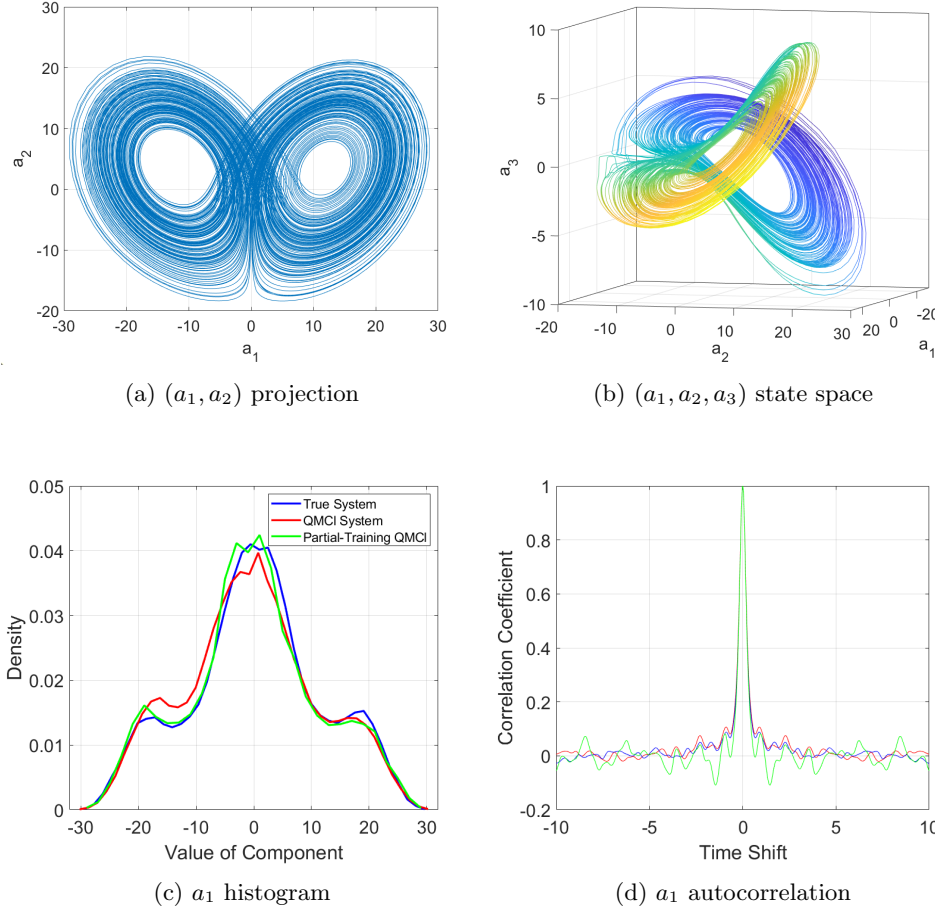


Fig. 6: Trajectories (a, b), marginal PDF of a_1 (c), and normalized time-autocorrelation function of a_1 (d) for the L63 QMCI system generated from 10,000 training points. The basis functions for this QMCI system were generated only from the a_1 L63 component of the training data, using delay-coordinate embedding. The trajectories in (a, b) span 200 model time units. The PDFs and autocorrelation functions for the partial-training system in (c, d) were estimated using time series spanning 200 model time units. PDFs and autocorrelation functions from the true L63 system and QMCI system from Figures 5a and 5b are shown for reference.

some applications such as climate dynamics, the increase in computation cost and requisite information in QMCI (see subsection 6.6) may result in parameterizations based on cheaper parametric stochastic models such as the i.i.d. Gaussian closure of the L63 system being favorable. However, the ability to accurately reconstruct entire attractors may allow for the reproduction of more complicated and subtle dynamical properties in the resolved variables, which could in turn have value in areas where additional computation time would be worth investing.

In comparison with the deterministic QMCI and i.i.d. Gaussian closure, we also

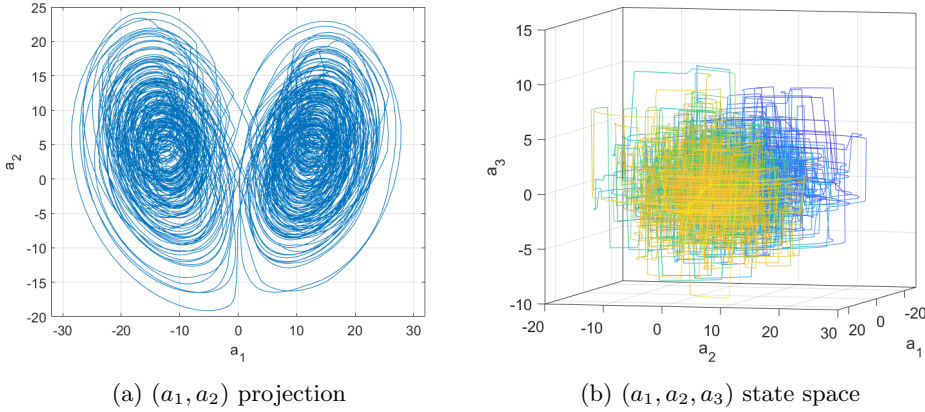


Fig. 7: Projected (a) and three-dimensional (b) trajectories generated by the Gaussian parameterization of the L63 system from [subsection 2.1.2](#). The plotted trajectories span 200 model time units. In (b), the color corresponds to the value of the a_1 component. Notice the lack of structure in the a_3 coordinate compared to [Figure 3a](#) due to modeling of the a_3 dynamics as an i.i.d. Gaussian process.

examine the stochastic QMCI closure described in [subsection 5.5](#). In this experiment, we use $N = 90,000$ samples of the state vector (i.e., $W = \text{Id}$ as in [subsection 7.2](#)) and $L = 1200$ eigenfunctions to build the QMCI Hilbert space $H_{L,N}$. The quantum state was updated through the observation kernel after every ten timesteps (i.e., $r = 10$). The bandwidth parameter for the kernel $\kappa_{\mathcal{W}}$ used to build the basis was algorithmically chosen to be $\epsilon_{\mathcal{W}} = \sqrt{19}$, and the bandwidth parameter for the feature map kernel k was chosen to be $\epsilon = 35$.

It is worth noting that a relatively large value of ϵ was chosen for this experiment (cf. $\epsilon = 2$ and $\epsilon = 10$ in [subsections 7.2](#) and [7.3](#), respectively) due to numerical stability issues. Namely, for values of ϵ comparable to the deterministic QMCI experiments, the stochastic QMCI system tends to run into numerical errors associated with the effect-update step if the current point lands too far from the training data (meaning that, for some $\hat{x}_n \in \mathcal{X}$ under the parameterized dynamics, $k(\hat{x}_n, x_m)$ is numerically zero for all x_m in the training dataset). Increasing ϵ makes the system more stable with respect to this particular problem, at the expense of a less informative kernel. The deterministic QMCI system is less noisy, and as it appears inherently less likely to run into this issue, allowing for the value of ϵ to be chosen significantly smaller.

In [Figures 8c](#) and [8d](#), we compare the marginal PDF and time-autocorrelation function of the a_1 variable, respectively, of the true system, the deterministic and stochastic QMCI systems, and the i.i.d. Gaussian closure. We can notice that the stochastic QMCI closure comes closer to reconstructing the correct PDF and autocorrelation function than the i.i.d. Gaussian closure. As is clear from [Figure 8a](#), the stochastic QMCI algorithm recovers some qualitative aspects of the L63 system, but fails in other important respects. In [Figure 8b](#) we can see that the three-dimensional (a_1, a_2, a_3) trajectories are somewhat more coherent than their counterparts from the Gaussian closure in [Figure 7b](#) (since the stochastic flux terms in QMCI are not i.i.d., and their distribution depends on the resolved variables), but they are still dominated

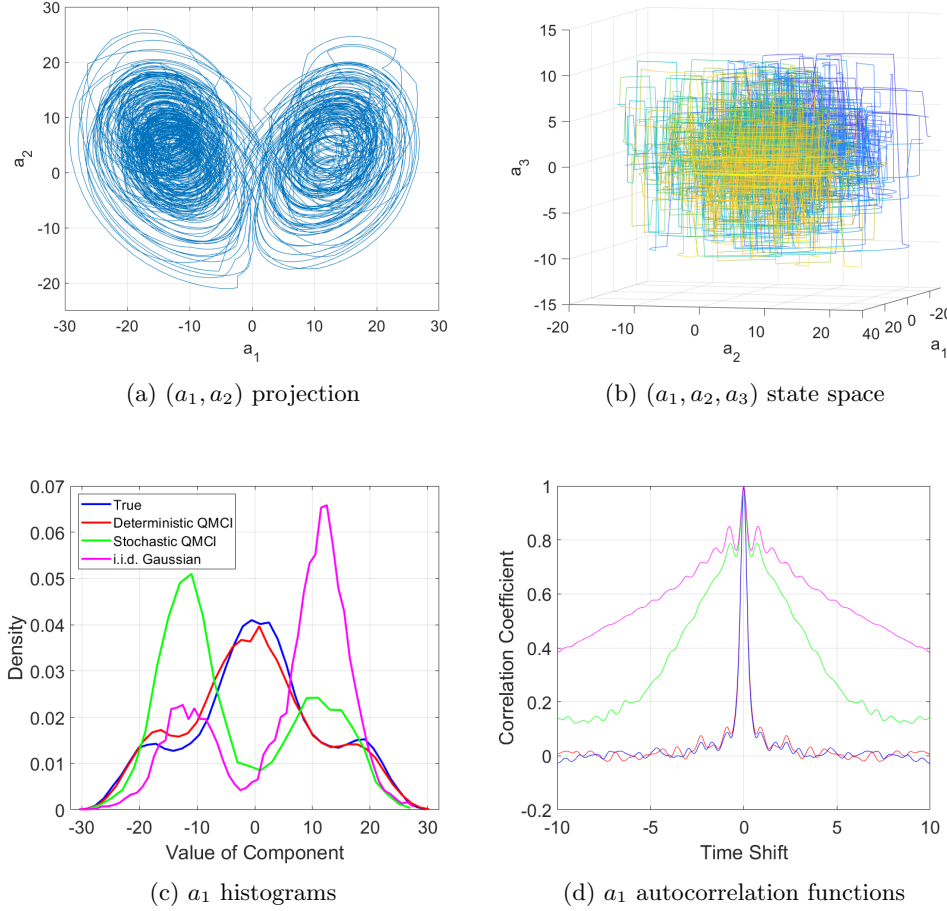


Fig. 8: Trajectories (a, b), marginal PDF of a_1 (c), and time-autocorrelation of a_1 (d) for the stochastic QMCI closure of the L63 system. The trajectories in (a, b) span 200 model time units. The PDFs and autocorrelation functions for the stochastic QMCI system in (c, d) were estimated using time series spanning 200 time units. PDFs and autocorrelation functions from the true L63 system, the deterministic QMCI system from Figures 5a and 5b, and the i.i.d. Gaussian closure [61] (see Figure 7 for trajectories) are also shown.

by noise. Moreover, similarly to the Gaussian closure, the “holes” of the attractor lobes (Figure 8a) are not adequately recovered. In Figure 8c, we notice that the a_1 histograms have significantly different structures—namely, the trajectories generated from the stochastic QMCI system tend to cluster in the two lobes, while the true system has a high density of points in the central transition region. Evidently, while the “double wing” nature of the attractor is present in the stochastic QMCI system, the smoothness of the transition between lobes, the general distribution of points, and the rate and qualitative behavior of the system as it transitions are all less accurate to the true system than the deterministic QMCI system is.

8. Lorenz 96 multiscale. The L96 multiscale model [55, 27] is a system of equations of K variables $\{x_k\}_{k=1}^K$ and JK variables $\{y_{j,k}\}_{j,k=1}^{J,K}$ defined by

$$(8.1) \quad \begin{aligned} \dot{x}_k &= -x_{k-1}(x_{k-2} - x_{k+1}) - x_k + F - h_x \bar{y}_k, \\ \dot{y}_{j,k} &= \frac{1}{\varepsilon} (-y_{j+1,k}(y_{j+2,k} - y_{j-1,k}) - y_{j,k} + h_y x_k), \\ x_{k+K} &= x_k, \quad y_{j,k+K} = y_{j,k}, \quad y_{j+J,k} = y_{j,k+1}, \end{aligned}$$

where $\bar{y}_k = \sum_j y_{j,k}/J$, and F, h_x, h_y , and ε are real parameters. The L96 multiscale system is a more comprehensive model of atmospheric dynamics than the L63 system. For $\varepsilon \ll 1$, it is a multiscale system, in which the variables x_k vary slowly in time and each have an associated set $\{y_{j,k}\}_{j=1}^J$ of variables which vary quickly. Each slow variable x_k is only influenced by the fast variables via the average value \bar{y}_k of its associated fast variable set. The L96 multiscale system has been extensively used as a testbed for parameterization schemes; see, e.g., [73, 21, 2, 45, 16, 38] among many references. The objective of parameterization in this case is to approximate the behavior of the slow variables. That is, we have $x = (x_1, \dots, x_K) \in \mathcal{X} \equiv \mathbb{R}^K$, $y = (y_{1,1}, \dots, y_{J,K}) \in \mathcal{Y} \equiv \mathbb{R}^{JK}$, and $Z : \mathcal{Y} \rightarrow \mathcal{Z} \equiv \mathbb{R}^K$ with $Z(y) = (\bar{y}_1, \dots, \bar{y}_K)$ for the resolved variables, unresolved variables, and flux terms, respectively.

As $\varepsilon \rightarrow 0$, the L96 multiscale system is known to exhibit an averaging limit [62], in which the evolution of the x_k variables is Markovian and is governed by the system of equations

$$\dot{x}_k = -x_{k-1}(x_{k-2} - x_{k+1}) - x_k + h_x \hat{Z}_k(x),$$

for some functions $\hat{Z}_1, \dots, \hat{Z}_K : \mathcal{X} \rightarrow \mathbb{R}$. Following refs. [14, 29], we choose the parameters $K = 9$, $J = 8$, $h_x = -0.8$, $h_y = 1$, and $\varepsilon = 1/128$. The resulting dynamical regime is chaotic, with approximately Markovian dynamics for the x_k variables.

8.1. Quantum mechanical closure experiments. Let $\Phi^t : \Omega \rightarrow \Omega$ with $\Omega = \mathcal{X} \times \mathcal{Y}$ and $t \in \mathbb{R}$ be the flow generated by (8.1). Similarly to the L63 experiments in section 7, we consider a discrete-time system $\Phi : \Omega \rightarrow \Omega$ with $\Phi = \Phi^{\Delta t}$ obtained by temporal subsampling of the flow. Here, the timestep is $\Delta t = 0.01$ model time units. As training data for QMCI, we use time series $w_0, \dots, w_{N-1} \in \mathcal{W} \equiv \mathcal{X} \equiv \mathbb{R}^K$ and $z_0, \dots, z_{N-1} \in \mathcal{Z}$, where $w_m = \mathcal{P}_{\mathcal{X}}(\omega_m)$, $z_m = Z(\omega_m)$, and $\omega_0, \dots, \omega_{N-1} \in \Omega$ with $\omega_m = \Phi^m(\omega_0)$. In particular, we build the basis of $H_{L,N}$ using information from only the slow variables. The numerical trajectory ω_m is generated using MATLAB's `ode15s` solver which is appropriate for stiff problems. The number of training samples is $N = 40,000$, and the initial condition ω_0 is taken on the trajectory starting from $(x_1, \dots, x_K) = (1, 0, \dots, 0)$ and $(y_{1,1}, \dots, y_{J,K}) = (1.1, 0, \dots, 0)$ after an equilibration time interval of 200 model time units (i.e., similarly to the L63 experiments; see subsection 7.2).

We build the kernel eigenbasis of the Hilbert space $H_{L,N}$ with dimension $L = 1900$ using the radial Gaussian kernel $\kappa_{\mathcal{W}}$ from (4.12). As in the L63 experiments from section 7, the bandwidth parameter $\epsilon_{\mathcal{W}} = \sqrt{10}$ was tuned automatically. Moreover, the evolution map $\phi : \mathcal{X} \times \mathcal{Z} \rightarrow \mathcal{X}$ is based on the RK4 scheme in (A.13). We evolve the quantum states using the map $\psi_r : \mathcal{X} \times Q(H_{L,N}) \rightarrow Q(H_{L,N})$ with $r = 5$ Koopman evolution steps (i.e., $r \Delta t = 0.05$ model time units) between each state conditioning via (5.4). The effect-valued feature-map $\mathcal{F}_{L,N}$ was based on a radial Gaussian kernel, here with bandwidth parameter $\epsilon = 2$. Similarly to the L63 experiments, we assess the performance of QMCI in terms of its ability to reproduce salient qualitative features of the true dynamics, as well as marginal PDFs and time-autocorrelation functions of

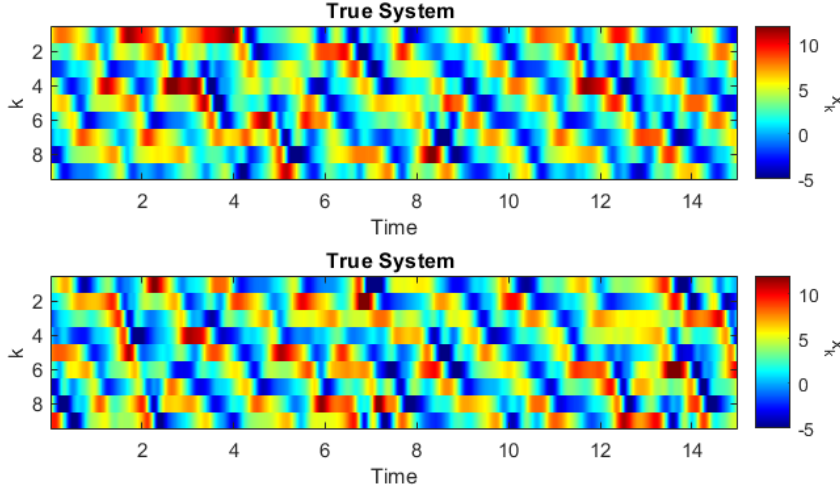


Fig. 9: Hovmoller diagrams of the slow variables x_k for the true L96 multiscale system (top) and the QMCI-parameterized system (bottom).

the revolved variables. In these tests, the true and QMCI systems are initialized on the trajectory starting from $(x_1, \dots, x_K) = (1, 0, \dots, 0)$ and $(y_{1,1}, \dots, y_{J,K}) = (1, 0, \dots, 0)$ after an equilibration period of 1000 model time units. We use 100,000 samples (i.e., $100,000 \Delta t = 1000$ model time units) on the true and QMCI trajectories starting at that point to compute PDFs and autocorrelation functions. The initial QMCI state is obtained via (5.7).

Figure 9 displays Hovmoller diagrams (space-time heat maps) of the x_k variables under the true L96 and QMCI dynamics. In our chosen dynamical regime, the x_k variables exhibit characteristic propagating patterns which can be thought of as crude representations of eastward-propagating disturbances in the Earth's midlatitude atmosphere. The dynamics of these wave-like structures, including their aperiodic emergence and decay, appear to be qualitatively well-captured by the QMCI system.

As a more quantitative test, in Figure 10 we compare the marginal PDFs and time-autocorrelation functions of x_1 under the true L96 and QMCI dynamics. We can see in Figure 10b that the autocorrelation under the QMCI system matches the periodicity present in that of the true system, though the decay of the correlation amplitude is somewhat faster in the QMCI system. The x_1 PDFs (Figure 10a) are also in good agreement between the true and QMCI systems.

9. Summary and discussion. We have developed a data-driven framework for closure of dynamical systems that combines aspects of quantum theory, ergodic theory, and kernel methods for machine learning. Our approach, called Quantum Mechanical Closure (QMCI), models the unresolved degrees of freedom as a finite-dimensional quantum mechanical system that is coupled to a classical model governing the resolved variables. The state of the quantum system is a density operator (a quantum mechanical analog of a probability density) that evolves dynamically under the induced action of the Koopman operator. The fluxes from the unresolved variables to the resolved variables are modeled as expectations of quantum observables (self-adjoint operators) that provide the closure terms needed to advance the resolved

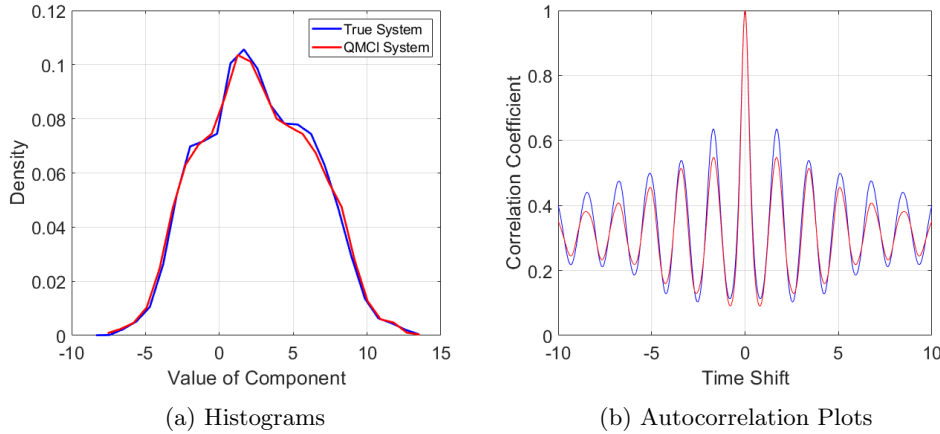


Fig. 10: Marginal PDFs (a) and time-autocorrelation functions (b) of the x_1 component of the L96 multiscale system under the true and QMCI dynamics, estimated using time series spanning 1000 model time units.

variables given the current quantum state. Meanwhile, the state of the resolved variables updates the quantum state by conditioning, using an operator-valued feature map in a step that can be viewed as a quantum mechanical analog of Bayes' rule. The resulting two-way coupling between the classical and quantum systems for the resolved and unresolved degrees of freedom, respectively, resembles the prediction–correction cycle of sequential data assimilation (filtering).

QMCI has a data-driven implementation in which a dataset of N samples of the resolved variables is used to learn a basis for an L -dimensional Hilbert space $H_{L,N}$ consisting of eigenfunctions $\phi_{l,N}$ of a kernel integral operator. The quantum mechanical closure model is then built over $H_{L,N}$, and all operators employed in the scheme are numerically represented as $L \times L$ matrices with respect to the $\{\phi_{l,N}\}$ basis. The data-drive formulation of QMCI has a well-characterized large-data limit, $N \rightarrow \infty$, leveraging results from spectral approximation of kernel integral operators. In addition the method has a stochastic variant wherein the closure terms are obtained by random draws at each timestep from the probability distribution of quantum mechanical measurements induced by the quantum state.

We have applied QMCI to deterministic and stochastic closure experiments involving the L63 (section 7) and L96 multiscale (section 8) systems; the latter, in a chaotic regime with timescale separation. In these experiments, QMCI was able to reconstruct the qualitative nature of the resolved variables, as well as their marginal distribution and time-autocorrelation functions with respect to the invariant measure. In the L63 examples, the unresolved variable was also recovered, resulting in a three-dimensional reconstruction of the Lorenz attractor.

We end the paper with a discussion of some of the salient features of QMCI and possible avenues for future work.

9.1. Positivity preservation. A novel aspect of QMCI is that it casts the problem of closure of dynamical systems in the setting of operator algebras and the associated quantum probability theory. What we have argued in this paper is that

the structure of these spaces naturally leads to computational algorithms with improved structure-preservation properties compared to formulations in abelian algebras of classical observables. In particular, as a result of basic properties of projections on operator algebras, QMCI represents positive classical observables by positive operators, whereas orthogonal projections onto finite-dimensional function spaces, are not, in general, positivity preserving. By virtue of the same properties, QMCI is able to represent classical probability densities by “honest-to-god” density operators in finite dimensions, whereas finite orthogonal basis expansions of probability densities are not, in general, positive functions (and thus not normalizable to probability densities).

We believe that the positivity preservation enjoyed by QMCI is a useful property in applications. In geophysical fluid dynamics, for instance, many relevant physical quantities such as density, moisture, and pressure, by definition take non-negative values. Since negative values of such variables have no physical meaning, a parameterization scheme which generates negative-valued outputs of these observables could have particularly problematic effects on the system as a whole. Core conservation laws, regarding mass, for example, could be violated by such a negative quantity, leading to poor, or even meaningless, predictions as time advances. In the context of parameterizations of climate models, some of the biases and numerical instabilities exhibited by data-driven parameterization schemes have indeed been attributed to failure to respect physical constraints such as energy conservation and positivity of precipitation [75], and it is possible that QMCI may provide a route to addressing such issues.

9.2. Stochastic versus deterministic approaches. In areas such as climate modeling, stochastic parameterization as a general approach has been increasingly studied and used to successful ends [6]. The stochastic mode of the QMCI framework (subsection 5.5) can be thought of as a new stochastic parameterization algorithm. In this view, at each time, the probability distribution associated with the stochastically-drawn flux term z is determined by a generalized probability density function which is the quantum density operator ρ . Though the framework of QMCI fundamentally alters the mathematical structure underlying the probabilistic dynamics of the distribution, as a whole this can nonetheless can be thought of in the same general terms as stochastic parameterizations based on classical probability theory.

The deterministic approach (subsections 5.1 to 5.4), instead of drawing the value of z randomly from an induced probability measure, directly chooses z to be the expectation value of a quantum observable given the quantum state ρ . This is a natural choice as an estimator of the true flux given the unresolved variables, and is similar in spirit to statistical closure methods that estimate fluxes through classical expectations [45], including methods based on ensemble data assimilation [16, 38, 17, 52]. We argue that the deterministic mode of QMCI is better thought about in a fundamentally different way than the stochastic mode (that is, differently than as some extension or limiting case of the stochastic approach).

Upon first glance, one might imagine that dropping stochasticity counteracts the primary benefit of this method as an approach compared to more standard approaches to parameterization. Indeed, moving away from deterministic functions of the state as parameterizations, due to their inherent dynamics-flattening properties, is one reason why we were interested in such techniques to begin with. However, while the choice of z at a given time is deterministic in this mode, it is not a function of the classical state at a given time—it is a function of the quantum state. That is, instead of our deterministic parameterization function being a function on the space of unresolved

variables \mathcal{Y} , it is now a function on the space of $L \times L$ density matrices. The latter, is a convex subset of the set of $L \times L$ Hermitian matrices of (real) dimension $L^2 - 1$ [5]. Assuming that the initial state is pure (i.e., a rank-1 projection, as is the case in the experiments in sections 7 and 8), all subsequent states produced by the QMCI algorithm are pure, and thus lie in a subset of the set of all quantum states of dimension $2(L-1)$. Since L can be very large compared to the dimension of \mathcal{Y} , our parameterization is no longer a dimension reduction, but in fact a massive dimension expansion. These additional dimensions allow for much more information to be carried through time, and allow us to avoid the dynamics-flattening that comes from a reduction approach.

A number of benefits arise from the deterministic variant of QMCI. For one, it is significantly computationally cheaper than the stochastic version, since the step of generating a probability distribution and drawing points from it is replaced by the comparatively cheaper calculation of computing $\text{tr}(\rho(\pi_L \zeta^{(i)}))$ from (5.1) (particularly when ρ is a pure state, in which case the computational cost is $O(L)$). Furthermore, in systems such as L96 multiscale (section 8), where multiple draws need to be taken at each timestep, we have a simple solution to the problem of choosing how to correlate the approximations of the various unresolved components. In the stochastic setup, all parameters were drawn separately (from the same quantum state, but nonetheless independently). Potentially important relations between what the values of the various parameters could be at a given time were thus lost—regardless of the accuracy of the PDFs, individual variation could result in sets of parameters which could not actually exist in reality. In the deterministic approach, this problem is implicitly resolved. All flux terms are taken to be the expectation of their observable $\pi_L \zeta^{(i)}$ associated with a given quantum state, so there is an implicit correlation between the parameters which naturally arises from the quantum state itself. Finally, it is not unreasonable to think that analyzing convergence properties and error bounds of the deterministic approach may be easier in future research than a stochastic mode.

In the L63 results of subsection 7.4, we can already see clear benefits of using the expectation value over a random draw. What is manifest in the trajectory plots in Figure 3, along with the marginal PDF and time-autocorrelation plots in Figure 5, is that the quantum state appears to be carrying sufficient information to resolve the a_3 component at each time in a way that meaningfully corresponds to the underlying dynamics. To achieve this, however, we had to use the expectation value.

9.3. Future work. This work motivates future research in a number of directions. First, it would be fruitful to explore ways of improving the computational scalability of QMCI, both with regards to training and out-of-sample evaluation. To that end, methods for kernel approximation based on random features [63] appear well-suited to reduce the computational cost of the current brute-force kernel computations, which is $O(N^2)$ for training (basis function computation) and $O(N)$ for out-of-sample evaluation (operator-valued feature map). Random feature methods can reduce these costs to $O(N)$ and $O(1)$, respectively, while allowing streaming data processing in the training phase [34]. Another direction would be to employ methods for kernel learning [60] so as to optimize the kernels used in the computation of the basis and operator-valued feature map with respect to an objective. A longer-term goal would be to develop implementations of QMCI on quantum computers. Recent approaches for simulation of dynamical systems on quantum computers based on closely-related mathematical techniques to QMCI have shown promising results for simple ergodic dynamical systems [35], and it would be interesting to explore whether these methods can be extended in a parameterization context. Here, a challenge

would be how to handle sequential two-way interactions between the classical and quantum computational systems representing the resolved and unresolved dynamics, respectively. We believe that addressing this and other related problems would be fruitful areas for future work.

Appendix A. Numerical methods. This appendix contains details on the numerical implementation of the data-driven formulation of QMCI described in [section 6](#). [Appendix A.1](#) provides details on the linear operators employed in the data-driven scheme. [Appendix A.2](#) gives the formula for classical evolution of the resolved variables used in the experiments of [sections 7](#) and [8](#). [Appendix A.3](#) contains a high-level algorithmic description of the QMCI pipeline, along with associated pseudocode. [Appendix A.4](#) describes the approach used to compute histograms and time-autocorrelation functions.

A.1. Linear operators. In [Appendices A.1.1](#) to [A.1.5](#), we describe the construction of the kernel integral operators, multiplication operators, spectral measures, evolution operators, and effect-valued feature maps, respectively, used in the data-driven QMCI formulation. We assume throughout availability of the training data described in [section 6](#). For simplicity, we suppress N and L subscripts (number of training samples and eigenfunctions, respectively) from our notation of column vectors and matrices representing vectors and linear operators, respectively.

A.1.1. Kernel integral operators. The first step in the data-driven QMCI algorithm is to use the training data $w_0, \dots, w_{N-1} \in \mathcal{W}$ to build the kernel integral operator $K_N : \hat{H}_N \rightarrow \hat{H}_N$ and compute the associated eigenfunctions $\phi_{l,N}$. The eigenvalue problem for K_N in [\(6.3\)](#) is equivalent to the matrix eigenvalue problem

$$(A.1) \quad \mathbf{K} \phi_l = \lambda_{l,N} \phi_l$$

for the $N \times N$ kernel matrix $\mathbf{K} = [K_{ij}]_{i,j=0}^{N-1}$ with $K_{ij} = \kappa_{\mathcal{W}}(w_i, w_j)$, where $\phi_l = (\phi_{0l}, \dots, \phi_{N-1,l})^\top \in \mathbb{R}^N$ are column vectors whose elements give the eigenfunction values, $\phi_{ml} = \phi_{l,N}(\omega_m)$. We normalize the eigenvectors such that $\phi_i^\top \phi_j = N \delta_{ij}$, which is equivalent to the orthonormality condition $\langle \phi_{i,N}, \phi_{j,N} \rangle_N = \delta_{ij}$ on \hat{H}_N . For computation, it is useful to arrange the leading L eigenvectors $\phi_0, \dots, \phi_{L-1}$ that form the basis of $H_{L,N}$ in an $N \times L$ matrix Φ whose l -th column is equal to ϕ_l .

A.1.2. Multiplication operators. Every classical observable $f : \Omega \rightarrow \mathbb{C}$ induces an element $\hat{f}_N \in L^\infty(\mu_N)$ by restriction to the finite dynamical trajectory $\{\omega_0, \dots, \omega_{N-1}\} \subset \Omega$ underlying the training data. Since $L^\infty(\mu_N)$ is isomorphic to \mathbb{C}^N whenever the states ω_m are distinct (which we assume here), we can represent \hat{f}_N by the column vector $\mathbf{f} = (f_0, \dots, f_{N-1})^\top \in \mathbb{C}^N$ where $f_m = f(\omega_m)$. We stress that \mathbf{f} is empirically accessible so long as the values f_m of f on the states ω_m are known, without requiring knowledge of ω_m . This is the case, for instance, for the values $z_m^{(i)} = Z^{(i)}(\omega_m)$ of the fluxes used as our training data.

In QMCI, we map every such classical observable f to a projected multiplication operator $A_{L,N} := \pi_{L,N} \hat{f}_N \in B(H_{L,N})$. Computationally, this operator is represented by the $L \times L$ matrix representation $\mathbf{A} := \beta_{L,N} A_{L,N} = [A_{ij}]_{i,j=0}^{L-1}$ with elements $A_{ij} = \langle \phi_{i,N}, A_{L,N} \phi_{j,N} \rangle_N$. Using \odot to denote elementwise multiplication of column vectors, we have

$$A_{ij} = \frac{1}{N} \sum_{m=0}^{N-1} \phi_{i,N}(\omega_m) f(\omega_m) \phi_{j,N}(\omega_m) = \frac{1}{N} \phi_i^\top (\mathbf{f} \odot \phi_j).$$

In matrix notation, the above expression becomes

$$(A.2) \quad \mathbf{A} = \frac{1}{N} \mathbf{\Phi}^\top (\text{diag } \mathbf{f}) \mathbf{\Phi}.$$

Note that \mathbf{A} is a self-adjoint matrix whenever f is real-valued. Henceforth, we will assume that this the case.

Given a quantum state $\rho \in Q(H_{L,N})$ with matrix representation

$$(A.3) \quad \boldsymbol{\rho} = [\langle \phi_{i,N}, \rho \phi_{j,N} \rangle_N]_{i,j=0}^{L-1},$$

the quantum mechanical expectation $\mathbb{E}_\rho A$ from (3.1) can be computed as

$$(A.4) \quad \mathbb{E}_\rho A = \text{tr}(\boldsymbol{\rho} \mathbf{A}).$$

If $\boldsymbol{\rho} = \boldsymbol{\xi} \boldsymbol{\xi}^\dagger$ is a pure state associated with a unit vector $\boldsymbol{\xi} \in \mathbb{C}^L$ (recall that † denotes the complex-conjugate transpose), then (A.4) simplifies to

$$\mathbb{E}_\rho A = \boldsymbol{\xi}^\dagger \mathbf{A} \boldsymbol{\xi}.$$

A.1.3. Spectral decomposition. In the stochastic variant of QMCI (see [subsection 5.5](#)), we use the spectral measure $E_{A_{L,N}}$ of $A_{L,N} = \pi_{L,N} \hat{f}_N$ in order to compute the discrete probability distributions $\mathbb{P}_{\rho, A_{L,N}}$ in (4.7) for a given quantum state $\rho \in Q(H_{L,N})$. We stochastically generate flux terms by sampling from these distributions, as follows.

Let $\mathbf{u}_0, \dots, \mathbf{u}_{L-1} \in \mathbb{R}^L$ be a set of orthonormal eigenvectors of \mathbf{A} from (A.2) with corresponding eigenvalues $a_0, \dots, a_{L-1} \in \mathbb{R}$ (potentially with multiplicities). In the $\{\phi_{l,N}\}$ basis of $H_{L,N}$, the spectral measure $E_{A_{L,N}}$ from (4.6) is represented by a matrix-valued measure $\mathbf{E} : \mathcal{B}(\mathbb{R}) \rightarrow \mathbb{M}_L$ with $\mathbf{E}(S) = [\langle \phi_{i,N}, E_{A_{L,N}}(S) \phi_{j,N} \rangle_N]_{i,j=0}^{L-1}$, such that

$$\mathbf{E}(S) = \sum_{l: a_l \in S} \mathbf{u}_l \mathbf{u}_l^\top.$$

Note that for any eigenvalue a_j , the sum $\mathbf{E}^{(j)} = \sum_{l: a_l = a_j} \mathbf{u}_l \mathbf{u}_l^\top$ is the matrix representation of the projection $E_{A_{L,N}}^{(j)}$ onto the eigenspace of $A_{L,N}$ corresponding to a_j .

Given a quantum state $\rho \in Q(H_{L,N})$ with matrix representation $\boldsymbol{\rho}$ from (A.3), the probability distribution $\mathbb{P}_{\rho, A_{L,N}}$ can be evaluated as

$$(A.5) \quad \mathbb{P}_{\rho, A_{L,N}}(S) = \sum_{l: a_l \in S} \text{tr}(\boldsymbol{\rho}(\mathbf{u}_l \mathbf{u}_l^\top)) = \sum_{l: a_l \in S} \mathbf{u}_l^\top \boldsymbol{\rho} \mathbf{u}_l.$$

If $\boldsymbol{\rho} = \boldsymbol{\xi} \boldsymbol{\xi}^\dagger$ is pure, then (A.5) simplifies to

$$\mathbb{P}_{\rho, A_{L,N}}(S) = \sum_{l: a_l \in S} |\boldsymbol{\xi}^\dagger \mathbf{u}_l|^2.$$

Practically, we draw samples from $\mathbb{P}_{\rho, A_{L,N}}$ by computing the probability vector $\mathbf{p} \in \mathbb{R}^L$ with

$$(A.6) \quad \mathbf{p} = (p_0, \dots, p_{L-1}), \quad p_l = P_{\rho, A_{L,N}}(\{a_l\}),$$

and drawing samples from the spectrum $\{a_0, \dots, a_{L-1}\}$ with distribution \mathbf{p} using a sampling algorithm (e.g., `randsample` in MATLAB).

A.1.4. Evolution operators. Following [7, 32, 29], we approximate the Koopman operator by the left shift operator $\hat{U}_N : \hat{H}_N \rightarrow \hat{H}_N$ defined as

$$(A.7) \quad \hat{U}_N f(\omega_m) = \begin{cases} f(\omega_{m+1}), & 0 \leq m \leq N-2, \\ 0, & m = N-1. \end{cases}$$

For completeness, we note that an alternative approach with equivalent asymptotic behavior as $N \rightarrow \infty$ (which we do not use in experiments of sections 7 and 8) is to employ the unitary shift

$$\hat{U}_N f(\omega_m) = \begin{cases} f(\omega_{m+1}), & 0 \leq m \leq N-2, \\ f(\omega_0), & m = N-1. \end{cases}$$

With either approach, we obtain the evolution operator $U_{L,N} : H_{L,N} \rightarrow H_{L,N}$ by projection onto $H_{L,N}$, $U_{L,N} = \Pi_{L,N} \hat{U}_N \Pi_{L,N}$. In the $\{\phi_{l,N}\}$ basis of $H_{L,N}$, $U_{L,N}$ is represented by the $L \times L$ matrix

$$\mathbf{U} = [U_{ij}] = [\langle \phi_{i,N}, \hat{U}_N \phi_j \rangle_N]_{i,j=0}^{L-1}.$$

In particular, for the left shift operator in (A.7), we have

$$U_{ij} = \frac{1}{N} \sum_{m=0}^{N-2} \phi_i(\omega_m) \phi_j(\omega_{m+1}) = \frac{1}{N} \phi_i^\top \hat{\mathbf{U}} \phi_j,$$

where $\hat{\mathbf{U}}$ is the $N \times N$ left shift matrix

$$\hat{\mathbf{U}} = \begin{pmatrix} 0 & 1 & & \\ & \ddots & \ddots & \\ & & 0 & 1 \\ & & & 0 \end{pmatrix}.$$

Equivalently, in matrix notation we have

$$(A.8) \quad \mathbf{U} = \frac{1}{N} \mathbf{\Phi}^\top \hat{\mathbf{U}} \mathbf{\Phi}.$$

Analogously to the data-independent case described in subsection 4.3.3, $U_{L,N}$ has an induced action $\mathcal{P}_{L,N} : B_1(H_{L,N}) \rightarrow B_1(H_{L,N})$ defined by the conjugation formula $\mathcal{P}_{L,N} A = U_{L,N}^* A U_{L,N}$. (Note that, as a vector space, $B_1(H_{L,N})$ is isomorphic to $B(H_{L,N})$ by finite dimensionality of $H_{L,N}$, but $B_1(H_{L,N})$ is equipped with the trace norm, whereas $B(H_{L,N})$ is equipped with the operator norm.) In the $\{\phi_{l,N}\}$ basis of $H_{L,N}$, $\mathcal{P}_{L,N}$ is represented by the linear operator $\mathbf{P} : \mathbb{M}_L \rightarrow \mathbb{M}_L$ on $L \times L$ matrices defined as $\mathbf{P} \mathbf{A} = \mathbf{U}^\top \mathbf{A} \mathbf{U}$. That is, if $\mathbf{A} = \beta_{L,N} A \in \mathbb{M}_L$ is the matrix representation of an operator $A \in B_1(H_{L,N})$, then $\mathbf{P} \mathbf{A}$ is the matrix representation of $\mathcal{P}_{L,N} A$, i.e., $\mathbf{P} \mathbf{A} = \beta_{L,N}(\mathcal{P}_{L,N} A)$.

In general, $U_{L,N}$ is not a unitary operator, so $\mathcal{P}_{L,N}$ does not necessarily map quantum states in $Q(H_{L,N}) \subset B_1(H_{L,N})$ to quantum states (see subsection 4.3.3). However, $\mathcal{P}_{L,N}$ is trace non-increasing, so it generates an open quantum system. In our computations, we enforce state preservation by replacing $\mathcal{P}_{L,N}$ by the nonlinear map

$$\tilde{\mathcal{P}}_{L,N}(\rho) := \frac{\mathcal{P}_{L,N} \rho}{\text{tr}(\mathcal{P}_{L,N} \rho)},$$

defined on the set of quantum states $\rho \in Q(H_{L,N})$ for which $\text{tr}(\mathcal{P}_{L,N}\rho)$ is nonzero. This map is represented by the map \tilde{P} on $L \times L$ density matrices defined as

$$\tilde{P}(\rho) = \frac{P\rho}{\text{tr}(P\rho)}.$$

If $\rho = \xi\xi^\dagger$ is pure, then $\tilde{P}(\rho) = \tilde{\xi}\tilde{\xi}^\dagger$ is a pure state associated with the unit vector

$$\tilde{\xi} = \tilde{P}(\xi) := \frac{U^\top \xi}{\|U^\top \xi\|_2}.$$

Thus, to compute the evolution of pure states it is sufficient to work with the map \tilde{P} on state vectors rather than explicitly with \tilde{P} on density matrices—this results in a reduction of computational cost from $O(L^3)$ to $O(L^2)$; see [subsection 6.6](#).

A.1.5. Effect-valued feature maps. Recall from [subsections 5.3](#) and [6.4](#) that the effect-valued feature map $\mathcal{F}_{L,N} : \mathcal{X} \rightarrow \mathcal{E}(H_{L,N})$ maps each state $x \in \mathcal{X}$ of the resolved variables to a projected multiplication operator $\pi_{L,N}(\hat{F}_N(x))$, where $\hat{F}_N(x) = k(x, X(\cdot)) \in L^\infty(\mu_N)$ is the feature vector associated with the kernel $k : \mathcal{X} \times \mathcal{X} \rightarrow [0, 1]$. In the $\{\phi_{l,N}\}$ basis of $H_{L,N}$, $\mathcal{F}_{L,N}$ is represented by the matrix-valued map $\mathbf{F} : \mathcal{X} \rightarrow \mathbb{M}_L$ with $\mathbf{F} = \beta_{L,N} \circ \mathcal{F}_{L,N}$. That is, we have $\mathbf{F}(x) = \mathbf{A}$, where \mathbf{A} is given by [\(A.2\)](#) with $\mathbf{f} = (k(x, x_0), \dots, k(x, x_{N-1}))^\top$. State conditioning by the effect $\mathcal{F}_{L,N}(x)$ (see [\(3.7\)](#) and [\(5.4\)](#)) can then be computed via the matrix formula

$$(A.9) \quad \rho|_{\mathbf{F}(x)} = \frac{\sqrt{\mathbf{A}}\rho\sqrt{\mathbf{A}}}{\text{tr}(\sqrt{\mathbf{A}}\rho\sqrt{\mathbf{A}})},$$

where $\rho|_{\mathbf{F}(x)}$ is the matrix representation of $\rho|_{\mathcal{F}_{L,N}(x)}$. If $\rho = \xi\xi^\dagger$ is pure, then the conditioned state $\rho|_{\mathbf{F}(x)}$ is also pure, and the associated state vector is given by

$$(A.10) \quad \xi|_{\mathbf{F}(x)} = \frac{\sqrt{\mathbf{A}}\xi}{\|\sqrt{\mathbf{A}}\xi\|_2}.$$

A drawback of [\(A.9\)](#) and [\(A.10\)](#) is that they require the computation of the matrix square root $\sqrt{\mathbf{A}}$. To avoid the cost of this step, we can modify $\mathcal{F}_{L,N}$ to the effect-valued map $\tilde{\mathcal{F}}_{L,N}(x) = (\pi_{L,N}\hat{F}_N^{1/2}(x))^2$. This map is represented by the matrix-valued function $\tilde{\mathbf{F}} : \mathcal{X} \rightarrow \mathbb{M}_L$ such that $\tilde{\mathbf{F}}(x) = \mathbf{A}^2$, where \mathbf{A} is given by [\(A.2\)](#), now with $\mathbf{f} = (\sqrt{k(x, x_0)}, \dots, \sqrt{k(x, x_{N-1})})^\top$. In this case, the conditioning formula by $\tilde{\mathbf{F}}(x)$ becomes

$$(A.11) \quad \rho|_{\tilde{\mathbf{F}}(x)} = \frac{\mathbf{A}\rho\mathbf{A}}{\text{tr}(\mathbf{A}\rho\mathbf{A})},$$

which avoids the matrix square root. Analogously to [\(A.10\)](#), the state vector update under [\(A.11\)](#) when $\rho = \xi\xi^\dagger$ is pure becomes

$$(A.12) \quad \xi|_{\tilde{\mathbf{F}}(x)} = \frac{\mathbf{A}\xi}{\|\mathbf{A}\xi\|_2},$$

which again does not require computation of a matrix square root. Our experiments in [sections 7](#) and [8](#) utilize [\(A.12\)](#) for state conditioning.

Even though, in general, $\mathcal{F}_{L,N}(x)$ and $\tilde{\mathcal{F}}_{L,N}(x)$ are not equal, the two maps have the same asymptotic limit as $N \rightarrow \infty$ and $L \rightarrow \infty$ (see [subsections 4.3.4](#) and [6.5](#)). In that limit, conditioning by any of $\mathcal{F}_{L,N}(x)$ and $\tilde{\mathcal{F}}_{L,N}(x)$ recovers conditioning by $\mathcal{F}(x)$ in the infinite-dimensional quantum system on H . The latter, is in turn consistent with classical Bayesian conditioning by the feature vectors $F(x)$ (see [subsection 4.2.4](#)). We note that for the radial basis function kernel in (5.5) used in our experiments the square root kernel function \sqrt{k} can be obtained simply by scaling the bandwidth parameter ϵ by a factor of $\sqrt{2}$.

A.2. Classical evolution. In the experiments of [sections 7](#) and [8](#), the classical evolution map $\tilde{\phi} : \mathcal{X} \times \mathcal{Z} \rightarrow \mathcal{X}$ is based on a standard RK4 discretization of the resolved component of the dynamics on $\mathcal{X} = \mathbb{R}^{d_{\mathcal{X}}}$, keeping the flux terms in $\mathcal{Z} = \mathbb{R}^d$ fixed. Specifically, given that the resolved components of the dynamics satisfy $\dot{x}(t) = v(x(t), z(t))$ for a vector field $v : \mathcal{X} \times \mathcal{Z} \rightarrow \mathcal{X}$, and the timestep of the parameterized system is Δt , we set

$$(A.13) \quad \begin{aligned} \tilde{\phi}(x, z) &= x + \frac{1}{6}(k_1 + 2k_2 + 2k_3 + k_4) \Delta t, \\ k_1 &= v(x, z), \quad k_2 = v(x + \Delta t k_1/2, z), \\ k_3 &= v(x + \Delta t k_2/2, z), \quad k_4 = v(x + \Delta t k_3, z). \end{aligned}$$

A.3. Algorithm structure. The data-driven QMCI pipeline consists of training, initialization, and simulation/prediction phases, summarized in [Appendices A.3.1](#) to [A.3.3](#) respectively.

A.3.1. Training. Recall that our training dataset consists of time-ordered samples $w_0, \dots, w_{N-1} \in \mathcal{W}$ for computing basis functions, and samples $z_0^{(i)}, \dots, z_{N-1}^{(i)} \in \mathbb{R}$ with $i \in \{1, \dots, d\}$ of the components of the flux $Z : \mathcal{Y} \rightarrow \mathcal{Z}$. In this paper, we assume that the samples are taken on a single dynamical trajectory $\omega_0, \dots, \omega_{N-1} \in \Omega$, i.e., $w_m = W(\omega_m)$, $z_m^{(i)} = Z^{(i)}(\omega_m)$, and $\omega_m = \Phi^m(\omega_0)$ for some initial condition $\omega_0 \in \Omega$. The methods described below can be readily generalized to training with samples from ensembles of shorter trajectories, so long as the sampling measure μ_N of the data converges to the invariant measure in the sense of (6.1). The steps of the training phase are as follows:

1. Tune the bandwidth parameter $\epsilon_{\mathcal{W}}$ of the kernel $\kappa_{\mathcal{W}}$. We perform this step using the automatic tuning procedure developed in refs. [20, 9]. The procedure is based on a grid search in a collection of candidate $\epsilon_{\mathcal{W}}$ values, selecting the value that maximizes a kernel-dependent measure of dimension of the dataset. For pseudocode, see, e.g., Algorithm B.5 in [29].
2. With the bandwidth parameter from Step 1, form the kernel matrix \mathbf{K} and compute the kernel eigenvectors $\{\phi_0, \dots, \phi_{L-1}\}$ from (A.1). Arrange the basis vectors in a matrix Φ as described in [Appendix A.1.1](#). In applications, we typically approximate \mathbf{K} by a sparse matrix using nearest-neighbor truncation, and solve the resulting eigenvalue problem with iterative solvers (e.g., MATLAB's `eigs`).
3. For each $i \in \{1, \dots, d\}$, use Φ and the $z_m^{(i)}$ samples to compute an $L \times L$ multiplication operator matrix $\mathbf{Z}^{(i)}$ via (A.2) with $\mathbf{f} = (z_0^{(i)}, \dots, z_{N-1}^{(i)})^\top$. In the stochastic variant of QMCI, we also compute the eigenvalues $a_0^{(i)}, \dots, a_{L-1}^{(i)} \in \mathbb{R}$ and corresponding eigenvectors $\mathbf{u}_0^{(i)}, \dots, \mathbf{u}_{L-1}^{(i)}$ for each $\mathbf{Z}^{(i)}$.
4. Compute the $L \times L$ Koopman operator matrix \mathbf{U} from (A.8).

A.3.2. Initialization. Let $\hat{x}_0 \in \mathcal{X}$ be a given initial classical state and $\hat{\rho}_0 \in Q(H_{L,N})$ an initial quantum state that may depend on \hat{x}_0 . In the experiments of sections 7 and 8, we set $\hat{\rho}_0$ to the uninformative state $\bar{\rho}_{L,N}$ from (5.7). This is a pure state induced by the unit vector $\bar{\xi}_{L,N} = \bar{\psi}_{L,N} / \|\bar{\psi}_{L,N}\|_{\hat{H}_N}$, where $\bar{\psi}_{L,N} = \sum_{l=0}^{L-1} c_l \phi_{l,N}$ and $c_l = \langle 1_\Omega, \phi_{l,N} \rangle_N$. In column vector notation, the expansion coefficients c_l are given by $c_l = \phi_l^\top \mathbf{1}_N / N$, where $\mathbf{1}_N = (1, \dots, 1)^\top$ is the column vector in \mathbb{C}^N whose all elements are equal to 1. Correspondingly, in the $\{\phi_{l,N}\}$ basis of $H_{L,N}$ the state vector $\bar{\xi}_{L,N}$ is represented by the column vector $\bar{\xi} = \beta_{L,N} \bar{\xi}_{L,N}$ given by

$$\bar{\xi} = \frac{\mathbf{c}}{\|\mathbf{c}\|_2}, \quad \mathbf{c} = (c_0, \dots, c_{L-1})^\top,$$

and the density operator $\bar{\rho}_{L,N}$ is represented by the rank-1 density matrix $\bar{\rho}_{L,N} = \bar{\xi} \bar{\xi}^\top$. Note that if the kernel $\kappa_{\mathcal{W}}$ used to build the basis is normalized to a Markov kernel (see, e.g., the QMCI experiments in subsection 7.3 and the QMDA experiments in refs. [32, 29]), then the leading basis element ϕ_0 can be chosen as $\mathbf{1}_N$, and $\bar{\xi}$ simplifies to the vector $(1, 0, \dots, 0)$.

Besides the choice $\hat{\rho}_0 = \bar{\rho}_{L,N}$, an alternative approach to quantum state initialization (which we do not employ in the experiments presented in this paper) is to use the feature map $\mathcal{F}_{L,N}$ to set $\hat{\rho}_0 = \mathcal{F}_{L,N}(\hat{x}_0) / \text{tr}(\mathcal{F}_{L,N}(\hat{x}_0))$. As noted in subsection 5.4, $\hat{\rho}_0$ obtained with this approach is not, in general, a pure state.

A.3.3. Simulation/prediction. Given the initial data $(\hat{x}_0, \hat{\rho}_0)$ obtained by any of the two methods described in Appendix A.3.2, the QMCI parameterized system evolves by alternating between classical and quantum evolution, as described in subsections 5.2 and 6.4. Algorithm A.1 implements this evolution over r timesteps given that the state of the system at the n -th timestep is $(\hat{x}_n, \hat{\rho}_n)$. We recall that $r \in \mathbb{N}$ is the number of timesteps between each update of the quantum state by the feature map (see subsection 5.2). Thus, the output of Algorithm A.1 is a sequence of classical states $\hat{x}_{n+1}, \dots, \hat{x}_{n+r} \in \mathcal{X}$ at timesteps $n+1, \dots, n+r$, respectively, and a posterior quantum state $\hat{\rho}_{n+r}$ at timestep $n+r$. To continue to march the system forward, Algorithm A.1 is executed with initial conditions $(\hat{x}_{n+r}, \hat{\rho}_{n+r})$.

If the initial state $\hat{\rho}_0 = \hat{\xi}_0 \hat{\xi}_0^\top$ is pure, then under iteration of Algorithm A.1 all subsequent states $\hat{\rho}_r, \hat{\rho}_{2r}, \dots$ are pure. Algorithm A.2 specializes Algorithm A.1 to that setting, which results in a reduction of computational cost from $O(L^3)$ to $O(L^2)$ (see subsection 6.6).

Finally, Algorithm A.3 implements the stochastic variant of QMCI for general (mixed) states. The specialization of this algorithm to pure states is entirely analogous to Algorithm A.2 so we do not include it here in the interest of brevity.

A.4. Histograms and autocorrelation functions. For time-ordered data $f_0, \dots, f_{N-1} \in \mathbb{R}$ sampled at a fixed interval Δt , the value of the time-autocorrelation function $C_{f,N}(\tau_j)$ at timeshift value $\tau_j = j \Delta t$, $j \in \mathbb{N}$, is given by

$$C_{f,N}(\tau_j) = \frac{1}{N} \sum_{n=0}^{N-j} f_n f_{n+j}.$$

In the main text, we show plots of the normalized autocorrelation function $\bar{C}_{f,N}(\tau_j) := C_{f,N}(\tau_j) / C_{f,N}(0)$, where $\bar{C}_{f,N}(0) = 1$ by construction. If the f_n are samples of an observable $f \in L^2(\mu)$ taken on an orbit $\omega_0, \dots, \omega_{N-1}$ of the dynamics, i.e., $f_n = f(\omega_n)$ and $\omega_n = \Phi^n(\omega_0)$, then by the pointwise ergodic theorem, as $N \rightarrow \infty$, $C_{f,N}(\tau_j)$

Algorithm A.1 QMCI forecast–analysis cycle. The algorithm assumes that training has been performed as described in [Appendix A.3.1](#).

Inputs

- Resolved variables $\hat{x}_n \in \mathcal{X}$ and density matrix $\hat{\rho}_n \in \mathbb{M}_L$ at the n -th timestep.
- Number of timesteps $r \in \mathbb{N}$ per quantum Bayesian update.

Outputs

- Resolved variables $\hat{x}_{n+1}, \dots, \hat{x}_{n+r} \in \mathcal{X}$ at timesteps $n+1, \dots, n+r$.
- Posterior density matrix $\hat{\rho}_{n+r} \in \mathbb{M}_L$ at timestep $n+r$.

Steps

1. Set $\tilde{\rho}_n = \hat{\rho}_n$.
 2. For $j \in \{1, \dots, r\}$:
 - (a) Compute the fluxes $z_{n+j-1} = (z_{n+j-1}^{(1)}, \dots, z_{n+j-1}^{(d)}) \in \mathbb{R}^d$ with $z_{n+j-1} = \text{tr}(\tilde{\rho}_{n+j-1} \mathbf{Z}^{(i)})$.
 - (b) Update the resolved variables: $\hat{x}_{n+j} = \tilde{\phi}(\hat{x}_{n+j-1}, z_{n+j-1})$.
 - (c) Update the density matrix with the transfer operator: $\tilde{\rho}_{n+j} = \tilde{P}(\tilde{\rho}_{n+j-1})$.
 3. Evaluate the effect-valued feature map: $\mathbf{e}_{n+r} = \tilde{F}(\hat{x}_{n+r})$.
 4. Compute the posterior density matrix $\hat{\rho}_{n+r} = \tilde{\rho}_{n+r} |_{\mathbf{e}_{n+r}}$ via (A.11).
 5. **Return:** $\hat{x}_{n+1}, \dots, \hat{x}_{n+r}, \hat{\rho}_{n+r}$.
-

Algorithm A.2 QMCI forecast–analysis cycle for pure states. The algorithm assumes that training has been performed as described in [Appendix A.3.1](#).

Inputs

- Resolved variables $\hat{x}_n \in \mathcal{X}$ and state vector $\hat{\xi}_n \in \mathbb{C}^L$ at the n -th timestep.
- Number of timesteps $r \in \mathbb{N}$ per quantum Bayesian update.

Outputs

- Resolved variables $\hat{x}_{n+1}, \dots, \hat{x}_{n+r} \in \mathcal{X}$ at timesteps $n+1, \dots, n+r$.
- Posterior state vectors $\hat{\xi}_{n+r} \in \mathbb{M}_L$ at timestep $n+r$.

Steps

1. Set $\tilde{\xi}_n = \hat{\xi}_n$.
 2. For $j \in \{1, \dots, r\}$:
 - (a) Compute the fluxes $z_{n+j-1} = (z_{n+j-1}^{(1)}, \dots, z_{n+j-1}^{(d)}) \in \mathbb{R}^d$ with $z_{n+j-1} = \tilde{\xi}_{n+j-1}^\dagger \mathbf{Z}^{(i)} \tilde{\xi}_{n+j-1}$.
 - (b) Update the resolved variables: $\hat{x}_{n+j} = \tilde{\phi}(\hat{x}_{n+j-1}, z_{n+j-1})$.
 - (c) Update the state vector with transfer operator: $\tilde{\xi}_{n+j} = \tilde{P}(\tilde{\xi}_{n+j-1})$.
 3. Evaluate the effect-valued feature map: $\mathbf{e} = \tilde{F}(\hat{x}_{n+r})$.
 4. Compute the state vector $\hat{\xi}_{n+r} = \tilde{\xi}_{n+r} |_{\mathbf{e}_{n+r}}$ via (A.12).
 5. **Return:** $\hat{x}_{n+1}, \dots, \hat{x}_{n+r}, \hat{\xi}_{n+r}$.
-

converges for μ -a.e. $\omega_0 \in \Omega$ to $C_f(\tau_j) = \langle f, U^j f \rangle$, where $U : H \rightarrow H$ is the Koopman operator induced by Φ .

To generate histograms based on the data f_0, \dots, f_{N-1} , we split the interval $[\min\{f_n\}_{n=0}^{N-1}, \max\{f_n\}_{n=0}^{N-1}]$ into B uniformly-sized bins S_0, \dots, S_{B-1} , and compute the normalized counts $(N_0/N, \dots, N_{B-1}/N)$ where N_i is the number of datapoints f_n lying in S_i . For our graphs, the value $B = 45$ was chosen.

Algorithm A.3 Stochastic QMCI forecast–analysis cycle. The algorithm assumes that training has been performed as described in [Appendix A.3.1](#).

Inputs

- Resolved variables $\hat{x}_n \in \mathcal{X}$ and density matrix $\hat{\rho}_n \in \mathbb{M}_L$ at the n -th timestep.
- Number of timesteps $r \in \mathbb{N}$ per quantum Bayesian update.

Outputs

- Resolved variables $\hat{x}_{n+1}, \dots, \hat{x}_{n+r} \in \mathcal{X}$ at timesteps $n+1, \dots, n+r$.
- Posterior density matrix $\hat{\rho}_{n+r} \in \mathbb{M}_L$ at timestep $n+r$.

Steps

1. Set $\tilde{\rho}_n = \hat{\rho}_n$.
 2. For $j \in \{1, \dots, r\}$:
 - (a) For $i \in \{1, \dots, d\}$:
 - i. Compute the probability vector $\mathbf{p}_{n+j-1}^{(i)} \in \mathbb{R}^L$ associated with $\tilde{\rho}_{n+j-1}$ and $\mathbf{Z}^{(i)}$ using (A.6).
 - ii. Draw a sample $z_{n+j-1}^{(i)}$ from the spectrum $\{a_0^{(i)}, \dots, a_{L-1}^{(i)}\}$ of $\mathbf{Z}^{(i)}$ with distribution $\mathbf{p}_{n+j-1}^{(i)}$.
 - (b) Set the flux term $z_{n+j-1} = (z_{n+j-1}^{(1)}, \dots, z_{n+j-1}^{(d)}) \in \mathbb{R}^d$, and update the resolved variables: $\hat{x}_{n+j} = \tilde{\phi}(\hat{x}_{n+j-1}, z_{n+j-1})$.
 - (c) Update the density matrix with the transfer operator: $\tilde{\rho}_{n+j} = \tilde{\mathbf{P}}(\tilde{\rho}_{n+j-1})$.
 3. Evaluate the effect-valued feature map: $\mathbf{e}_{n+r} = \tilde{\mathbf{F}}(\hat{x}_{n+r})$.
 4. Compute the posterior density matrix $\hat{\rho}_{n+r} = \tilde{\rho}_{n+r}|_{\mathbf{e}_{n+r}}$ via (A.11).
 5. **Return:** $\hat{x}_{n+1}, \dots, \hat{x}_{n+r}, \hat{\rho}_{n+r}$.
-

REFERENCES

- [1] A. ARAKAWA AND W. H. SCHUBERT, *Interaction of a cumulus cloud ensemble with the large-scale environment, Part I*, J. Atmos. Sci., 31 (1974), pp. 674–701, [https://doi.org/10.1175/1520-0469\(1974\)031<0674:IOACCE>2.0.CO;2](https://doi.org/10.1175/1520-0469(1974)031<0674:IOACCE>2.0.CO;2).
- [2] H. M. ARNOLD, I. M. MOROZ, AND T. N. PALMER, *Stochastic parametrizations and model uncertainty in the Lorenz ’96 system*, Phil. Trans. R. Soc. A, 371 (2013), 20110479, <https://doi.org/10.1098/rsta.2011.0479>.
- [3] Z. ARTSTEIN, J. LINSHIZ, AND E. TITI, *Young measure approach to computing slowly advancing fast oscillations*, Multiscale Model. Simul., 6 (2007), pp. 1085–1097, <https://doi.org/10.1137/070687219>.
- [4] V. BALADI, *Positive Transfer Operators and Decay of Correlations*, vol. 16 of Advanced Series in Nonlinear Dynamics, World Scientific, Singapore, 2000.
- [5] I. BENGTTSSON AND K. ZYCKOWSKI, *Geometry of Quantum States. An Introduction to Quantum Entanglement*, Cambridge University Press, Cambridge, 2006.
- [6] J. BERNER ET AL., *Stochastic parameterization: Toward a new view of weather and climate models*, Bull. Amer. Math. Soc., 98 (2017), pp. 565–588, <https://doi.org/10.1175/BAMS-D-15-00268.1>.
- [7] T. BERRY, D. GIANNAKIS, AND J. HARLIM, *Nonparametric forecasting of low-dimensional dynamical systems*, Phys. Rev. E., 91 (2015), 032915, <https://doi.org/10.1103/PhysRevE.91.032915>.
- [8] T. BERRY, D. GIANNAKIS, AND J. HARLIM, *Bridging data science and dynamical systems theory*, Notices Amer. Math. Soc., 67 (2020), pp. 1336–1349, <https://doi.org/10.1090/noti2151>.
- [9] T. BERRY AND J. HARLIM, *Variable bandwidth diffusion kernels*, Appl. Comput. Harmon. Anal., 40 (2016), pp. 68–96, <https://doi.org/10.1016/j.acha.2015.01.001>.
- [10] M. BLANK, *Ergodic averaging with and without invariant measures*, Nonlinearity, 30 (2017), pp. 4649–4664, <https://doi.org/10.1088/1361-6544/aa8fe8>.
- [11] T. BOLTON AND L. ZANNA, *Applications of deep learning to ocean data inference and subgrid parameterization*, J. Adv. Model. Earth Sy., 11 (2019), pp. 376–399, <https://doi.org/10.1029/2018MS001501>.

- 1029/2018MS001472.
- [12] N. D. BRENOWITZ AND C. S. BRETHERTON, *Prognostic validation of a neural network unified physics parameterization*, Geophys. Res. Lett., 45 (2018), pp. 6289–6298, <https://doi.org/10.1029/2018GL078510>.
- [13] S. L. BRUNTON, B. W. BRUNTON, J. L. PROCTOR, E. KAISER, AND J. N. KUTZ, *Chaos as an intermittently forced linear system*, Nat. Commun., 8 (2017), 19, <https://doi.org/10.1038/s41467-017-00030-8>.
- [14] D. BUROV, D. GIANNAKIS, K. MANOHAR, AND A. STUART, *Kernel analog forecasting: Multiscale test problems*, Multiscale Model. Simul., 19 (2021), pp. 1011–1040, <https://doi.org/10.1137/20M1338289>.
- [15] F. CHATELIN, *Spectral Approximation of Linear Operators*, Classics in Applied Mathematics, Society for Industrial and Applied Mathematics, Philadelphia, 2011.
- [16] N. CHEN AND Y. LI, *BAMCAFE: A Bayesian machine learning advanced forecast ensemble method for complex turbulent systems with partial observations*, Chaos, 31 (2021), 113114, <https://doi.org/10.1063/5.0062028>.
- [17] Y. CHEN, D. SANZ-ALONSO, AND R. WILLETT, *Autodifferentiable ensemble Kalman filters*, SIAM J. Math. Data Sci., 4 (2022), pp. 801–833, <https://doi.org/10.1137/21M1434477>.
- [18] A. J. CHORIN AND F. LU, *Discrete approach to stochastic parametrization and dimension reduction in nonlinear random projections*, Proc. Natl. Acad. Sci., 112 (2015), pp. 9804–9809, <https://doi.org/10.1073/pnas.1512080112>.
- [19] R. COIFMAN AND M. HIRN, *Bi-stochastic kernels via asymmetric affinity functions*, Appl. Comput. Harmon. Anal., 35 (2013), pp. 177–180, <https://doi.org/10.1016/j.acha.2013.01.001>.
- [20] R. R. COIFMAN, Y. SHKOLNISKY, F. J. SIGWORTH, AND A. SINGER, *Graph Laplacian tomography from unknown random projections*, IEEE Trans. Image Process., 17 (2008), pp. 1891–1899, <https://doi.org/10.1109/tip.2008.2002305>.
- [21] D. CROMMELIN AND E. VANDEN-ELJNDEN, *Subgrid-scale parameterization with conditional Markov chains*, J. Atmos. Sci., 65 (2008), pp. 2661–2675, <https://doi.org/10.1175/2008JAS2566.1>.
- [22] S. DAS AND D. GIANNAKIS, *Delay-coordinate maps and the spectra of Koopman operators*, J. Stat. Phys., 175 (2019), pp. 1107–1145, <https://doi.org/10.1007/s10955-019-02272-w>.
- [23] S. DAS, D. GIANNAKIS, AND J. SLAWINSKA, *Reproducing kernel Hilbert space quantification of unitary evolution groups*, Appl. Comput. Harmon. Anal., 54 (2021), pp. 75–136, <https://doi.org/10.1016/j.acha.2021.02.004>.
- [24] M. DELLNITZ AND G. FROYLAND, *On the isolated spectrum of the Perron–Frobenius operator*, Nonlinearity, 13 (2000), pp. 1171–1188, <https://doi.org/10.1088/0951-7715/13/4/310>.
- [25] W. E, B. ENGQUIST, X. LI, W. REN, AND E. VANDEN-ELJNDEN, *Heterogeneous multiscale methods: A review*, Commun. Comput. Phys., 2 (2007), pp. 367–450.
- [26] T. EISNER, B. FARKAS, M. HAASE, AND R. NAGEL, *Operator Theoretic Aspects of Ergodic Theory*, vol. 272 of Graduate Texts in Mathematics, Springer, Cham, 2015.
- [27] I. FATKULLIN AND E. VANDEN-ELJNDEN, *A computational strategy for multiscale systems with applications to Lorenz 96 model*, J. Comput. Phys., 200 (2004), pp. 605–638, <https://doi.org/10.1016/j.jcp.2004.04.013>.
- [28] B. FOX-KEMPER, S. BACHMAN, B. PEARSON, AND S. RECKINGER, *Principles and advances in subgrid modelling for eddy-rich simulations*, CLIVAR Exchanges, 65 (2014), pp. 42–46.
- [29] D. C. FREEMAN, D. GIANNAKIS, B. MINTZ, AND A. OURMAZD, *Data assimilation in operator algebras*, 2022, <https://arxiv.org/abs/2206.13659>.
- [30] P. R. GENT AND J. C. MCWILLIAMS, *Isopycnal mixing in ocean circulation models*, J. Phys. Oceanogr., 20 (1989), pp. 150–155, [https://doi.org/10.1175/1520-0485\(1990\)020\(0150:IMIOCM\)2.0.CO;2](https://doi.org/10.1175/1520-0485(1990)020(0150:IMIOCM)2.0.CO;2).
- [31] D. GIANNAKIS, *Data-driven spectral decomposition and forecasting of ergodic dynamical systems*, Appl. Comput. Harmon. Anal., 47 (2019), pp. 338–396, <https://doi.org/10.1016/j.acha.2017.09.001>.
- [32] D. GIANNAKIS, *Quantum mechanics and data assimilation*, Phys. Rev. E, 100 (2019), 032207, <https://doi.org/10.1103/PhysRevE.100.032207>.
- [33] D. GIANNAKIS, *Delay-coordinate maps, coherence, and approximate spectra of evolution operators*, Res. Math. Sci., 8 (2021), 8, <https://doi.org/10.1007/s40687-020-00239-y>.
- [34] D. GIANNAKIS, A. HENRIKSEN, J. A. TROPP, AND R. WARD, *Learning to forecast dynamical systems from streaming data*, 2021, <https://arxiv.org/abs/2109.09703>.
- [35] D. GIANNAKIS, A. OURMAZD, J. SCHUMACHER, AND J. SLAWINSKA, *Embedding classical dynamics in a quantum computer*, Phys. Rev. A, 105 (2022), 052404, <https://doi.org/10.1103/PhysRevA.105.052404>.
- [36] D. GIANNAKIS, J. SLAWINSKA, AND Z. ZHAO, *Spatiotemporal feature extraction with data-driven*

- Koopman operators*, in Proceedings of the 1st International Workshop on Feature Extraction: Modern Questions and Challenges at NIPS 2015, D. Storcheus, A. Rostamizadeh, and S. Kumar, eds., vol. 44 of Proceedings of Machine Learning Research, Montreal, Canada, 2015, PMLR, pp. 103–115, <https://proceedings.mlr.press/v44/giannakis15.html>.
- [37] K. T. GOH, J. KANIEWSKI, E. WOLFE, T. VÉRTESI, X. WU, Y. CAI, Y.-C. LIANG, AND V. SCARANI, *Geometry of the set of quantum correlations*, Phys. Rev. A, 97 (2018), 022104, <https://doi.org/10.1103/PhysRevA.97.022104>.
 - [38] G. A. GOTTWALD AND S. REICH, *Supervised learning from noisy observations: Combining machine-learning techniques with data assimilation*, Phys. D, 423 (2021), 132911, <https://doi.org/10.1016/j.physd.2021.132911>.
 - [39] W. W. GRABOWSKI, H. MORRISON, S.-I. SHIMA, G. C. ABADE, P. DZIEKAN, AND H. PAWLOWSKA, *Modeling of cloud microphysics: Can we do better?*, Bull. Amer. Meteor. Soc., 100 (2019), pp. 655–672, <https://doi.org/10.1175/BAMS-D-18-0005.1>.
 - [40] W. W. GRABOWSKI AND P. K. SMOLARKIEWICZ, *CRCP: A Cloud Resolving Convection Parameterization of the tropical atmosphere*, Phys. D, 133 (1999), pp. 171–178, [https://doi.org/10.1016/S0167-2789\(99\)00104-9](https://doi.org/10.1016/S0167-2789(99)00104-9).
 - [41] I. GROOMS AND A. J. MAJDA, *Efficient stochastic superparameterization for geophysical turbulence*, Proc. Natl. Acad. Sci., 110 (2013), pp. 4464–4469, <https://doi.org/10.1073/pnas.1302548110>.
 - [42] S. GUDDER, *Quantum probability*, in Handbook of Quantum Logic and Quantum Structures, K. Engesser, D. M. Gabbary, and D. Lehmann, eds., Elsevier, Amsterdam, 2007, pp. 121–146.
 - [43] T. HOFMANN, B. SCHÖLKOPF, AND A. SMOLA, *Kernel methods in machine learning*, Ann. Statist., 36 (2008), pp. 1171–1220, <https://doi.org/10.1214/009053607000000677>.
 - [44] A. S. HOLEVO, *Statistical Structure of Quantum Theory*, vol. 67 of Lecture Notes in Physics Monographs, Springer, Berlin, 2001.
 - [45] S. W. JIANG AND J. HARLIM, *Modeling of missing dynamical systems: Deriving parametric models using a nonparametric framework*, Res. Math. Sci., 7 (2020), p. 16, <https://doi.org/10.1007/s40687-020-00217-4>.
 - [46] P. W. JONES, A. OSIPOV, AND V. ROKHLIN, *Randomized approximate nearest neighbors algorithm*, Proc. Natl. Acad. Sci., 108 (2011), pp. 15679–15686, <https://doi.org/10.1073/pnas.1107769108>.
 - [47] D. KELLY AND I. MELBOURNE, *Deterministic homogenization for fast-slow systems*, J. Funct. Anal., 272 (2017), pp. 4063–4102, <https://doi.org/10.1016/j.jfa.2017.01.015>.
 - [48] S. KLUS, F. NÜSKE, S. PEITZ, J.-H. NIEMANN, C. CLEMENTI, AND C. SCHÜTTE, *Data-driven approximation of the Koopman generator: Model reduction, system identification, and control*, Phys. D, 406 (2020), 132416, <https://doi.org/10.1016/j.physd.2020.132416>.
 - [49] B. O. KOOPMAN, *Hamiltonian systems and transformation in Hilbert space*, Proc. Natl. Acad. Sci., 17 (1931), pp. 315–318, <https://doi.org/10.1073/pnas.17.5.315>.
 - [50] K. LAW, A. SHUKLA, AND A. M. STUART, *Analysis of the 3DVAR filter for the partially observed Lorenz’63 model*, Discrete Contin. Dyn. Syst., 34 (2013), pp. 1061–10178, <https://doi.org/10.3934/dcds.2014.34.1061>.
 - [51] K. LAW, A. STUART, AND K. ZYGALAKIS, *Data Assimilation: A Mathematical Introduction*, vol. 62 of Texts in Applied Mathematics, Springer, New York, 2015, <https://doi.org/10.1007/978-3-319-20325-6>.
 - [52] M. E. LEVINE AND A. M. STUART, *A framework for machine learning of model error in dynamical systems*, 2022, <https://arxiv.org/abs/2107.06658>.
 - [53] J. W.-B. LIN AND J. D. NEELIN, *Influence of a stochastic moist convective parameterization on tropical climate variability*, Geophys. Res. Lett., 27 (2000), pp. 3691–3694, <https://doi.org/10.1029/2000GL011964>.
 - [54] E. N. LORENZ, *Deterministic nonperiodic flow*, J. Atmos. Sci., 20 (1963), pp. 130–141, [https://doi.org/10.1175/1520-0469\(1963\)020<0130:DNF>2.0.CO;2](https://doi.org/10.1175/1520-0469(1963)020<0130:DNF>2.0.CO;2).
 - [55] E. N. LORENZ, *Predictability of weather and climate*, in Predictability of Weather and Climate, T. Palmer and R. Hagedorn, eds., Cambridge University Press, Cambridge, 1996, ch. 3, pp. 40–58.
 - [56] A. J. MAJDA AND J. HARLIM, *Filtering Complex Turbulent Systems*, Cambridge University Press, Cambridge, 2012.
 - [57] A. J. MAJDA, I. I. TIMOFEEV, AND E. VANDEN EIJNDEN, *Models for stochastic climate prediction*, Proc. Natl. Acad. Sci., 96 (1999), pp. 14687–14691, <https://doi.org/10.1073/pnas.96.26.14687>.
 - [58] I. MELBOURNE AND A. M. STUART, *A note on diffusion limits of chaotic skew-product flows*, Nonlinearity, 24 (2011), pp. 1361–1367, <https://doi.org/10.1088/0951-7715/24/4/018>.

- [59] I. MEZIĆ, *Spectral properties of dynamical systems, model reduction and decompositions*, Non-linear Dyn., 41 (2005), pp. 309–325, <https://doi.org/10.1007/s11071-005-2824-x>.
- [60] O. OWHADI AND G. R. YOO, *Kernel flows: From learning kernels from data into the abyss*, J. Comput. Phys., 389 (2019), pp. 22–47, <https://doi.org/10.1016/j.jcp.2019.03.040>.
- [61] T. N. PALMER, *A nonlinear dynamical perspective on model error: A proposal for non-local stochastic-dynamic parametrization in weather and climate prediction models*, Quart. J. Roy. Meteorol. Soc., 127 (2001), pp. 279–304, <https://doi.org/10.1002/qj.49712757202>.
- [62] G. A. PAVLIOTIS AND A. M. STUART, *Multiscale Methods: Averaging and Homogenization*, vol. 53 of Texts in Applied Mathematics, Springer, New York, 2008, <https://doi.org/10.1007/978-0-387-73829-1>.
- [63] A. RAHIMI AND B. RECHT, *Random features for large-scale kernel machines*, in Advances in Neural Information Processing Systems, J. Platt, D. Koller, Y. Singer, and S. Roweis, eds., vol. 20, Curran Associates, Inc., 2007, pp. 1177–1184, <https://proceedings.neurips.cc/paper/2007/file/013a006f03dbc5392effeb8f18fda755-Paper.pdf>.
- [64] C. W. ROWLEY, I. MEZIĆ, S. BAGHERI, P. SCHLATTER, AND D. S. HENNINGSON, *Spectral analysis of nonlinear flows*, J. Fluid Mech., 641 (2009), pp. 115–127, <https://doi.org/10.1017/s0022112009992059>.
- [65] P. SAGAUT, *Large Eddy Simulation for Incompressible Flows*, Springer-Verlag, Berlin, 2006.
- [66] T. SAUER, J. A. YORKE, AND M. CASDAGLI, *Embedology*, J. Stat. Phys., 65 (1991), pp. 579–616, <https://doi.org/10.1007/bf01053745>.
- [67] R. SCHACK, *Quantum theory from four of Hardy’s axioms*, Found. Phys., 33 (2003), pp. 1461–1468, <https://doi.org/10.1023/A:1026044329659>.
- [68] T. SCHNEIDER, A. M. STUART, AND J.-L. WU, *Learning stochastic closures using ensemble Kalman inversion*, Trans. Math. Appl., 5 (2021), tnab003, <https://doi.org/10.1093/imatrm/tnab003>.
- [69] B. K. SRIPERUMBUDUR, K. FUKUMIZU, AND G. R. LANCKRIET, *Universality, characteristic kernels and RKHS embedding of measures*, J. Mach. Learn. Res., 12 (2011), pp. 2389–2410.
- [70] M. TAKESAKI, *Theory of Operator Algebras I*, vol. 124 of Encyclopaedia of Mathematical Sciences, Springer, Berlin, 2001.
- [71] L. A. TAKHTAJAN, *Quantum Mechanics for Mathematicians*, vol. 95 of Graduate Series in Mathematics, American Mathematical Society, Providence, 2008.
- [72] U. VON LUXBURG, M. BELKIN, AND O. BOUSQUET, *Consistency of spectral clustering*, Ann. Stat., 26 (2008), pp. 555–586, <https://doi.org/10.1214/0090536070000000640>.
- [73] D. S. WILKS, *Effects of stochastic parametrizations in the Lorenz ’96 system*, Quart. J. Roy. Meteor. Soc., 131 (2005), pp. 389–407, <https://doi.org/10.1256/qj.04.03>.
- [74] M. O. WILLIAMS, I. G. KEVREKIDIS, AND C. W. ROWLEY, *A data-driven approximation of the Koopman operator: Extending dynamic mode decomposition*, J. Nonlinear Sci., 25 (2015), pp. 1307–1346, <https://doi.org/10.1007/s00332-015-9258-5>.
- [75] J. YUVAL AND P. A. O’GORMANN, *Stable machine-learning parameterization of subgrid processes for climate modeling at a range of resolutions*, Nat. Commun., 11 (2020), 3295, <https://doi.org/10.1038/s41467-020-17142-3>.